



universität  
wien

## MASTERARBEIT / MASTER'S THESIS

Titel der Masterarbeit / Title of the Master's Thesis

### **The role of chemical etching in the electron irradiation of SWCNTs in a 1D-2D carbon heterostructure**

verfasst von / submitted by

Michael Somma, BSc

angestrebter akademischer Grad / in partial fulfilment of the requirements for the degree of

Master of Science (MSc)

Wien, 2022 / Vienna, Year 2022

Studienkennzahl lt. Studienblatt /  
degree programme code as it appears on  
the student record sheet:

A 066 876

Studienrichtung lt. Studienblatt /  
degree programme as it appears on  
the student record sheet:

Masterstudium Physik

Betreut von / Supervisor:

Univ.-Prof. Dr. Jani Kotakoski

## Abstract

The stacking of 2D materials in so called Van der Waals heterostructures (VdWHs) gained interest, because of possible applications in electronics. The focus today is enlarged to an even broader class of materials where mixed low-dimensional nanomaterials are combined, such in the present case of a 1D-2D carbon structure. A floating catalyst chemical vapor deposition (FC-CVD) method provides individual single-walled carbon nanotubes (SWCNTs) and makes the experimental realisation of such a structure possible. The main experimental technique is aberration-corrected scanning transmission electron microscopy (STEM) operated at 60 keV. Small field of view (FOV) (about 10 nm) irradiation experiments were done. One part of SWCNTs in 1D-2D carbon heterostructure show damage and building up of mobile hydrocarbon contamination under ultra high vacuum (UHV) condition. Ruling out knock-on damage and considering the absence of excitation and ionization damage in the studied structure due to its electronic properties the route of chemical etching is followed. The effect of chemical etching and the impact of the local atmosphere in STEM has not been fully understood yet. To study the type of molecules involved in this process, H<sub>2</sub>, O<sub>2</sub> and H<sub>2</sub>O is willingly leaked in the microscope column at 10<sup>-6</sup> – 10<sup>-8</sup> mbar pressure range and the same irradiation experiments as under UHV condition are done. From the leakage experiments of this thesis one can learn that OH-groups under electron radiation can damage the pristine lattice of carbon nanotubes (CNTs). Chemical etching involving O<sub>2</sub> require defects in order to lead to damage. It could be ruled out that pre-existing defects yielding from the synthesis are a necessary condition for the damage, as CNTs are stable under an O<sub>2</sub> atmosphere. The pristine graphene lattice remains untouched by this damaging mechanism. In the proposed damaging mechanism water molecules enters the ends of the CNTs and diffuse inside. The water can be split into OH-molecule in the FOV by the electron beam. The molecules are thought to bond to the sidewalls inside the CNT and could cause defects by a beam driven chemical etching process. From previous studies [1, 2] it is suggested that these defects can act as nucleation site for the destruction of the CNT by further chemical etching. The leakage experiment strongly indicate that the damage observed at UHV condition is a chemical etching process depending on water contained in the local atmosphere.

# Zusammenfassung

Das Übereinanderschichten von so genannten Van der Waals Heterostrukturen ist interessant wegen möglicher neuartiger Anwendungen in der Elektronik. Das Augenmerk wird heutzutage vermehrt auf die Kombination von unterschiedlich dimensionalen Nanomaterialien gelegt, wie im hier behandelten Fall einer 1D-2D Kohlenstoffstruktur. Eine spezielle chemische Gasphasenabscheidung mit treibenden Katalysatorpartikeln stellt individuelle einwändige Kohlenstoffnanoröhren bereit und ermöglicht die experimentelle Realisierung dieser Struktur. Die experimentelle Haupttechnik ist Aberrations-korrigierte Rastertransmissionselektronenmikroskopie bei 60 keV. Bei kleinen Sichtfeldern (etwa 10 nm) werden Bestrahlungsexperimente durchgeführt. Ein Teil der Kohlenstoffnanoröhren gehen dabei kaputt und mobile Kohlenwasserstoffverunreinigungen werden angehäuft unter ultrahohen Vakuumbedingungen. Da Knock-on Beschädigungen bei 60 keV ausgeschlossen werden können und die Struktur aufgrund ihrer elektronischen Eigenschaften keine Schäden durch Anregung oder Ionisierung erfährt, wird der Fokus auf chemische Ätzprozesse, d. h. die Wechselwirkung von durch den Elektronenstrahl radikalisierten Molekülen mit der Probe, gelegt. Die Rolle dieser Ätzprozesse und der Einfluss der lokalen Umgebung in der Rastertransmissionselektronenmikroskopie sind nicht vollständig geklärt. Um die Art der Moleküle, die an dem Prozess beteiligt sind, genauer zu erforschen, werden  $H_2$ ,  $O_2$  und  $H_2O$  in das Mikroskop bei Drücken von  $10^{-6} - 10^{-8}$  mbar gezielt eingeleitet und die gleichen Bestrahlungsexperimente wie bei ultrahohen Vakuumbedingungen durchgeführt. Aus den Experimenten, bei denen Gase eingeleitet wurden, geht hervor, dass OH-Gruppen unter Elektronenbestrahlung unberührte Kohlenstoffnanoröhren zerstören können. Chemische Ätzprozesse mit  $O_2$  brauchen Defekte, um zu Zerstörung zu führen. Es konnte ausgeschlossen werden, dass präexistente Defekte von der Herstellung eine notwendige Bedingung für die Zerstörung sind, da die Kohlenstoffnanoröhren unter  $O_2$  Umgebung stabil sind. Das unberührte Graphengitter ist nicht von diesem Zerstörungsmechanismus betroffen. Bei dem vorgeschlagenen Zerstörungsmechanismus wandern Wassermoleküle in die Enden der Kohlenstoffnanoröhren und diffundieren innerhalb. Das Wasser könnte im Sichtfeld vom Elektronenstrahl in OH-Moleküle geteilt. Die Moleküle können günstigerweise an den Seitenwänden im Inneren der Kohlenstoffnanoröhren gebunden werden und verursachen möglicherweise Defekte durch einen Elektronenstrahl-gesteuerten chemischen Ätzprozess. Neuliche Studien [1, 2] legen nahe, dass die Defekte als Keim für die Zerstörung durch weitere chemische Ätzprozesse dienen können. Die Experimente, bei denen Gase eingeleitet wurden, indizieren deutlich, dass die Zerstörung bei ultrahohen Vakuumbedingungen von chemischen Ätzprozessen abhängt, die ihren Ursprung in Wassermolekülen in der lokalen

Umgebung finden.

## Acknowledgments

First of all I sincerely want to thank my supervisor for this thesis, Prof. Jani Kotakoski. It isn't by far a course of natural action to meet a professor that is always available giving the right amount of support and encouragement. My case was special, as I had to interrupt my masterproject due to worst form of chronic fatigue syndrome, where I was bedridden for nearly two years and when I couldn't talk at worst times. I'm so glad that Prof. Kotakoski didn't hesitate one second when I came back and gave me the opportunity to resume my project. Secondly, I want to thank Dr. Kimmo Mustonen for his help and guidance in terms of electron microscopy and sample preparation. The second parts of the experiments leading to this thesis weren't possible without his steady support. I want to express my thanks to Dr. Clemens Mangler for the technical support for the Nion UltraSTEM. He was always there when things didn't go as they were supposed to. Fabian Kraft built a laser cleaning set-up. The experiments for this thesis would have been close to impossible without it. In terms of CNT synthesis my thanks go to Dr. Saeed Ahamd and Aqeel Hussain, our collaborators from Aalto University of Prof. Kauppinen's group.

# Contents

<b>1</b>	<b>Introduction</b>	<b>8</b>
<b>2</b>	<b>Theory, Methods and Materials</b>	<b>12</b>
2.1	Graphene and carbon nanotubes . . . . .	12
2.2	Chemical vapor deposition . . . . .	15
2.2.1	Working principle . . . . .	15
2.2.2	Graphene synthesis . . . . .	16
2.2.3	Basic principle of floating catalyst-CVD of SWCNTs . . . . .	18
2.2.4	Thermophoretic Deposition . . . . .	19
2.2.5	Differential mobility analysis . . . . .	20
2.2.6	FC-CVD of SWCNTs . . . . .	22
2.3	Scanning transmission electron microscopy . . . . .	24
2.3.1	Basic principle . . . . .	24
2.3.2	Aberrations, resolution and image quality in STEM . . . . .	26
2.3.3	Nion UltraSTEM 100 . . . . .	28
2.3.4	Diffraction pattern of carbon nanotubes . . . . .	33
2.3.5	Hydrocarbon contamination in (S)TEM . . . . .	34
2.4	CNT-graphene van der Waals heterostructure . . . . .	36

2.5	Irradiation damage in STEM . . . . .	38
2.5.1	Damage in low-dimensional carbon materials . . . . .	38
2.5.2	Electron irradiation of CNTs . . . . .	39
2.5.3	Chemical etching in STEM . . . . .	42
2.6	Chemistry of graphitic carbon networks . . . . .	43
2.6.1	Chemical reactivity of graphene and CNTs . . . . .	43
2.6.2	Hydroxyl groups on graphene . . . . .	46
2.6.3	OH-groups forming point defects in graphene in TEM . . . . .	47
<b>3</b>	<b>Experiment, Results and Discussion</b>	<b>51</b>
3.1	Analysis of STEM images . . . . .	51
3.2	Electron dose analysis of the damage at UHV . . . . .	54
3.3	Damaging of CNTs under UHV . . . . .	55
3.3.1	Sample no.189, 190 and 195 . . . . .	55
3.3.2	Sample no.192 . . . . .	57
3.3.3	Sample no.239 . . . . .	60
3.3.4	Sample no.333 . . . . .	62
3.3.5	Hypothesis for the damaging mechanism at UHV . . . . .	63
3.4	(Ir)radiation of CNTs under hydrogen, oxygen and water atmospheres . . . . .	65
3.4.1	Sample no.374 . . . . .	65
3.4.2	Sample no.334 . . . . .	67
3.4.3	Sample no.1094 and 1095 . . . . .	74
3.5	UHV damage, dependencies and general observations . . . . .	81
<b>4</b>	<b>Conclusion and Outlook</b>	<b>84</b>

## List of Abbreviations

CCD	charge-coupled device
CNT	carbon nanotube
CPC	charged particle counter
CVD	chemical vapor deposition
DFT	density functional theory
DMA	differential mobility analyzer
FC-CVD	floating catalyst chemical vapor deposition
FFT	fast Fourier transform
FOV	field of view
HRTEM	high-resolution transmission electron microscopy
MAADF	mid-angle annular dark field
MWCNT	multi-walled carbon nanotube
OG	objective gauge
PMMA	poly methyl-methacrylate
STEM	scanning transmission microscopy
SWCNT	single-walled carbon nanotube
TEM	transmission electron microscopy
TP	thermophoretic precipitator
UHV	ultra high vacuum
VdWH	van der Waals heterostructure
VOA	virtual objective aperture

# Chapter 1

## Introduction

The following research question will be covered in this thesis: *What part plays the local atmosphere and its composition in the damaging of SWCNTs in a 1D-2D carbon VdWHs under UHV and what is the mechanism of chemical etching under controlled  $H_2$ ,  $O_2$  and  $H_2O$  in this system in aberration-corrected scanning transmission electron microscopy?*

Multi-walled carbon nanotubes (MWCNTs) were first discovered in 1991. The interest focused on SWCNTs, as theoretical calculations predicted that CNTs depending on diameter and chirality could have either metallic or semiconducting behavior. The electronic properties have novel applications in the field of nanoelectronics [3].

Starting from the discovery of graphene in 2004 [4], the theoretically predicted extraordinary thermal, mechanical and electronic properties gave rise to an extensive amount of research. Graphene is one of the most promising materials in nanotechnology [5]. The tailoring of electronic properties nowadays focuses on the introduction of defects [6, 5], and the atomic manipulation of foreign atoms [7]. Both can be done in *in situ* experiments in state-of-the-art scanning transmission electron microscopy (STEM) at atomic precision.

The studied system consists in SWCNTs that are suspended on graphene. Such structures are called VdWHs. The interaction between the SWCNT and the graphene layer is limited to van der Waals (VdW) interaction and no covalent bonds are formed. A recent STEM study [8] shows that the VdW interaction has a significant impact on the structure of both SWCNTs and graphene. The SWCNTs are flattened and the graphene gets curved. The research interest in the field of VdWHs up to now was down to combining 2D-materials [9]. Protodevices have been fabricated, like a bipolar field effective transistor, where hexagonal boron nitride (hBN) and molybdenum

disulfide ( $\text{MoS}_2$ ) was sandwiched by two graphene layers [10]. The research is extended to mixed-dimensional VdWHs [9]. Sticking to low-dimensional materials, in these structures 2D-materials are combined with 1D or 0D materials. In the present study a carbon 1D-2D VdWHs is examined. There is no direct application in the field of electronics of the system, as pristine graphene has no band gap, but yet it is of fundamental interest. The studied system is suitable to study both the surface diffusion on graphene and the in-tube diffusion in SWCNT.

In terms of sample preparation the SWCNT are produced by a highly specialised gas-phase chemical vapor deposition (CVD) method. The advantage of this method is that the SWCNTs are highly individual and are transferred directly on the target TEM-grids. The high individuality enables the experimental realisation of a 1D-2D carbon VdWHs.

The starting point for the study is the electron irradiation damage of SWCNTs on graphene and the building up of mobile hydrocarbon contamination in STEM. The damaging mechanism has no straight forward explanation in terms of established theory. There are three main mechanisms that cause radiation damage in electron microscopy. Firstly, knock-on damage is due to elastic scattering. Secondly, ionization and excitation occur when electrons are removed from an atom or excited to a higher energy level. Lastly, the less studied mechanism is chemical etching processes. Molecules or groups of the residual vacuum are split under the electron beam and react with the sample. In usual TEM systems the vacuum is around  $10^{-7}$  mbar. The leading opinion is that these pressures are not sufficient to cause structural changes to the sample [1]. There is clear indication that chemical etching processes can lead to damage that is not primarily dependent on the electron energy and depend on the local atmosphere of the microscope [11]. Experiments in controlled low-pressure atmospheres give for the first time the chance to find out, what exactly causes this chemical etching processes. Two studies [1, 2], with such leakage experiments are reported on the literature. The studies show that controlled  $\text{O}_2$  and  $\text{H}_2\text{O}$  low-pressure atmospheres lead to chemical etching of the hydrocarbon contamination. That is in alignment with what is observed in electron microscopy with similar pressures of the residual air [1]. Graphene is etched in the presence of reactive lattice imperfections, such as edges or defects. The pristine graphene remains untouched [2].

A recent study [12] adopting aberration-corrected TEM and density functional theory (DFT) simulations suggests that point defects in graphene can be formed by the assistance of OH-groups. The theoretical calculations show that energy barriers in the damaging mechanism are exceeded by the electron energies used in TEM experiments. This applies also for the 60 keV used in the

current study.

The main experimental method applied in this study is aberration-corrected STEM with atomic resolution. The microscope is operated at 60 keV. This technique enables the study of just one SWCNT suspended on graphene at atomic resolution. The fast image processing at low field of views (FOVs) makes it specially suitable for the planned irradiation experiments. The microscope's vacuum is normally at UHV condition ( $10^{-10}$  mbar). This is how the first experiments for this thesis are done. In the second part experiments under controlled atmospheres of  $H_2$ ,  $O_2$  and  $H_2O$  are performed. Those gases are willingly leaked in the microscope column.

The hypothesis that should be put to test in this thesis reads:

*Under controlled water atmospheres at residual pressures of  $10^{-6} - 10^{-8}$  Torr CNTs in a carbon VdWHS damage. They are stable under similar  $O_2$  and  $H_2$  pressures. As the CNTs are stable under  $O_2$  atmosphere, defects are not a condition for the process. The formed point defect acts as nucleation site for further chemical etching involving OH-groups.*

*A part of SWCNTs in a carbon VdWHS under UHV condition show damage and accumulation of mobile hydrocarbon contamination. The damage could be attributed to water in the local atmosphere and the damaging mechanism matches the one proposed for the experiments under controlled water atmosphere. Once a reactive site is formed mobile hydrocarbon contamination, that is diffusing, is bond to the SWCNT and becomes visible in STEM. The contamination that sticks to the SWCNT attracts further mobile contamination until exhaustion.*

The aim of this study is to find out what causes the damage of SWCNTs in the 1D-2D carbon VdWHS at UHV. The impact of the local atmospheres, i.e. the role of split molecules under the electron beam and its reaction with the sample in STEM is not fully understood. This thesis is meant to give further insight in the process of chemical etching under electron irradiation by the means of experiments under controlled atmospheres. Mobile contamination is a big issue especially in samples that are treated by *pre situ* laserling. An attempt will be made to get more control over this effect and find out about crucial parameters involved. Further, an answer to the question whether chemical etching involving OH-groups can form defects to pristine graphitic networks.

The main outcome of the experiments leading to this thesis is that the pristine SWCNT freely suspended and in a 1D-2D VdwHS damage under controlled  $H_2O$  atmospheres under electron irradiation in STEM at 60 keV. The process, unlike chemical etching involving  $O_2$  that has been

already studied with graphene, does not strictly need a pre-existing defect or lattice imperfection.

# Chapter 2

## Theory, Methods and Materials

### 2.1 Graphene and carbon nanotubes

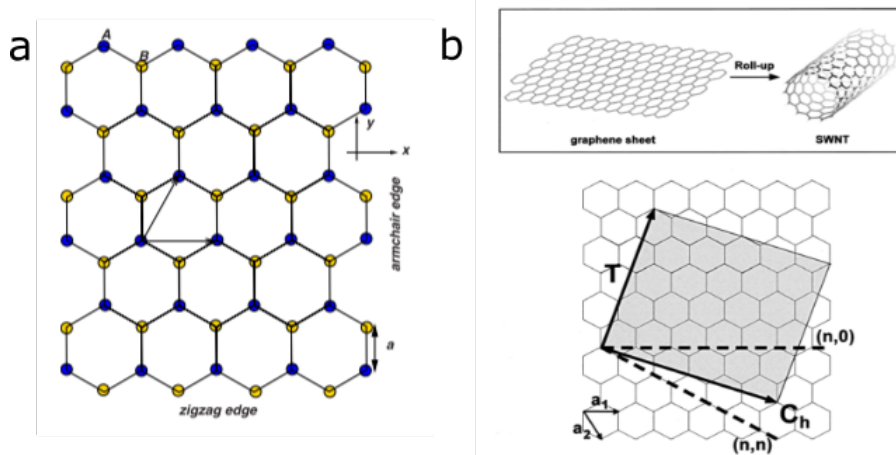


Figure 2.1: **Atomic structure of graphene and CNTs.** (a) atomic structure of graphene (honeycomb lattice) including the two possible edge states, zigzag and armchair, reprinted figure with permission from [13] Copyright (2009) by the American Physical Society. (b) atomic structure of a carbon nanotube.  $C_h$  is the chiral vector,  $(n, m)$  the chiral indices,  $a_1$  and  $a_2$  are the basis vectors,  $T$  is the translation vector, reprinted with permission from [3]. Copyright (2000) American Chemical Society.

Graphene is a single atomic layer of  $sp^2$ -bonded carbon atoms arranged in a honeycomb lattice, as shown in Fig. 2.1(a). It shows remarkable properties, which makes it very interesting system to study, such as: mechanical breaking strength ( $\sim 40$  N/m [14]) and (Young's modulus  $\sim 1.0$  TPa [14]), thermal properties at room temperature (thermal conductivity  $\sim 3000$   $Wm^{-1}K^{-1}$  [14]). But the most expressed scientific interest in graphene came because of its electronic properties.

Those include the conduction of electrons (and holes) in a single layer less than 1 nm thick, with mobility  $\mu = 200000 \text{ cm}^2/\text{Vs}$  [14] at room temperature for freely suspended graphene. These properties apply in a number of fields, including in electronics in the construction of ultra-capacitors, graphene transistors, integrated circuits, etc. [14].

The  $s$ ,  $p_x$  and  $p_y$  electrons of carbon give rise to the  $\sigma$  and  $\sigma^*$ , bonding and antibonding, bands. Those are responsible for the elastical properties. The remaining  $p_z$  electrons form by interaction with neighboring atoms the  $\pi$  and  $\pi^*$  bands. Those are responsible for the electronic properties and are the valence and conduction band respectively [15]. The electron band structure calculated with the tight-binding model is shown in Fig. 2.2. The zoom of the figure show the dispersion near the so called the Dirac points  $K$  and  $K'$ . Those are symmetry points from the corners of the Brillouin zone. The dispersion near the Dirac points is linear and this leads to the electronic properties of graphene [13]. The Fermi-level is located at the Dirac points where the  $\pi$  and  $\pi^*$  bands touch giving metallic character to graphene [15].

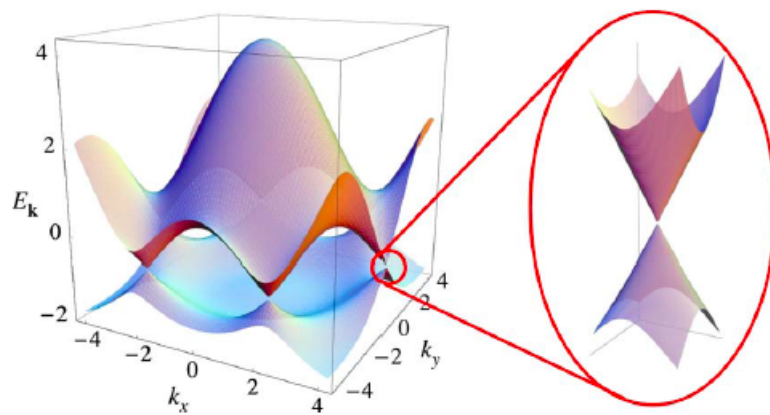


Figure 2.2: **Electronic dispersion of graphene.** the electronic dispersion of monolayer graphene with a zoom near the Dirac points  $K$ . The  $\pi$  and  $\pi^*$  bands. Reprinted figure with permission from [13] Copyright (2009) by the American Physical Society.

Graphene has two atoms per unit cell, thus has six phonon modes. There are three acoustic and three optical ones denoted by A and O respectively. Longitudinal and transversal (L/T) refer to the direction with respect to the axis connecting the two basis atoms [16].

In 1991 MWCNTs were produced and identified by TEM. The structural, chemical, mechanical, thermal and electronic properties, similarly as in the case of graphene, increased the interest in studying CNTs. In 1993 the first systematic synthesis of SWCNTs, as shown in Fig. 2.1(b), was reported, giving birth to a decade and a half of intensive research in this field. The major achieve-

ments in the research of CNT growth include the purity of SWCNTs, the division in metallic and semiconducting CNTs as well as p- and n-type doping. After intensive research, nowadays the focus lies on technical applications [14].

A SWCNT is a one atom thick rolled-up graphene sheet, as shown in Fig. 2.1(b). Each tube is characterized by its chiral vector

$$\mathbf{C}_h = m\mathbf{a}_1 + n\mathbf{a}_2 \quad (2.1)$$

where  $n, m$  are integers showing the components of the vector in terms of the unit-vectors of the honeycomb lattice, as represented in Fig. 2.1(b).

The chiral angle  $\theta$  can be written in terms of the chiral indices  $(n, m)$

$$\theta = \tan^{-1}[\sqrt{3}m/(m + 2n)]. \quad (2.2)$$

A  $\theta$  of  $0^\circ$  is a zigzag species and  $30^\circ$  correspond to armchair. The tube diameter can be expressed in terms of  $(n, m)$ , as well, where  $a$  stands for the lattice constant in graphene,

$$d_t = \frac{a}{\pi} \sqrt{m^2 + mn + n^2}. \quad (2.3)$$

In the electronic structure of a CNT the confinement of the 1D electronic states must be taken into account. The  $\sigma$  bands cause strong covalent in-plane binding, whereas the  $\pi$  bands are responsible for the VdW interaction, similar as in a graphite crystal. The  $\pi$  and  $\pi^*$  (valence/conduction) bands are close to Fermi-level allowing optical excitation. Considering the density of states (DOS) represented in Fig. 2.3(c) the analysis of the energy dispersion simplifies. The optical absorption/emission is related to the electronic states close to the van Hove singularities (vHSs). The vHSs closer to Fermi-level, as can be seen in Fig. 2.3(a)(b) originate from the cutting points near to the Dirac points. The electronic properties depend on where the vHSs cut the electronic dispersion of the parent material graphene, compare Fig. 2.3(a). If there is no allowed  $k$ -vector crossing the  $K$ -point, the tube is semiconducting. This can be related to the chiral indices. If  $\frac{n-m}{3}$  is an integer, the tube is metallic, like in the case of armchair. Otherwise, the CNT is semiconducting [16].

The number of hexagons  $N$  in the unit cell of CNTs is given by

$$N = \frac{2(m^2 + n^2 + mn)}{d_t}. \quad (2.4)$$

There are 2 atoms per hexagon and so for a (10,10) CNT there are  $6N$  phonon branches [17]. There is a fourth acoustic mode added compared to the parent material graphene. The longitudinal and

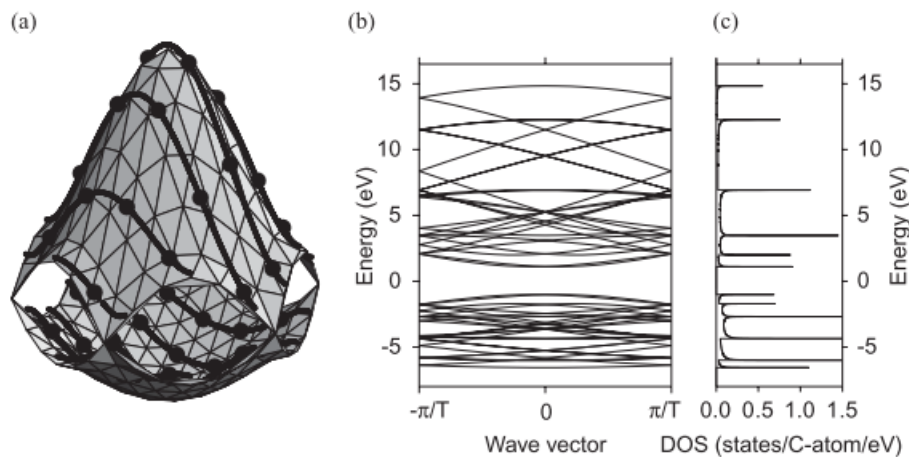


Figure 2.3: **Electronic structure of CNTs.** (a) the energy dispersion in the tight-binding model of the first Brillouin zone and the dark lines show the cutting points of the nanotube (4,2). (b) the electron energy dispersion from a) obtained by zone-folding. (c) the density of states (DOS) of the diagram shown in b). Reprinted from [16], Copyright (2004), with permission from Elsevier. .

transversal in plane modes split into various features depending on the chirality. From the low-lying optical modes, there are expected to be three active modes, but only the radial breathing modes (RBM) is observable experimentally. In this mode the atoms stretch their bonds out-of-plane leading to a coherent expansion and contractions in radial direction [16]. The RBM strongly depends on the diameter and the chirality [18].

## 2.2 Chemical vapor deposition

In this section the synthesis of the used samples will be discussed. An introduction to chemical vapor deposition will be given, then the special methods applied in this experiment, for graphene and CNTs, will be focused on.

### 2.2.1 Working principle

Chemical vapor deposition (CVD) consists of the activation of gaseous reactants and the eventual chemical reaction. Stable solids are formed and deposited on a suitable substrate. The energy needed can be provided in different forms including heat, light or electric discharge. There are two types of reactions, homogeneous gas-phase reactions and heterogeneous chemical reactions happening near a heated surface leading to powders or films. In the production of thin films the

heterogeneous reactions should be favoured and the homogeneous one should be avoided. The processing steps can be divided as follows. Firstly in the *heating step* the quartz tube surrounded by a tubular furnace is heated up to pre-processing temperature. In the *annealing step* the temperature is maintained and the first chemical reactions happen. The metal catalyst surface is cleaned and the crystalline orientation, roughness and the grain size are modified. In the *growing step* new precursors are introduced and the actual growth over the catalyst substrate happens. There are one-step and many-step processes. In the *cooling step* the reactor is cooled usually under the same atmosphere as in the growing step. It is cooled under 200 °C to prevent the oxidation of oxygen-containing groups in spots where there is no coverage of the grown material. Finally the chamber is filled with inert gas, mainly N or Ar, and brought back to atmospheric pressure [19].

### 2.2.2 Graphene synthesis

In the case of graphene, methane is the most mentioned carbon source. To reduce the required temperature transition metal catalysts, mainly Ni and Cu, are used in the reaction. There are two different proposed growth mechanisms in Cu and Ni. The solubility of carbon in Ni is much higher than in Cu. In the case of Cu the process is meant to be limited to the surface and there is negligible dissolution into the catalyst material. Further no precipitation during the cooling can be observed. In Ni carbon atoms can easily dissolve and the graphene growth mainly yields from precipitation during the cool-down step in the process. It leads to polycrystalline graphene. The lower the base pressure, the lower the density of impurities and residual oxygen. Experiments have been performed over a large range of pressures, ranging from high vacuum ( $10^{-4} - 10^{-6}$  Torr) and low pressure (0.1 – 1 Torr) to atmospheric pressure (760 Torr). Graphene of acceptable quality could be synthesized at all pressure ranges, but there are big differences in domain size and morphology. Another important thermodynamic parameter is temperature. The temperature can vary from 800 °C-1100 °C. At higher temperatures the dissociation of carbon precursors are promoted. Also the surface smoothening plays a key role in the synthesis over metal catalysts. In the case of Cu and Ni a temperature range of 900 °C-1050 °C is used. High temperatures lead to large domain size, but more metal is evaporated leading to roughness of the surface [19].

In this study three types of graphene are used.

The first two types are commercial CVD-grown graphene by Graphenea. The graphene shows a transparency of 97% and the film has a coverage of 95%. The graphene's quality is checked by Raman spectroscopy by the manufacturer [20]. In the first case, TEM-gold-grids are available with

graphene and are ready-to-use. The second type is "Easy transfer" graphene. The graphene is transferred to the Si-N grids. The gold-grids are 3 mm in diameter and have an amorphous carbon film ("Quantifoils") with 2  $\mu\text{m}$  holes. The Si-N grids consist of a silicon basis wafer, 3 mm in diameter, with a 0.5 mm  $\times$  0.5 mm window and a 200 nm Si-N film with 2.5  $\mu\text{m}$  diameter holes [21]. The transfer process involves three steps. In the first one, the sample is put into deionized water removing the polymer film. Secondly, the graphene and the sacrificial layer, that is found on top, are put on the TEM-grid. The water is removed by air-drying. In the last step the sacrificial layer is removed by a thermal treatment. The grids are annealed in Ar/H<sub>2</sub> (95/5 molar fractions) at 400 °C for 4 h [20].

The second type is graphene grown with a methane-based CVD with copper substrate [19]. For the synthesis a Danube Nanotech System is used. The experimental set-up consists of a quartz tube that is connected to a pump (Edwards EMF10). On the other side the copper can be loaded on top of a glass stripe and the gas lines are connected that are regulated by Alicat flow controllers. The furnace (Carbolyte) can be driven to the position where the sample sits. For the transfer process a spincoater consisting of turning wheel connected to an electrical power source is used. The turning speed can be regulated by tuning the power. Firstly the copper foil is cut into cm pieces and is inserted into the quartz tube of the CVD furnace. The tube is closed and the pressure is pumped down to the mid  $10^{-2}$  mbar range for 20 min with the provided pump. The gas flow of Ar/H<sub>2</sub> (95/5 molar fractions) is set up at  $(2.1 \pm 0.1)$  slpm. Then the methane flow control is switched on at  $(5 \pm 1)$  sccm and one waits for 5 min. Then the furnace is brought at the position of the quartz tube where the sample is and is turned on. The furnace contains a temperature controller. The target temperature is set to  $(960 \pm 1)$  °C for 2 h. After the growth step the methane line is closed. After 1 h the heating and the methane flow is turned off but the Ar/H<sub>2</sub> line is still kept on. Now the graphene is transferred onto TEM-grids. The copper that contains the graphene is cut into pieces that are of the size of the TEM-grids (3 mm in diameter). The copper is spincoated with poly methyl methacrylate (PMMA) by turning on the spincoater and adding a drop onto the copper foil. The stripes are put into 10% nitric acid and kept there for 4-6 h until the copper is etched away. After the etching, the graphene with the PMMA are floating on the nitric acid. The TEM-grids are held with tweezers and the flakes in the nitric acid are fished. Then the grids are put into water to get rid of the acid. To finally transfer the graphene onto the grids they are put onto a hot plate (150 °C) for 20 min. After the transfer the samples are baked in order to get rid of the PMMA. This is done again in the furnace where the graphene synthesis happened. The samples are loaded to the quartz tube. The pressure is pumped down to mid  $10^{-2}$  mbar with the

provided pump. The tube is vented with Ar at a flow of  $(1.5 \pm 0.1)$  slpm. Then a 400 °C bake for 4 h is done. After that the Ar line is closed and the system is cooled down for 2 h. Before unloading the sample carefully, the provided pump is switched off and the tube is slowly vented with air. The uncertainties are estimated by the resolution of the respective displays.

The samples for the present study were not prepared by myself, this workflow is from a synthesis with the same system and approach for samples for a different purpose. The type of graphene and TEM-grid will be stated for each experiment separately.

### 2.2.3 Basic principle of floating catalyst-CVD of SWCNTs

In the following the attention will be put to special gas-phase CVD for the CNT synthesis. This method relies on the decomposition of a carbon source on nanometer-sized particles that act as catalysts and as a CNT formation sites. Metal-organic compounds, such as ferrocene ( $\text{Fe}(\text{C}_5\text{H}_5)_2$ ), are used. Special interest applies to CO as a carbon source as the disproportionation reaction  $2 \text{CO}(\text{g}) \leftrightarrow \text{C}(\text{s}) + \text{CO}_2(\text{g})$  requires the presence of a catalyst. That way thermal self-decomposition can be avoided [22]. In Fig. 2.4(a) a schematic representation of the used reactor for the CNT synthesis is presented. The core consists of a quartz tube ( $d = 28$  mm;  $t = 2$  mm;  $h = 87$  cm) and an electrical furnace (entech Ängelholm Sweden). There are ducts for the primary and secondary flow of the CO, the ferrocene and the  $\text{CO}_2$ . The flows are controlled by mass flow controls (MFC). In this experiment ferrocene is sublimated in the flow of CO. This gas is inserted through an injector probe that is water cooled to 24 °C forming a steep temperature gradient in which ferrocene is decomposed into iron vapor [24]. At the exhaust part a special collector duct is used for the CNT deposition on cellulose filters [22]. As the catalyst in this CVD method are in aerosol phase, the method is also referred to as floating catalyst CVD (FC-CVD). The biggest advantage over conventional CVD methods is that the CNTs can be directly deposited onto the target substrate and do not have to be transferred [24]. The main steps that are understood in the CNT formation will be described. On the upper part of the reactor ferrocene vapor and CO enter the quartz tube. Ferrocene is partially decomposed and nanometer-sized catalyst particles are formed. Catalytic disproportionation, where CO is transformed into  $\text{CO}_2$ , and hydrocarbon as well as catalytic ferrocene decomposition occurs. After that the carbon is dissolved into the particle. Then the particle is saturated with carbon and on the particle surface a carbon film is formed. The catalyst particle with a graphitic layer is cleaned by  $\text{CO}_2$ . If the catalyst particle is small enough, the CNT growth starts [22].

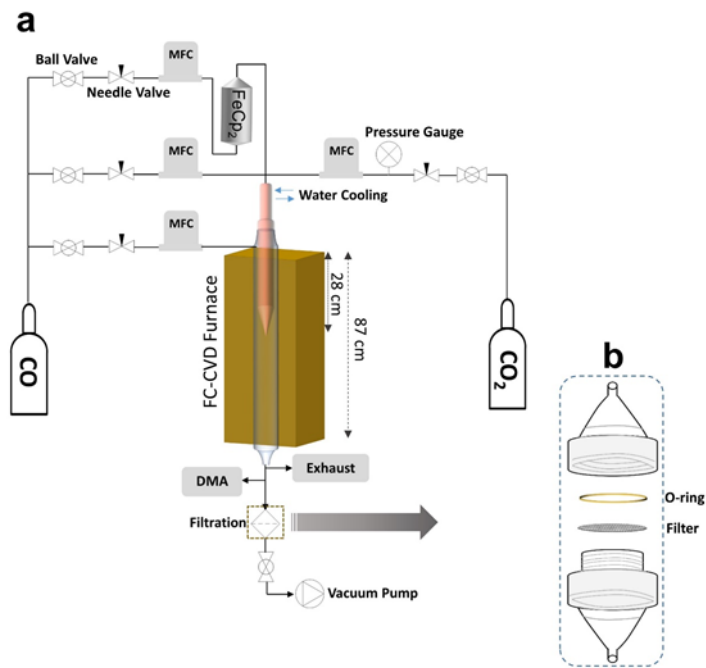


Figure 2.4: **CVD system for CNT synthesis.** (a) the schematic assembling of the used FC-CVD reactor. (b) an image of the collector for the cellulose filter used for CNT deposition. Reprinted with permission by Yongping Liao, PhD [23].

The CNT deposition plays a key role in this study and its success. Individual, bundle-free SWCNTs are needed. The standard cellulose filter deposition, as schematically shown in Fig. 2.4(b), is normally used for thin film application meaning the opposite to the needs of this experiment. Therefore, another deposition technique must be applied, one that is based on thermophoresis. This technique has a positive impact on the bundling behavior that has not been fully understood yet.

## 2.2.4 Thermophoretic Deposition

When a temperature gradient is applied to a gas that contains particles in aerosol phase, the particles experience a force pointing towards the lower part of the gradient. The motion of the particles caused by such a gradient is called *thermophoresis* [25]. The used nanoparticles are in the range of a few nanometers implying that the thermophoresis happens in the free molecular regime. But CNTs are nonspherical objects with length in the micrometer range. This makes it difficult to describe them in terms of aerosol theory. The thermophoretic terminal velocity of CNT differs from the prediction of the easiest model, where rigid body collision amongst the gas molecules is taken into account. The terminal velocity and hence the deposition rate is sys-

tematically lower than predicted and they show a slight diameter dependence. In practice, the thermophoretic deposition is realised by a plate-to-plate thermophoretic precipitator (TP) that consists of a top and bottom aluminium plate sandwiching a polytetrafluorethylene plate. The target substrate is located at the lower plate. The upper plate is heated up by two power resistors to about 100 °C and the lower part is cooled by water cooling down to about 40 °C [24]. In the experimental set-up for the electrical heating a function generator (Agilent E3633A) is used and the temperatures are measured with a thermocouple and a multimeter (Fluke 54 II B). On the upper plate the line with the CNTs coming from the reactor, as well as the vacuum line can be connected. Another big advantage over conventional filter deposition of that technique apart from the low CNT concentration is the fact that it can be used for temperature sensitive target substrates, as well.

### 2.2.5 Differential mobility analysis

In the synthesis of CNTs in a FC-CVD the goal is to reach a thermodynamically stable condition of the reactor, before one can think of the actual CNT deposition. A method is needed to somehow get feedback on what is produced by the reactor. Even though CNT synthesis has progressed massively, the methods of detection and analysis are mainly limited to transmission electron microscopy (TEM) and Ramanspectroscopy. An explanation of TEM will be given in sec. 2.3.1. Ramanspectroscopy is based on the inelastic scattering of light showing distinct features of carbon nanomaterials [16]. Atomic force microscopy (AFM) or scanning electron microscopy (SEM) can be applied, but those techniques all need a further experimental step and do not give real time feedback. Differential mobility analysers (DMAs) are widely used in the field of aerosol science. The measurement is based on the classification of the size of charged aerosol particles given their electrical mobility in an external electrical field. A certain electrical mobility is selected and a concentration measurement is carried out. Monitoring the voltage of the electric field makes it possible to determine particles within a size range [26]. The DMA consists of two concentric metal electrodes. To the inner one a negative voltage is applied, whereas the outer one is grounded. The aerosol enters the DMA. The inner core is surrounded by sheath air and the flows pass through the DMA without mixing [27]. The sheath gas flow guarantees the laminarity of the aerosol particles [28]. Positively charged particles are attracted by the inner negatively charged collector rod. [26].

A short theoretical insert is needed dealing with the motion of particles in a fluid. Reynold's

number is the ratio of inertial vs. viscous forces. Stoke's law is a solution to the general differential equation describing fluid motion. It applies when inertial forces are negligible. Most aerosol motion happens at low Reynold's numbers, therefore it can be well described by Stoke's law, given by

$$F_n = 3\pi\eta Vd, \quad (2.5)$$

here  $\eta$  is the dynamic viscosity,  $d$  is the diameter of the spherical particle and  $V$  is the velocity of the particle [25]. The electrical mobility of the particle is given by

$$Z_p = \frac{(Q_s + Q_a) \ln(R_2/R_1)}{2\pi LV}, \quad (2.6)$$

where  $Q_a$  refers to the the charged aerosol flow,  $Q_s$  to the particle free sheath air flow ,  $R_1$  and  $R_2$  to the inner and outer diameter of the DMA electrodes,  $L$  is the length of the electrode and  $V$  is the applied voltage. The electrical mobility relates to the physical particle diameter

$$d_p = \frac{neC_C}{3\pi\mu Z_p}, \quad (2.7)$$

where  $n$  is the number of elementary charges,  $e$  is the elementary charge,  $C_C$  is the Cunningham slip correction, that takes into account noncontinuum effects when calculating the drag on small particles,  $\mu$  is the gas viscosity and  $Z_p$  is the particle's electrical mobility. Cunningham slip correction is a function of the mean free path length of the considered gas molecule and the particle diameter. Particles with low electrical mobility are collected at the lower part of the rod and particles with high electrical mobility at the higher part. Narrow-ranged electrical mobility particles exit the DMA through a small slit. This is connected to a particle counter and the particle number concentration is measured. The size distribution can be gained by varying the applied voltages [27]. For the CPC a GRIMM (model number 5.414) is used and for the DMA a GRIMM electrostatic classifier ("Vienna/Reischel Type"). In the CPC the particles act as a condensation nuclei in butanol vapour. The counting is based on detecting the butanol bubbles via laser measurements. The inlet and outlet flow of the DMA is balanced with a primary flow calibrator (Gilibrator 2 Sensidyne). To avoid the impact on the DMA measurement of any charging effects during the synthesis, an aerosol neutralizer based on bipolar diffusion charging by a weak radioactive source, is interposed between the reactor and the DMA. For a detailed theoretical description of DMA consult [26].

The aim is now to connect the measured DMA data to what is synthesised by the FC-CVD based reactor. There are active or inactive conditions and only in the active one SWCNTs are formed. In Fig. 2.5 the plots of DMA measurements of several conditions are shown. For example at a

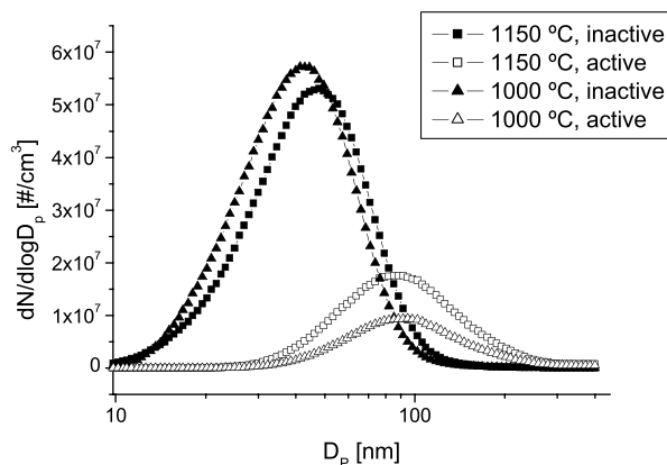


Figure 2.5: **DMA measurements.** the mobility diameter versus the number concentration from the DMA. Active and inactive conditions are shown. Reprinted from [26], Copyright (2005), with permission from Elsevier.

total number concentration of  $1.5 \times 10^7 \text{ cm}^{-3}$  and at a geometric count mean diameter of 100 nm SWCNT are grown [26].

Mobility diameters smaller than 30 nm indicate the growth of random nanoparticles. The maximum of the peak is an indication of the concentration of the collected CNTs and individuality of CNTs. The probability for aerosol particles leading to further bundling shows a quadratic dependence on the number concentration. This implies that collision can be avoided by a reduction of the CNT aerosol. At low concentration, where about 50 ccm of CO was passed through the ferrocene cartridge leading to a total number concentration of  $0.25 \times 10^6 \text{ cm}^{-3}$ , a reduced bundling behavior and an increase in length, to  $4.2 \mu\text{m}$ , can be observed. Greater mobility diameters at lower number concentrations are also believed to be caused by higher average length of the CNTs [29]. A maximum number concentration of low  $10^5 \text{ cm}^{-3}$  is needed to fulfill the experiment's requests, bundle-free individual SWCNTs.

## 2.2.6 FC-CVD of SWCNTs

Before the reactor is started by ramping temperatures up and starting the gas flows, it must be cleaned and residual waste from previous synthesis removed. The exhaust-line is connected to a DMA/CPC system. Before measurements this system needs to be calibrated. The inlet and outlet flow of the DMA is balanced to 3 slpm. For the calibration of the CPC there is a test routine provided by the manufacturer's software. A stable condition is reached when several consecutive

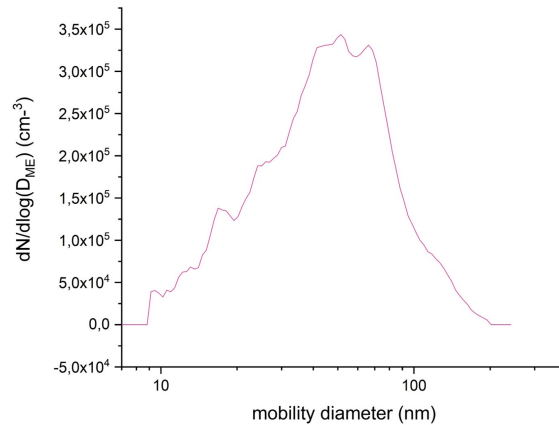


Figure 2.6: **DMA measurement.** the number concentration against the mobility diameter from the DMA measurement prior to CNT deposition.

DMA measurements deliver similar results. In Fig. 2.6 the DMA data prior to one of the CNT depositions on the TEM-grids for the experiment is shown. The mobility diameter is clearly above 30 nm, so CNTs are synthesized. The maximum number concentration  $3.4 \times 10^5 \text{ cm}^{-3}$  indicates that bundle-free individual CNTs are produced in the reactor.

The reactor can be tuned by adjusting the flows of the different gases and the temperatures at the bottom and at the top. This includes the main and secondary flow of CO, the ferrocene, as well as CO<sub>2</sub>. The total flow is always balanced to a total flow of 350 sccm. The ferrocene influences the yield significantly, where steps of about  $\pm 5$  sccm are taken. The CO<sub>2</sub> values correlate with the mean diameter of the synthesised CNTs. An increase in CO<sub>2</sub> causes a decrease in the mean diameter [30]. There are no systematic studies on the impact of temperature on the synthesis of CNTs, but a decrease in temperature from 880 °C to 750 °C increases the fraction of semiconducting CNTs [31]. In order to retrace the changes made to the synthesis, it is recommended to change only one parameter at a time, as well as wait for at least 1 h to restabilize before doing further changes and measurements.

The CNT synthesis done by myself was used for another purpose. The experimental conditions including gas flows and temperatures for that synthesis are given in Tab. 2.1. The uncertainty is estimated by the resolution of the different displays. The deposition of the CNT was thermophoretic deposition. Before the actual deposition the vacuum line of the reactor is tuned to 0.1 slm, compared to 0.3 slm in standard filter deposition, and the hot plate is heated up until an equilibrium is reached. At the same time the water cooling on the lower plate is turned on. In this deposition the higher temperature was of  $(95 \pm 2) \text{ }^\circ\text{C}$  and the lower one  $(37 \pm 2) \text{ }^\circ\text{C}$ . For the uncer-

Table 2.1: Experimental parameters of one CNT deposition in a CO-based FC-CVD system. The temperatures at the top and the bottom of the furnace, as well as the gas flows are given.

$T_{upper}$ [°C]	$850 \pm 1$
$T_{lower}$ [°C]	$830 \pm 1$
$CO_{main}$ [sccm]	$177 \pm 1$
$CO_{secondary}$ [sccm]	$102 \pm 1$
$CO_2$ [sccm]	$0.4 \pm 0.1$
$Fe(C_5H_5)_2$ [sccm]	$70 \pm 1$

tainty the thermal fluctuations throughout the time of deposition are considered. The purpose of this sample was to reach a very low CNT concentration in the order of one CNT per  $(2\mu m)^2$ . The produced CNT concentration was measured as a function of deposition time by depositing CNTs on a Si wafer piece and then the CNTs were counted in a certain area from a SEM image. This was not done by myself. To reach the requested CNT concentration a deposition time of 25 min is necessary. Compared to standard filter deposition onto holey cellulose filter this corresponds to a deposition time of 75 s. The samples used for this thesis were done by our collaborators Aqeel Hussain and Saeed Ahmad at Aalto university in Prof. Kauppinen's group. They used a slightly different set-up than the one described. The method is based on ethylene ( $C_2H_4$ ) as a carbon source.  $H_2$  and  $N_2$  are used as additional carrier gases and as a catalyst ferrocene mixed with silicon oxide powder is used [32]. These changes have no impact on the basic principle of the FC-CVD method and has no implication on the present study. Unfortunately, there is no detailed documentation on the samples in terms of exact experimental conditions such as DMA data, gas flows and furnace temperatures.

## 2.3 Scanning transmission electron microscopy

### 2.3.1 Basic principle

The basic principle of an electron microscope (EM) is the use of electrons to generate an magnified image. The electrons can be transmitted or interact with the atoms and the electron cloud of the specimen and are scattered. The main processes of interaction can be divided elastic and inelastic scattering. In elastic scattering the incoming electron with negative charge is scattered at the positively charged nucleus, the direction of propagation is changed, but the energy is conserved.

In inelastic processes the electron interacts with the electron cloud and the energy of the electron is changed. For a complete list please consult [33].

Following the particle-wave dualism of de Broglie an electron at an acceleration voltage of  $V_0$  of 60 keV has an relativistic wavelength of

$$\lambda = \frac{h}{\sqrt{(eV_0/c)^2 + 2m_0eV_0}} \simeq 3.5 \text{ pm}, \quad (2.8)$$

where  $h$  is Planck's constant,  $c$  the speed of light,  $e$  the elementary charge and  $m_0$  the rest mass of the electron [33]. In transmission EM (TEM) thin samples ( $D < 100 \text{ nm}$ ) are used. There are two techniques available in TEM and they differ in the way they approach the specimen. TEM is a wide-beam technique. The electron beam is close to parallel and the image is formed by an objective lense after the specimen and collected in parallel. Instead in scanning TEM (STEM) the electron beam is focused finely by a lens before the specimen. The sharply focused beam is scanned over the sample in a raster pattern. Every scattering event, that has a certain intensity, is detected separately and build up to an virtual image by correlating the scattering intensity to the known scanning position [34]. Annular dark field (ADF) detectors, like shown in Fig. 2.7, are made of a ring like structure and are located after the specimen. The transmitted electrons or electrons with little deviations from the center building up the bright field (BF) are not detected. The medium angle ADF (MAADF) used in this thesis covers a detection range of 60-200 mrad. As only higher angle deviations are considered, the process can be regarded as Rutherford scattering [33]. The differential cross section of the process is given by

$$\frac{\sigma_R}{d\omega} = \left( \frac{1}{4\pi\epsilon_0} \frac{Ze^2}{4eV_0} \right)^2 \frac{1}{\sin^4(\theta/2)}, \quad (2.9)$$

where  $Z$  is the atomic number and  $\theta$  the scattering angle [35]. The detected intensities depend on the atomic number  $Z$  of the scattering atom [33]. The exact  $Z$ -dependence depends on the signal collection geometry, but is expected to be in  $Z^{1.5-1.8}$  range [36].

The electrons originate from an electron gun. Its purpose is it to deliver a steady stream of ideally monochromatic (constant kinetic energy) electrons. To describe the gun as a point source, the electrons should emanate from one single point [37]. There are two main types of electron sources, thermoionic and field emission guns. Only the second ones are relevant in the present case. The field emission gun (FEG) consists of a sharp tungsten tip and two sets of anodes, where the first is responsible for the acceleration and the second for the focus of the electrons. In FEGs strong electrostatic fields are applied to induce electron emission. High energy electrons tunnel through the potential barrier and are released. UHV ( $10^{-11} \text{ mbar}$ ) is needed at the gun. The

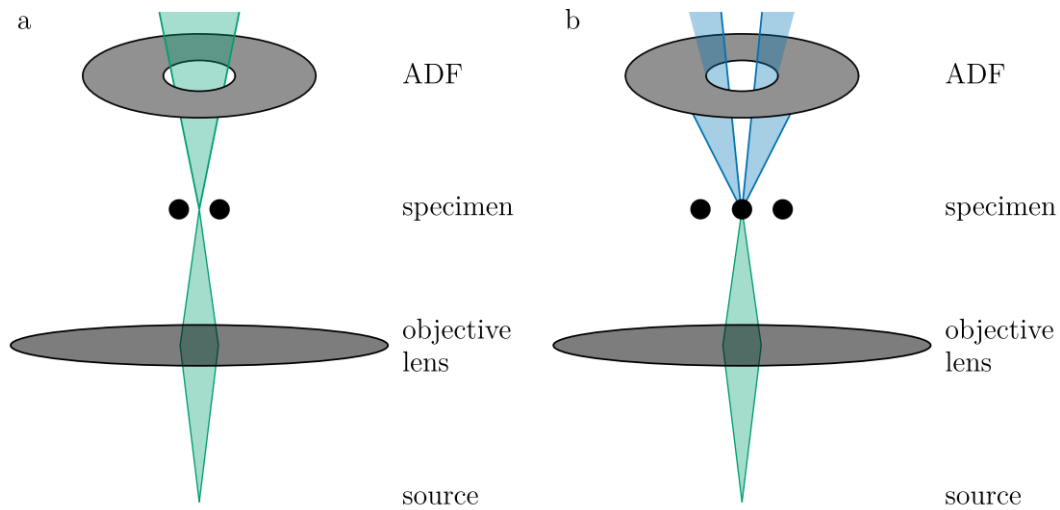


Figure 2.7: **ADF imaging.** (a) the focused electron with little deviation passes through the detector. (b) a scattered beam results in a signal, reprinted with permission of Greogor Leuthner, PhD [35].

emission area is in the order of nanometers. They are superior to thermoionic source in terms of higher spatial resolution, higher brightness and better signal to noise ratio [38].

Usually round electromagnetic lenses are used to focus the electron beam. These consist of a circular current-coil surrounded by a high permeability yoke with specially designed pole pieces. The magnetic field is controlled by controlling the current. The motion of the electrons is described by the relativistic motion of charged particles in an external magnetic field. The driving force of the deflection is the Lorentz force [37].

### 2.3.2 Aberrations, resolution and image quality in STEM

Electromagnetic lenses are not perfect and therefore show aberrations. Apart from the geometric aberrations inherent to the lenses, there are also chromatic aberrations. These depend on the energy spread of the electron source, fluctuations in the acceleration voltage or other energy losses yielding from the interaction of the sample. The problem arises from the fact that electrons with different wavelengths are focused onto different points. The disc diameter for this aberrations can be related to the energy spread  $\Delta E$ , the collection semiangle  $\alpha$  of the lens and the chromatic aberration factor  $C_c$ , as follows [34]

$$d_c = C_c \alpha \Delta E / eV_0. \quad (2.10)$$

The geometrical optical aberrations can be described by the wave aberration function  $\chi$ . It gives the phase difference between the perfect wave and the actual wave in terms of axial angle  $\theta$  and azimuthal angle  $\phi$  [39]. In a Taylor series expansion, the geometric aberrations are denoted by  $C_{m,n}$ .  $m$  is the order of the aberration and  $2\pi/n$  is the smallest rotation angle that gives the same phase shift. The orthogonal components of the same aberration with non-cylindrical symmetry are specified with  $a/b$ . The aberration function up to third order reads

$$\begin{aligned}\chi(\theta_x, \theta_y) = (2\pi/\lambda)\{ & C_1(\theta_x^2 + \theta_y^2)/2 + C_{1,2a}(\theta_x^2 - \theta_y^2)/2 + C_{1,2b}\theta_x\theta_y + \\ & C_{2,1a}\theta_x(\theta_x^2 + \theta_y^2)/3 + C_{2,1b}\theta_y(\theta_x^2 + \theta_y^2)/3 + C_{2,3a}\theta_x(\theta_x^2 - 3\theta_y^2)/3 + \\ & C_{2,3b}\theta_y(3\theta_x^2 - \theta_y^2)/3 + C_3(\theta_x^2 + \theta_y^2)^2/4 + C_{3,2a}(\theta_x^4 - \theta_y^4)/4 + \\ & C_{3,2b}\theta_x\theta_y(\theta_x^2 + \theta_y^2)/2 + C_{3,4a}(\theta_x^4 - 6\theta_x^2\theta_y^2 + \theta_y^4)/4 + \\ & C_{3,4b}(\theta_x^3\theta_y - \theta_x\theta_y^3)^2/4\},\end{aligned}\quad (2.11)$$

where  $\lambda$  is the electron wave length, and  $\theta_x$  is  $\theta \cos(\phi)$  and  $\theta_y$  is  $\theta \sin(\phi)$  [40].  $C_{0,1}$  is the simple image shift.  $C_{1,2}$  is the two-fold axial astigmatism.  $C_{1,0}$  is the defocus.  $C_{2,3}$  is the three fold astigmatism. Astigmatism appears when rays in perpendicular planes have different foci.  $C_{2,1}$  is the axial coma. This aberration is due to relative angle between the incoming probe and the optical axis.  $C_{3,2}$  is the axial star aberration or also called third-order two-fold astigmatism.  $C_{3,4}$  is the four-fold astigmatism.  $C_{3,0}$  is the third order spherical aberration due to the fact that electrons are focused differently depending on their radial distance on the optical axis. For a detail description of the higher order aberrations please consult [41].

The only higher order of interest here is the  $C_{5,0}$ , that is the fifth order spherical aberration. The most important lower order aberrations are spherical aberrations, astigmatism and coma. The diameter of the disc of confusion for spherical aberration can be expressed by

$$d_s = \frac{1}{2}C_s\alpha^3,\quad (2.12)$$

where  $C_s$  is the spherical aberration coefficient and  $\alpha$  the collection semiangle of the lens [34].

Also aberration-free lenses show diffraction effects when a point source is imaged, as only a portion of the wavefront is collected. The intensity profiles oscillates and concentric rings are visible. The diameter of the central disk, is called Airy disk.

Points in the image that are next to each other have both this disc-like features. The resolution can be measured by how close the points can join in order to be still able to distinguish them into different sources. In the Rayleigh criterion the resolution is defined as the radius of the Airy disk.

The distance when the maximum of one intensity meets the first minimum of the second one is considered. The resolution is given by

$$r_d \approx \frac{0.61\lambda}{\alpha}, \quad (2.13)$$

where  $\lambda$  is the wavelength [34].

When considering eq. (2.12) and eq. (2.13) it is apparent that spherical aberrations increase and diffraction effects decrease with increasing aperture semiangle  $\alpha$  and vice versa. Therefore, an optimum value for  $\alpha$  has to be found. When only these two aberrations are considered, the radius of the total disc of confusion for the optimum  $\alpha$  gives

$$r_{tot} = 1.21\lambda^{3/4}C_s^{1/4}. \quad (2.14)$$

The image quality in STEM does not only depend on the resolution, but also the collected signal is important. The signal to noise ratio can be quantified by

$$\text{SNR} = \frac{\mu}{\sigma}, \quad (2.15)$$

where  $\mu$  is the mean value of the signal and  $\sigma$  the standard deviation of the noise. In the Rose criterion SNR must exceed 5 in order to observe image details [35].

Spherical aberrations are the key factor in limiting resolution in TEM. Round magnetic lenses have a positive spherical aberration and can therefore not be used to correct those aberrations. Multipole lenses with negative spherical aberrations are used to correct them [34]. In the Nion UltraSTEM 100 octupole and quadrupole lenses are used [42].

### 2.3.3 Nion UltraSTEM 100

In the experiment a Nion UltraSTEM 100 is used. In Fig. 2.8(a) an image of the instrument and in Fig. 2.8(b) a schematic cross section is given. The microscope's original design consists of the following part, where the path of the imaging electrons is followed. Firstly a 100 kV VG cold field emission gun can be found, then a pair of deflector to steer the beam, three round condenser lenses and in between them the virtual objective aperture (VOA). The  $C_3/C_5$  aberration corrector is followed by a quadrupole lens module that couples the corrector to the objective lens. Then one can find the objective lens (OL), a sample chamber containing the sample stage, four round projector lenses. After that comes the detector column. This contains a high angle annular dark field (HAADF) (80-240 mrad), a MAADF (40-60 mrad) detector, a beam stop to record diffraction

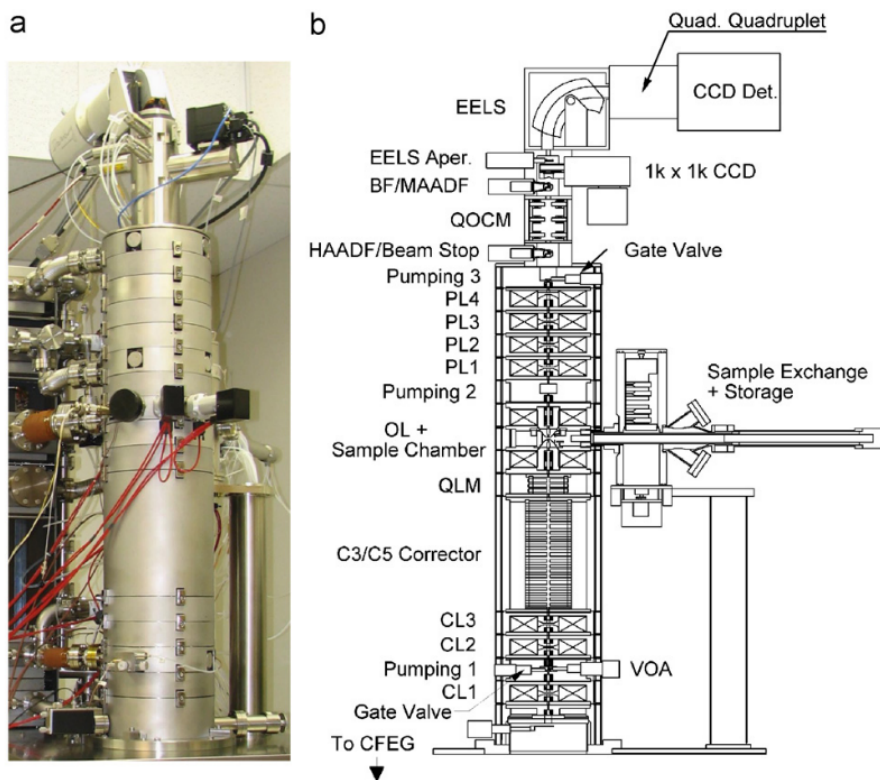


Figure 2.8: **Nion UltraSTEM 100**. (a) an image of the Nion UltraSTEM 100. (b) a schematic cross section with all essential parts. Reprinted from [42], Copyright (2007), with permission from Elsevier.

pattern, a bright field (BF) detector and a CCD (charged-coupled device) camera. The camera uses a 1k×1k chip and 15 MHz read out rate. Finally a quadrupole-octupole coupling module to couple inelastically scattered electrons and a EELS system can be found.

The  $C_3/C_5$  aberration corrector consists in 12 roatable quadrupoles and three quadrupole–octupoles. They allow the correction up to third order aberrations, as well as the principle fifth order spherical aberration [42]. The measuring of the aberration coefficients is based on the Ronchigram method. The beam is shifted on amorphous structures and the local magnifications are measured [35]. The scanning of the electron beam is done by two sets of fast deflectors that are contained in the lower and upper part of the OL. The energy spread of the electron source is about 0.3 eV. The MAADF detector is made of a single crystal scintillator connected to a photon multiplier tube (PMT). The vacuum-system is exclusively dry and the pre-pump is provided by turbo pumps. For the rest, ion getter pumps are used. The vacuum is usually in the  $10^{-9}$  Torr range. The resolution achieved in the image depends on the probe size and current and the interaction of the beam and the sample. The geometric aberrations for a 60 keV beam in the used system gives  $0.51 \text{ \AA}$ . The chromatic aberrations for 60 keV are  $0.97 \text{ \AA}$ . There is another factor that is independent on the

aberrations and that is the size of image of the demagnified Gaussian distributed electron source. In the used system the  $d_{source}$  is about 0.5 Å. Therefore, the total probe size yields 1.1 Å [42]. The diffraction limit following eq. (2.13) at 60 keV and  $\alpha = 30$  mrad in the used system yields 0.98 Å. When the probe current tends to zero, the probe size reaches its minimum, as there is no Gaussian contribution. In practice there must be a reduction in the demagnification in order to get a current in the probe [34]. In the used system the electron current is about 60 pA. To give some relevant numbers, if one wants to increase the current to 0.5 nA,  $d_{source}$  needs to be increased to 1.5 Å. The electron current as a function of  $d_{source}$  is given by

$$I = B\pi^2 d_{source}^2 \alpha^2 / 4, \quad (2.16)$$

where  $B$  is the brightness of the source and  $\alpha$  the collection semiangle [42].

In part of the experiments in this thesis the UHV of the STEM is replaced by controlled low-pressure atmospheres by controlled hydrogen, oxygen or water. A schematic overview of the experimental set-up for that is given in Fig. 2.9(a). For the H<sub>2</sub> a HIG Minican is used. For Ar and O<sub>2</sub> commercially available gases (Linde) and for the H<sub>2</sub>O standard distilled water is taken. The set-up consists of a leak line connected to the microscope column and to the cylinders of the different gases. A membrane pump (Pfeiffer MVP 15 l/min) is used to pump out residual air from the line. A leak valve at the column that is regulated by a micrometer screw. The pump and the different gas bottles can be detached from the central line leading to the microscope via valves.

The local atmosphere of the microscope is not defined very well. The composition in terms of

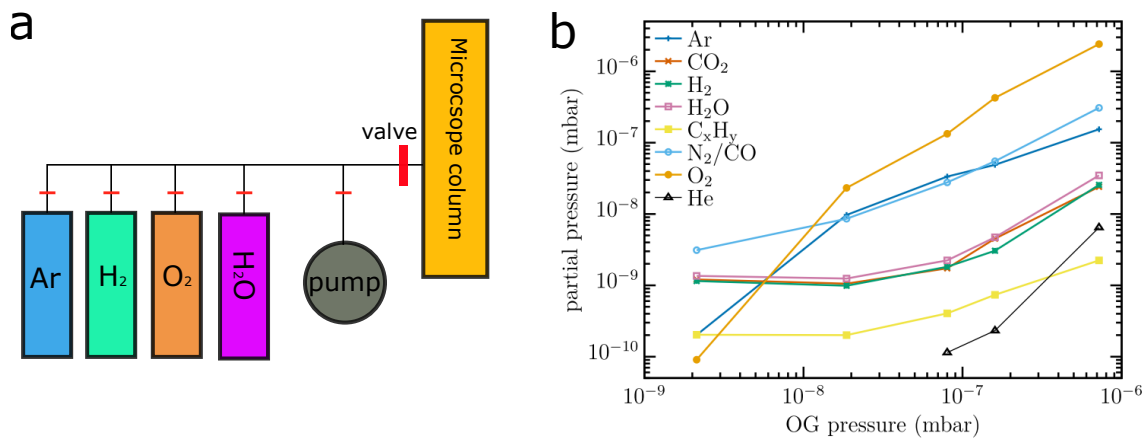


Figure 2.9: **Leakage set-up and relevant pressures.** (a) the essential parts of the experimental set-up for the leakage experiment. (b) the partial pressures as a function of different OG pressures under oxygen atmosphere, adapted from [2] (CC BY 3.0).

molecules of the residual vacuum with oxygen atmospheres was measured by [2] with a mass

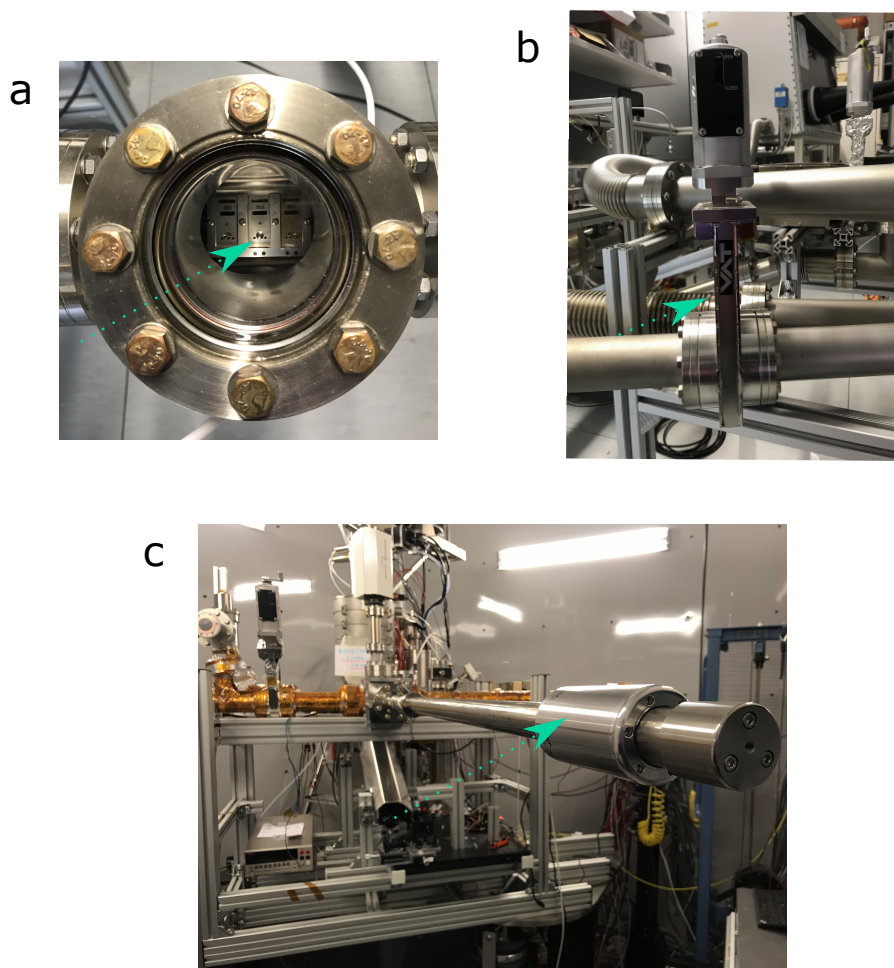


Figure 2.10: **Experimental set-up of the Nion UltraSTEM 100.** (a) a car from a view port of the UHV system, the TEM-grids are contained in the puck. (b) is an image of a gate valve. (c) the arm used for the sample exchange connected to the Nion UltraSTEM.

spectrometer (Pfeiffer Prisma QME200) connected to the sample area of the microscope. The molecular current as function of atomic number was determined. After calibration these values can be converted into partial pressures as function of objective gauge (OG) pressure measured in the microscope. The measured partial pressures as a function of OG pressures can be seen in Fig. 2.9(b).

The Nion UltraSTEM 100 is further equipped with a customized UHV system consisting in ducts. There are several valves reaching the microscope (Fig. 2.10(b)). The samples are contained in specially designed sample holders inserted in "cars" that can be driven by magnets from outside to the microscope (Fig. 2.10(a)). The sample can quickly be inserted and extracted from the microscope by a specially designed arm (Fig. 2.10(c)).

In the following a general experimental approach for Nion UltraSTEM will be given. Before driving the car near to the microscope insertion arm the pressure must be checked and has to be in

low  $10^{-8}$  mbar range. Then the first and second valve are opened and closed right away. Then the puck that contains the sample can be extracted by the specially designed arm and inserted into the microscope column. Before inserting the sample into the microscope column, the pressure in the arm is checked that should be in low  $10^{-9}$  mbar range, the sample stage must be zeroed and another valve must be opened. When the puck is inserted the valve is closed again. Whenever the sample is exchanged this procedure of checking the pressures and putting the stage to zero must be repeated.

If the experiment is done as the first session of the day, the backplanes are demagnetized. The electron beam is turned on. The CCD mode is selected and the zero of the defocus is searched. The first part of the tuning is done in this mode. The VOA is put in and is centered by a routine provided by the manufacturer's software. Then at a defocus of about  $-1500$  nm the image in the

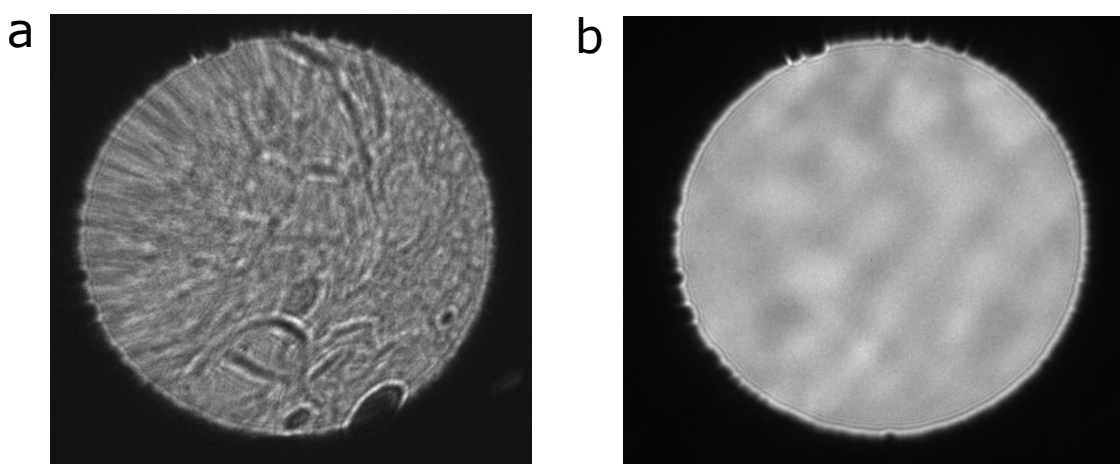


Figure 2.11: **Aberations and Ronchigram.** (a) an image of the CCD camera at roughly  $2000$  nm defocus, higher order aberrations can be seen. (b) shows the ronchigram at zero defocus after the tuning algorithm converged.

CCD is checked. If the higher order aberrations are too much off, as can be seen in Fig. 2.11(a), the tuning algorithm will fail. In this case a rough manual tuning to adjust the quality of the image must be done. The coma a/b is corrected in  $5-10$   $\mu\text{m}$  steps. Then the tuning algorithm is applied initially at a defocus of about  $-1500$  nm. The measured values of the algorithm can be corrected and the algorithm shows the measured values with respect to a required interval for each aberration, separately. Firstly only the aberrations up to second order are measured and corrected, iteratively. If higher orders are off in several consecutive measurements, those need to be corrected. Then again the lower orders must be measured and corrected. Considering the principle to measure aberrations it is essential to tune on amorphous material or on crystalline one with considerable amount of amorphous contamination. After some iterations the high tension (HT)

wobble is applied in 50 V steps to see if the electron beam is centered. If the values start to converge the defocus is decreased to about  $-650$  nm, this is the defocus where the tuning algorithm is optimized at. Once all values converge to 100% in repeated measurements, the ronchigram close to zero defocus looks like in Fig. 2.11(b). Some astigmatism can still be observed (line-like features), but no higher orders. At zero defocus the operating mode of the microscope is switched to scan-mode and the MAADF detector is put. The images that are recorded in scan-mode are characterized by the field of view (FOV), the amount of pixels and the dwell time that refers to the time that the electron beam spends on every pixel. The final step of the tuning of the astigmatism must be done manually in this mode. Firstly, the defocus is adjusted at a FOV of about 512 nm ( $512 \times 512$  pixels and  $8 \mu\text{s}$  dwell time) and the astig a/b are corrected by 10 nm steps. This is done iteratively. The resolution of the image must be optimized. Then the FOV is decreased to 64 nm and firstly the defocus is corrected. Then the astig a/b is adjusted in 2 nm steps. The FOV is decreased further. Crystalline particles that show atomic features are very useful when tuning the microscope at this stage. It is helpful to calculate the FFT of the images, as they show distinctive diffraction maxima. If the defocus is roughly within 5 nm, one should switch from the mechanical defocus adjustment of the stage to the fine focus of the electron beam. The final tuning is ideally done on atomically resolved graphene at FOV of 3-5 nm at  $1024 \times 1024$  pixels and  $16 \mu\text{s}$  dwell time. The astig a/b is corrected by 1 nm steps and a final adjustment of the coma a/b is done by varying it by 100 nm steps. Temperature stability is vital when it comes to maintain tuning over several hours. A temperature drift of about  $0.1 \text{ }^\circ\text{C/h}$  is the threshold value for loss of tuning. Particularly important is the temperature of the objective lens. If the tuning is lost, one can try to make some adjustments to the astig a/b, as well as the coma a/b. If this doesn't work, the same procedure including the tuning algorithm in CCD mode and the final adjustment in scan-mode, as just described, must be repeated.

### 2.3.4 Diffraction pattern of carbon nanotubes

In the structural characterization of CNTs there are two broad classes, i.e optical and non-optical techniques. Optical methods that use optical transition energies and relate it to the chirality-dependent band gaps have insufficient spatial resolution. The second class is widely based on electron diffraction. The method proposed is completely calibration-free. Fig. 2.12 shows a simulated electron diffraction pattern (EDP) of a (12,7) CNT.  $d_i$  stands for the interlayer spacings and  $\alpha$  denotes the chiral angle. Along the equatorial line the dominant Bessel function is  $J_0(\pi D_0 R)$ ,

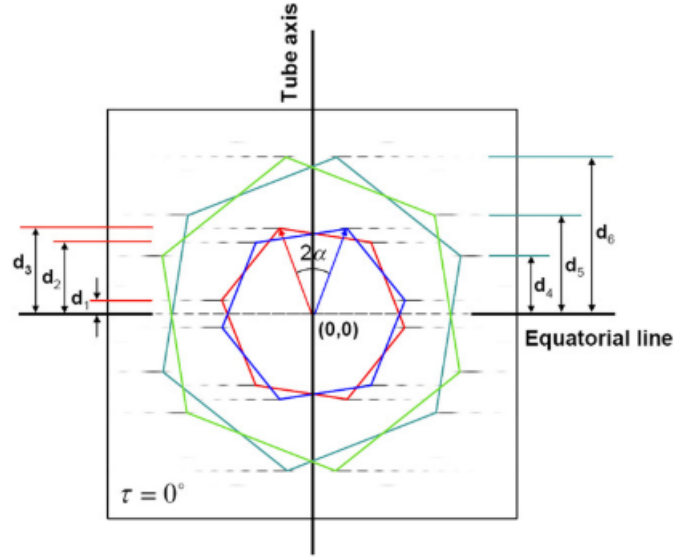


Figure 2.12: **Diffraction of CNTs.** a simulated electron diffraction pattern of a (12,7) CNT.  $\tau$  stands for the tilt angle and  $d_i$  for the interlayer spacings. Reprinted from [43], Copyright (2006), with permission from Elsevier.

where  $D_0$  is the tube diameter and  $R$  the radial distance along the equatorial line. Using a valid approximation for arguments  $\gg 0$ ,  $\sqrt{\frac{2}{\pi x}} \cos(x - \frac{\pi}{4})$ , the roots are found at  $x_j = \pi D_0 R_j = (j-1/4)\pi$ . So the diameter can be found along an intensity profile along the equatorial line, with  $D_0 \cdot \delta = 1$ , where  $\delta = R_{j+1} - R_j$ . Introducing the *intrinsic interlayer spacings*  $\xi_i = D_0 \cdot d_i$  and some geometrical observations the chiral indexes  $(n, m)$  are given by [43]

$$n = \frac{\pi}{\sqrt{3}}(2\xi_3 - \xi_2), \quad m = \frac{\pi}{\sqrt{3}}(2\xi_2 - \xi_3) \quad (2.17)$$

or equivalently,

$$n = \frac{\pi}{\sqrt{3}}(3\xi_3 - \xi_6), \quad m = \frac{\pi}{\sqrt{3}}(2\xi_6 - 3\xi_3). \quad (2.18)$$

### 2.3.5 Hydrocarbon contamination in (S)TEM

In order to atomically resolve images in (S)TEM, well-prepared samples are necessary and especially any surface contamination obfuscates samples. Usually CVD-grown graphene is transferred onto TEM-grids with a PMMA-mediated transfer technique. The PMMA is removed with solvents. PMMA and other hydrocarbon residuals are left behind and the view in a (S)TEM is nearly almost obscured by contamination. The general approach to get rid of that contamination involves thermal annealing.

Another problem is that samples show e-beam induced organic deposition, where mobile contaminants cover the originally clean surface during imaging in the (S)TEM [44]. There are other four factors, apart from the specimen preparation history, that influence the amount of hydrocarbon contamination. Those are the sticking coefficient of the hydrocarbons, the existing contamination in the vacuum system of the microscope, the level of the vacuum and the electron probe current density [45].

To minimize the problem of hydrocarbon contamination the samples are introduced into the ultra high vacuum system of the microscope via a standard 12 h 130 °C vacuum bake to get rid of an excess of hydrocarbon contamination. Further two cleaning techniques are applied.

Firstly, a dry-cleaning technique with active carbon is used. The technique is based on the fact that active carbon is a good absorbent of organic impurities. The experimental set-up for this technique consists in a commercially available furnace with tunable temperature. In the furnace there is a block of aluminum (20×20×4 cm) in order to keep the temperature stable. In the center of the block there is a hole where the active carbon is put. A thermocouple is connected from the center of the active carbon to a voltmeter (FLUKE 179 Multimeter) to measure the temperature exactly. The TEM-grids are embedded into activated carbon powder and eventually heated from room temperature to 210 °C and held there for 30 min. After that the TEM-grids are taken out of the active carbon and are blown clean with air. In the study, which this method is based on, HRTEM images are taken before and after the cleaning treatment. The technique produces atomically clean graphene in  $\mu\text{m}^2$  size. When considering the ratio of clean and contaminated areas visible in the TEM images, the cleanliness in commercially available standard graphene improves from 6% to 95%. The procedure works only with single layer graphene, bilayers remain contaminated [46].

The second cleaning technique is *pre situ* annealing by laser induced heating. Experimentally, a high power diode laser (445 nm, tunable up to 6 W, Lasertack GmbH) was used. The laser spot size is 1 mm<sup>2</sup>. The laser enters the microscope column through a view port and targets directly the sample. The distance between the laser and the sample is 40 cm. 600 mW (10% duty cycle) for 2 min results in visibly cleaner samples. This laser is operated with a pulse modulation. The pulse frequency as well as the maximum intensity in % can be adjusted. The temperature during the heating is estimated with 1100-1300 °C. When increasing the power higher the gold support of used TEM-grids starts to melt and the sample is destroyed. The treatment brings significantly cleaner graphene with clean areas in the size of several hundreds nm<sup>2</sup> [7]. Two slightly different

systems are used throughout the experiments for this thesis. The first one is the one that has been just described. The second one consists in a Cobolt Blues<sup>TM</sup> 50 (473 nm) laser and the beam is brought to the sample with an optical system. It will be stated in the experimental section which one was used. The basic principle is the same. The major improvement of the second one is the alignment between the electron beam and the laser spot can be adjusted. Ideally the laser hits at the spot that is imaged in the microscope. The advantage of the laser cleaning is that the sample doesn't have to be exposed to air as the cleaning procedure happens within the microscope's vacuum. The downside is that it can lead to damage of the TEM support grids.

## 2.4 CNT-graphene van der Waals heterostructure

Having introduced the main methodology of the present study the focus should now be put on the 1D-2D carbon VdWHs and what is known about it.

From a recent STEM study done by [8], we get an idea how the used VdWHs looks like atomically (Fig. 2.13). The circles are the average atom positions perpendicular to the tube axis of a tilt series (300 mrad) of the graphene layer right next to the CNT. The fitted data were put into an atomistic simulation. The cross section of the interface of two different tube diameters is presented [8].

It becomes apparent that there are structural changes due to the VdW interaction. The deformation of the graphene layer and the "flattening" of the CNT are evident. What is surprising from the applied model is that larger diameter CNT like the (30,5) (Fig. 2.13), are effected more, which is interesting, as it is opposed to the decrease in curvature in pristine CNTs with increasing tube diameters. The curvature of the graphene layer can also play an interesting role. The electronic and phononic properties, that are expected to undergo changes, relevant for this study, will be treated in the following.

Curving graphene can imply three microscopic impacts. Firstly, the distance between carbon atoms can be altered. Secondly, a rotation between the  $p_z$  orbitals can be caused. Lastly, the  $\pi$  and  $\sigma$  bonds can be rehybridized. Periodic corrugations lead to the opening of a band gap that can be tuned by the amplitude and period of the curvature [47]. A DFT study [48] on a semiconducting (8,0) ( $d = 0.63$  nm) CNT provides information. They investigate the radial deformation by applying stress to the opposite sides in  $y$ -direction to the cross section of the tube. The amount of stress is parameterized by  $\eta = \frac{R-R_y}{R}$ , where  $R$  is the radius of the perfect CNT and  $R_y$  is the semi-minor axis in  $y$ -direction. The degeneracy of the energy bands is increased. As  $\eta$  increases

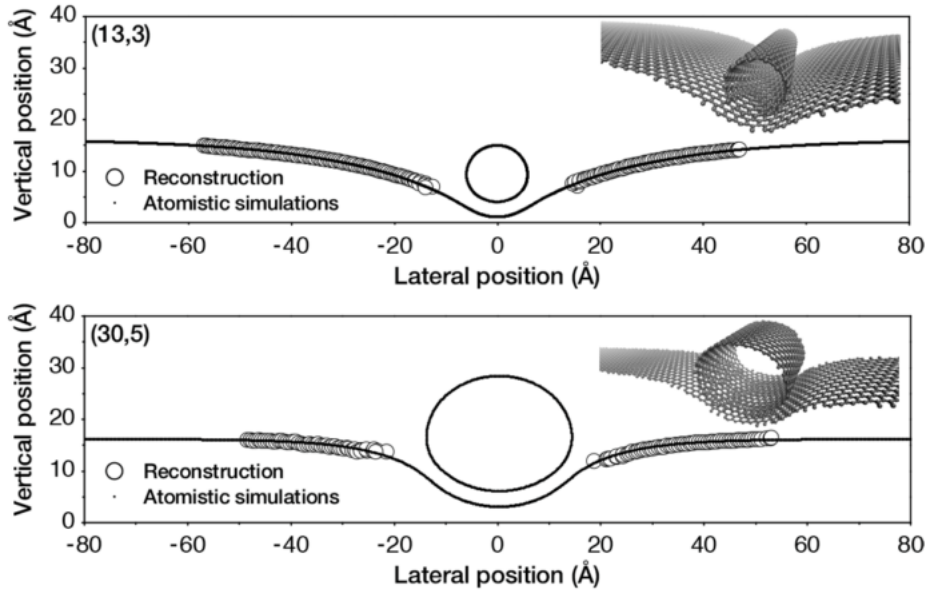


Figure 2.13: **Carbon 1D-2D heterostructure.** the atomic structure of the used graphene-CNT VdWHs, the number pairs correspond to the chiral indices  $(n, m)$ , figure adapted from [8] (CC BY 4.0).

the lowest conduction band moves towards Fermi-level. The energy bands near the Fermi-level are mainly composed of the atoms with highest curvature. At  $\eta$  equal to 23% the highest valence band reaches Fermi-level and meets the lowest conduction band. The  $\sigma - \pi$  orbital hybridization at the edges with the highest curvature is responsible for this semiconductor-metal transition. From the study [8], it can be observed that the (30, 5) CNT ( $d = 2.57$  nm) is by far more affected by the flattening than the smaller CNT. The  $\eta$  is of 7.2% for the large tube, when an ellipse is fitted the data of Fig. 2.13 and negligible for the smaller one. Similar maximal curvatures like in the study [47] are not reached for two reasons. On the one hand, the flattening itself is not strong enough and on the other hand, with decreasing diameter the CNTs are negligibly affected by the flattening mechanism. Therefore no drastic changes in the electronic structure of CNTs are to be expected.

The easiest and noninvasive way to measure the phononic properties is Ramanspectroscopy. Raman involves the inelastic scattering of light.  $Sp^2$ -hybridized carbon has only few Raman active modes leaving a characteristic signature [14]. In the scattering event an electron is excited from the valence band to a virtual state. The excited electron is scattered and emits or absorbs a phonon. Finally, the electron relaxes in the valence band and emits a photon [16]. The G-peak corresponds to the double degenerate optical in-plane modes and is found around  $1580\text{ cm}^{-1}$ . In this study [49] graphene is transferred onto a flexible substrate, with two- and four-point

methods strain is applied leading to a uniform curvature of graphene. During the application of strain, Raman spectra are recorded. When graphene is curved the symmetry is broken leading to a phonon component parallel and perpendicular to the direction of applied strain axis. This splits the G-peak into two separate features like in the case of CNTs [49]. There is another characteristic feature in the Raman spectra of CNTs, the RBM found between  $100\text{ cm}^{-1}$  and  $500\text{ cm}^{-1}$  [16]. In a recent study [50] with plasma CVD-seed grown graphene with wrinkled morphology, radial modes (RMs) in the range of about  $100\text{--}500\text{ cm}^{-1}$  are revealed. The existence of additional Raman features in the low-energy range have been suggested by simulations before. The Raman shifts depend on the arc length and the curvature. With growing arc length the Raman peak increases, but gets lower with increased curvature [50].

## 2.5 Irradiation damage in STEM

### 2.5.1 Damage in low-dimensional carbon materials

In TEM, high energy electrons pass through a specimen. At prolonged exposures beam damage is inevitable especially to light and non-metallic materials. The damage is due to three main mechanisms: (i) knock-on damage caused by elastic electron scattering, (ii) excitations and ionization of the material caused by inelastic scattering and (iii) chemical reactions between specimen and residual gas molecules that are split under the electron beam. In graphene because of its high electron mobility the only damaging mechanism at ultra high vacuum (UHV) ( $10^{-10}$  mbar) is knock-on damage [1]. The life time of an electron-hole pair in graphene is about 100 fs [51] compared to about 4 ns between scattering events for a 40 pA current beam. The displacement threshold energy, the energy required to displace an atom by a knock on event, has been shown to be between 18 eV and 22 eV in experiments. This corresponds to to an electron energy of 90-100 keV [5]. In the experiments leading to this thesis an electron acceleration voltage of 60 keV is used, so atoms are not displaced by knock-on damage [1]. The formation of a Stone-Wales (SW) defect is possible by transforming four hexagons of the graphene lattice into two pentagons and two heptagons. This is done by a bond rotation of  $90^\circ$  of a carbon-carbon bond [5]. In the case of knock-on damage, the electrons transfer energy to the sample through statistically distributed knock-on events. This process is Poisson-distributed and becomes less likely with increasing electron dose. The mean electron dose can be accessed by likelihood minimization to the experimental values [52]. To compare theory and experiment the cross section  $\sigma$  for the process is given

by

$$\sigma = \frac{1}{\lambda\rho}, \quad (2.19)$$

where  $\lambda$  is the mean electron dose to create the defect from the minimization and  $\rho$  is the sheet density of graphene [35].

In the following the damaging mechanism of CNTs in electron microscopy will be discussed.

## 2.5.2 Electron irradiation of CNTs

Irradiation of electrons in CNTs induces atomic displacement mainly due to knock-on collisions due to their electronic structure. This prevents radiolytic processes from taking place. Theoretically, the knock-on cross section is described as Coulomb scattering of the relativistic electrons and the nuclei that was derived by Mott as a solution of the Dirac equation. The considered transferred energies are at order of magnitude of the bonding energy, therefore the neighbors of the knocked atom need to be taken into consideration, as well. The *total displacement cross-section* is given as the integral of the cross-section over an energy domain,  $\sigma_d = \int_{S(T>E_d)} \sigma(T) \frac{4\pi}{T_{max}} dT$ .  $E_d$  is the threshold energy corresponding to the energy necessary to displace an atom from the lattice and  $T_{max} = 2ME(E + 2mc^2)/((M + m)^2c^2 + 2ME)$  is the maximum transferred energy, where  $M$  and  $m$  denote the mass of the nucleus and the electron, respectively [53].

But only when considering an isotropic threshold energy function  $E_d$ , an analytical expression can be given. In crystalline materials this is barely fulfilled. The minimum threshold energy is orthogonal to the plane 23 eV, based on density functional based tight binding (DFTB) calculations. When relativistic elastic scattering of the electron at the nucleus is considered, a maximum of 23 eV are transferred to the nucleus by an electron of 113 keV. The highest threshold energies are found for in-plane movement of the atoms where big distortions are induced to the lattice during the ejection process [53]. After the removal of one atom it is remarkable that the cross section for this under coordinated atom is one order of magnitude higher than in the pristine graphene lattice (13.4 b). The calculation is done for a electron beam energy 20 keV above threshold energy. There is a strong asymmetry between the upper and the lower part of the CNT. Structurally, the doubly coordinated atom yields in a dangling bond vacancy. When another atom is removed from the CNT, one ends up having a divacancy. This two models can be applied to odd- and even-numbered vacancies, respectively [54].

Primary vacancies, where only very few atoms are missing, act as seeds for the growth of dislo-

cation lines in the CNTs. Dislocations with different orientations in a (20,5) CNT with 12 missing atoms are shown in Fig. 2.14. There is an impact on the tube diameter. For example, the diameter changes from 2.0 nm to 1.8 nm in Fig. 2.14(c),(d). The second impact, which considering the electronic properties is even more interesting, is the local change in chirality of the CNT from  $(m, n)$  to  $(m \pm n, n \mp m)$  [54].

It might be useful to make an example and give some relevant values. Taking an armchair (8,8) CNT the threshold energy  $T_d$  is about 20 eV. Assuming a single vacancy, i.e. dangling bond as just discussed, the threshold energy is about 14 eV with weak dependence on the tube diameter. Instead, a double vacancy has a larger displacement threshold of about 18 eV, because no doubly coordinated atom is found in this structure. Note that a threshold energy of 12 eV corresponds to a kinetic energy of the electrons of 66 keV [55].

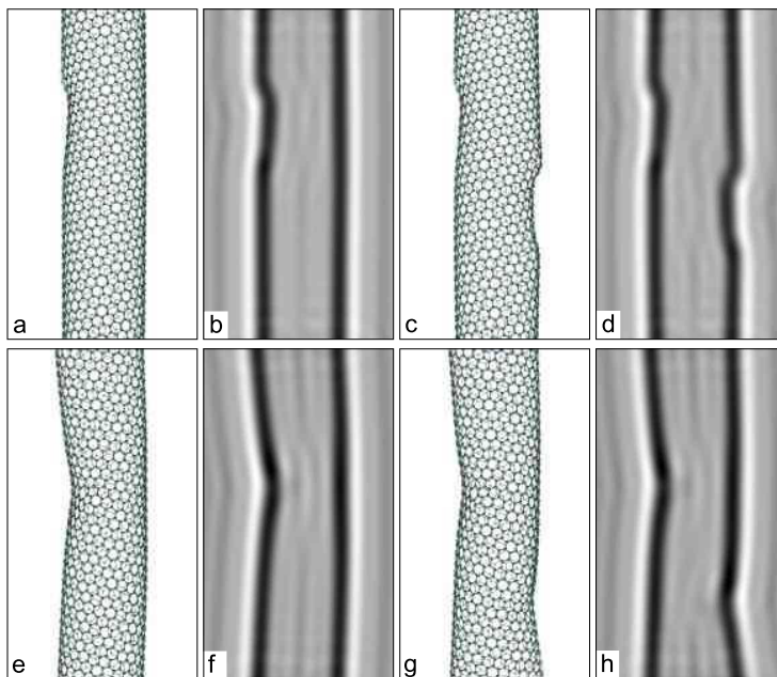


Figure 2.14: **Line defects in CNTs.** (a-h) relaxed structures and the corresponding simulated HRTEM bright field images of different dislocation lines in a (20,5) CNT with 12 missing atoms. Reprinted figure with permission from [54] Copyright (2008) by the American Physical Society.

The knock-on cross section proposed by [53, 54] for an acceleration voltage of 60 keV is vanishing. One needs to focus on the properties of the studied system that could lower the threshold energies and hence enable knock-on damage.

The first thing that plays a role is the enhanced curvature at the sidewalls (compare Fig. 2.13) of the CNT, as it is known that smaller diameter CNTs have softer bonds due to the enhanced

curvature [56, 55]. The threshold energy of CNTs above 2 nm is expected to be similar to that of graphene. The diameter dependence starts to be stronger when approaching diameters smaller than 1 nm [57]. In the studied case CNTs that approach 1 nm in diameter are not affected by this flattening mechanism. Therefore, curvature alone does not significantly lower the threshold energies in order to lead to knock-on damage.

Secondly, going beyond the static approximation of the targeted lattice one can include atomic vibrations in terms of phonon modes. This total cross section was calculated by [52]. In the picture of quantum description of vibration of atoms in a crystalline structure the velocities follow a temperature-dependent distribution that depends on the material-specific phonon modes. In the case of 2D-materials in a usual TEM-geometry the out-of-plane velocities  $v_z$  of the nuclei are of the biggest interest. To estimate the phonon DOS a DFT-calculation of the phonon band structure of graphene is performed. Considering the out-of-plane acoustic (ZA) and the optical (ZO) phonon modes of graphene this yields in a mean square velocity in  $z$ -direction  $\overline{v_z^2} \approx 3.17 \times 10^5 \text{ m}^2/\text{s}^2$ . Assuming a Gaussian distribution of the out-of-plane velocities  $P(v_z, T)$  the total cross section is given by [58]

$$\sigma(T, eV_0) = \int_{E_{max}(v_z, eV_0) \geq T_d} P(v, T) \sigma(E_{max}(v_z, eV_0)) dv. \quad (2.20)$$

The energy transferred to the nucleus after the scattering event, when the movement in  $z$ -direction parallel to the incident beam is considered, gives [58]

$$E_n(eV_0, v_z) = \frac{(2\sqrt{eV_0(eV_0 + 2mc^2)} + Mv_z c)^2}{2Mc^2}. \quad (2.21)$$

Respecting the most favorable thermal velocity of the carbon atoms, this is three standard deviations in the Gaussian distribution of the thermal velocities, the maximum transferred energy is enhanced to 14.6 eV. Compared to the the lowest observed threshold energies of 18 eV [5] in experiments, that still gives a vanishing cross section for this process. The threshold energy for a monovacancy is of 14 eV [55], this implies that maximum transferred energy is higher than the actual threshold leading to non-zero cross section. For the case of a divacancy the cross section is vanishing again.

These calculations in this model are done for flat graphene. It is noteworthy that the case of graphene and the vertical phonons, parallel to the electron beam, can be considered as a boundary case for the one of the CNTs used in this scattering geometry. The damage mostly happens at the side and the vertical component of the out-of-plane phonon will never reach the value of the case of graphene. Therefore, one can exclude that atoms cannot be removed from the lattice by elastic scattering, but the scattering events can still move atoms and transfer energy.

### 2.5.3 Chemical etching in STEM

As knock-on damage is only possible at already damaged graphene and excitation and ionization do not play a role in this experiment, the attention will now be put to chemical etching processes. These come into play when residual molecules in the vacuum are split under the electron beam and react with the sample.

At the beginning a short overview of the theoretical description of chemical etching will be given. Most commonly, etching is modeled by considering the absorption of gas molecules, desorption, dissociation and surface diffusion. Neglecting diffusion and assuming that the etching product leaves the surface immediately after the dissociation the etching rate can be expressed by

$$R_E \propto \frac{xP_D\Phi_e s\Phi}{s\Phi + p/\tau + P_D\Phi_e}, \quad (2.22)$$

where  $x$  is at stoichiometric factor indicating how many atoms are removed by one radical,  $P_D$  is the probability to dissociate an atom,  $\Phi_e$  is the flux of electrons,  $s$  is the sticking coefficient stating the probability for a molecule to stick to the surface,  $p$  density of absorption sites and  $\tau = \tau_0 \exp(\frac{E_A}{k_B T})$  ( $E_A$ , the absorption energy) the mean residence time for the etching species [35].

Chemical etching has been observed by [11] at vacuum level in the  $10^6 - 10^{-7}$  mbar range. The process starts at a contamination site that presumably contains a defect. The increase of the perimeter of the hole as a function of the electron dose at 20 keV and 80 keV is analyzed. The fact that the process doesn't primarily depend on the electron energy suggests that it has a dependence on the local atmosphere of the surrounding vacuum.

In a recent study [2] nanopores were formed by an electron voltage 100 keV in STEM for an irradiation time of about 1 min. The imaging is performed at 60 keV and oxygen is leaked into the microscopy column. The rate of chemical etching corresponds to the growth of the nanopore. The pore growth plotted against the cumulative electron dose shows a linear behavior. This implies that the growth is limited by the amount of oxygen atoms and not the reactive sites. If the last one was the case, the etching rate would depend on the diameter of the nanopore. The etching rate between near-UHV ( $10^{-10}$  mbar) and  $2 \times 10^{-7}$  mbar differs by two orders of magnitude. For example at  $2 \times 10^{-7}$  mbar the etching rate is 4 atoms/s [35]. It is shown in case of single layer graphene that at pressures typical for EM instruments chemical modification yielding from non-ideal vacuum have a sustainable impact on the structure of the sample [2]. Controlled air leakage into the microscope column is shown to be effective in cleaning hydrocarbon contamination, but

is not damaging the pristine graphene lattice. Oxygen and water atmospheres between  $10^{-10}$  –  $10^{-6}$  mbar show a similar behavior like air. Oxygen shows etching rates about twice as efficient as water. The pristine graphene is not touched even in oxygen environment, the graphene edges are prone to damage [1]. Armchair edges are more resistant to knock-on damage than zigzag, but they are more easily destabilized under oxygen atmospheres [2]. Also defects in graphene can serve as reactive sites for chemical etching of the oxygen [1]. When considering the etching rates yielding from the model given in eq. (2.22) at a reasonable beam current of 50 pA per  $1 \text{ nm}^2$ , this gives only an etching rate of  $2 \times 10^{-22}/\text{s}$ , in clear discrepancy with the experimental observed rates. An attempt was made to adjust the model by taking into account ionization or dissociation of the oxygen molecules by the electron beam [35]. The total number of landing molecules on the clean area of interest on the sample is

$$N_x = \sigma \rho d, \quad (2.23)$$

where  $\sigma$  is the cross section for ionization or dissociation,  $\rho$  the gas density and  $d$  the diameter of clean area on the sample surface. When considering an ionization cross section of  $3 \times 10^6 \text{ b}$ ,  $p = 1 \times 10^{-6}$  mbar,  $d = 10 \text{ nm}$  at 300 K and an electron current of 40 pA this gives an etching rate of  $1.8 \times 10^{-5}/\text{s}$ . The rate when considering dissociation is expected to be even smaller. That is still orders of magnitudes away from the experimentally observed rates.

Large quantities of contamination on top of CNTs can make them weaker under electron irradiation. Aberration-corrected low voltage high resolution (LV-HR) TEM (vacuum level in  $10^{-7}$  Torr range) operated at 80 keV is used and time frames are taken every 5 s. Clear damage and eventual destruction of CNTs can be observed (Fig. 2.15)(a-j) [56]. It is notable that only the contaminated CNT is destroyed under electron radiation.

Summing up one can state that chemical etching of carbon nanomaterials is observed with oxygen and the oxygen contained in water at reactive sites under the electron beam in the STEM.

## 2.6 Chemistry of graphitic carbon networks

### 2.6.1 Chemical reactivity of graphene and CNTs

Theoretical studies [59, 60] have shown that defects increase the chemical reactivity of graphene. Point surface defects play an essential part in the carboxylation of graphene. The reactivity of

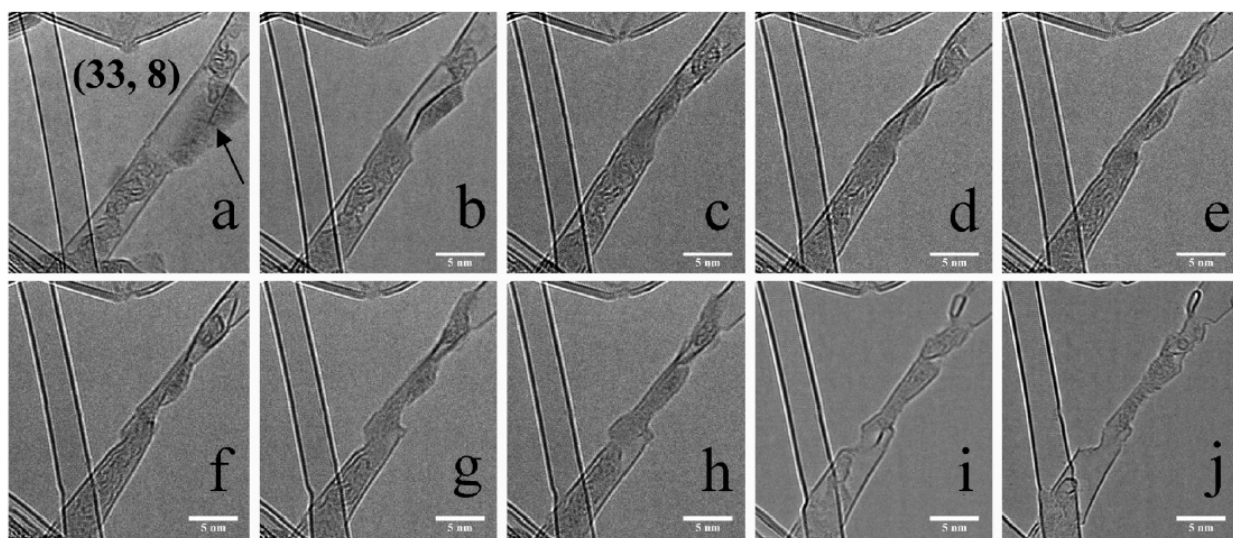


Figure 2.15: **Damaging of contaminated CNTs.** (a-j) HRTEM time series of every 5 s at 80 keV of several CNTs are given. The contaminated CNT shows clear damaging. Adapted with permission from [56]. Copyright (2009) American Chemical Society.

single vacancies, (555-777) and (585) double vacancies, Stone Wales defects, hydrogenated zigzag and armchair edges is analyzed by dispersion-corrected density functional theory. The numbers 5,7 and 8 correspond to penta-, hepta- and octagon, respectively. The chemical reactivity depends on the type of functional group added. H, F and phenyl groups ( $C_6O_5$ ) were analyzed. The reactivity for the respective most reactive bonding site ranks in the following starting from the most reactive: single vacancy, zigzag edge, 585, 555-777, Stone Wales, armchair edge, pristine graphene. In the case of single and double vacancies fluorine is the most reactive followed by hydrogen and phenyl groups. Further, the cooperative addition of two radicalized aryl groups ( $C_6O_6$ ) was considered. The double vacancies and the Stone Wales defect show a similar behavior. The second aryl group is bond to a nearby carbon atom of the first group on the opposite site of the lattice. The chemical reactivity of the defect is enhanced. In the case of the Stone Wales it is even nearly doubled. The single vacancy does not show an increase in chemical reactivity when adding a second group [61].

In the case of CNTs the strain-induced changes in the local bonding of a curved CNT have to be taken into account. In Fig. 2.16(a)(b) two CNTs with different diameters are presented. Two angles can be determined depending on the chirality that have an impact on the properties of the obtained material with respect to pristine graphene. Firstly, the pyramidalization angle  $\theta_p$  calculated by comparing the angles of the  $\sigma$ - and the  $\pi$ -orbitals (Fig. 2.16.c(i),(ii), Fig. 2.16.d(i),(ii)). Secondly,  $\phi$  is the misalignment angle between two adjacent  $\pi$ -orbitals (Fig. 2.16.c(iii),(iv), Fig.

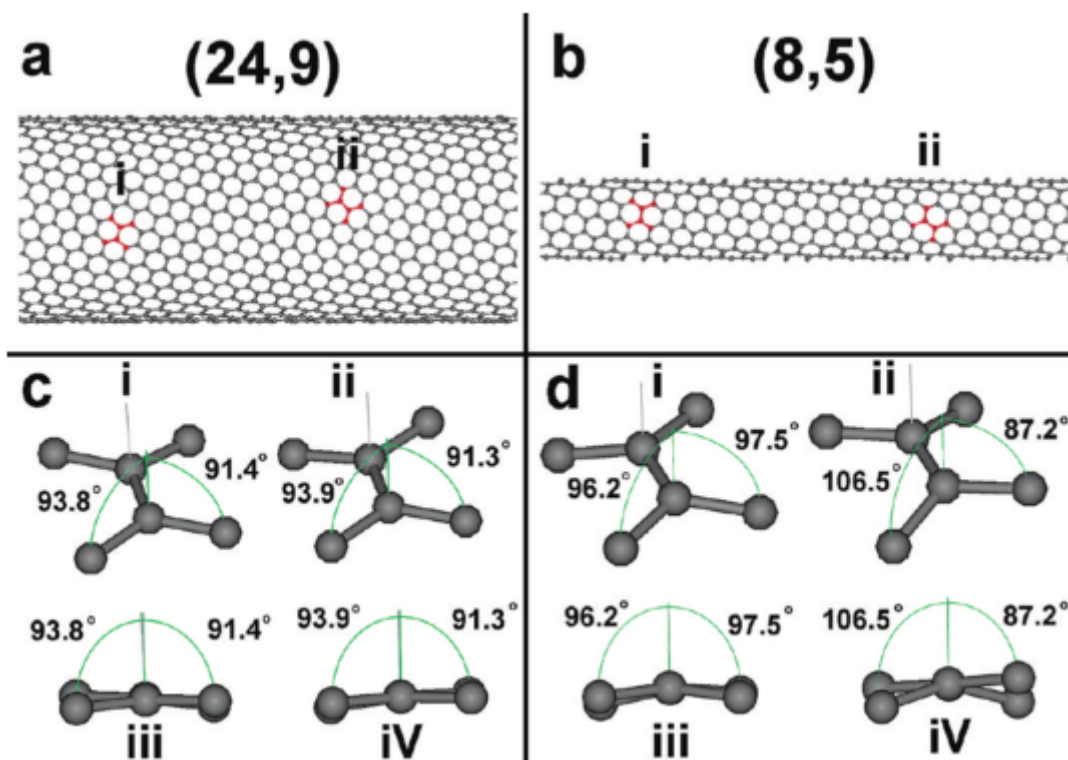


Figure 2.16: **Pyramidization and  $\pi$ -orbital misalignment angle.** (a) the atomic structure of a (24,9). (b) a (8,5) CNT and selected areas in red. (i) and (ii) the angles necessary to calculate the pyramidization angle  $\theta_p$ . (iii) and (iv) for  $\phi$ , the  $\pi$ -orbital misalignment angle. Reprinted with permission from [56]. Copyright (2009) American Chemical Society.

2.16.d(iii),(iv)). In  $sp^2$ -hybridized carbon  $\theta_p$  is zero and for  $sp^3$ -hybridized carbon it is  $19.5^\circ$ . In CNTs the  $\theta_p$  represents a measure of chemical reactivity, whereas  $\phi$  stands for the strain in the graphitic network. To give some examples, a (5,5) CNT, diameter of 0.676 nm, has a  $\theta_p$  of  $5.97^\circ$  and a  $\phi$  of  $21.3^\circ$ . A (10,0) CNTs, diameter of 0.781 nm, has a  $\theta_p$  of  $5.15^\circ$  and a  $\phi$  of  $18.5^\circ$ . A (10,10) CNT, diameter of 1.35 nm, has a  $\theta_p$  of  $3.00^\circ$  and a  $\phi$  of  $10.4^\circ$ . Both angles scale inversely with the tube diameter.  $\theta_p$  and hence the chemical reactivity starts to change rapidly when approaching diameters smaller than about 1 nm [62].

In CNTs it has been shown also experimentally [63] that the chemical reactivity to  $O_2$  highly depends on their diameter, metallicity and their chiral angle. The CNT samples undergo an oxidation treatment with air under different temperatures ( $400$ - $490^\circ C$ ), as conferred via TEM before and after the treatment. The reactivity is determined by an interplay of chiral angle and diameter. Smaller diameter CNTs are more reactive as CNTs with small chiral angles. Metallic CNTs have a greater intrinsic chemical reactivity than semiconducting ones. This applies only for small diameters. For example for a (19,10) CNT, diameter of 1.45 nm is even more stable than

a comparable semiconducting one. First principle DFT calculations provide theoretical insights. The  $O_2$  needs to overcome a barrier of about 1 eV to get absorbed into the carbon lattice. Then the oxygen splits into two oxygen adatoms. The first defect is formed by the evolution of a  $CO_2$  molecule. Then the process becomes exothermic. The focus in the simulations was put on the dependence on the chirality and CNTs with roughly the same diameter were analyzed, as the increase of reactivity with decreasing diameter is assumed. The experimental evidence that higher chiral angle are more stable could be reproduced [63].

## 2.6.2 Hydroxyl groups on graphene

Chemical etching processes involving oxygen need an imperfection of the graphene lattice. Assuming that the CNTs have only few pre-existing defects, it is still not clear what could cause the first defect that acts as a nucleation site for the damaging process. There must be other elements or groups of elements responsible.

The adsorption energy for a hydroxyl groups, where covalent bonds are formed between carbon, oxygen and hydrogen, on graphene yields  $-9.34$  eV with respect to free atoms. The epoxide group, where the oxygen forms two covalent bonds with two neighbouring carbon atoms, is only  $-4.72$  eV. Bonding of an OH-molecule can introduce significant local distortion to the lattice. The oxygen is on top of the carbon atom nearly perpendicular to the lattice plane. The bound carbon atom moves up by  $0.37$  Å. The C-bond of the nearest neighbors is of  $1.48$  Å. The O-H-bond is  $0.98$  Å, a small amount longer than in water. The hybridisation of the carbon changes from  $sp^2$  to distorted  $sp^3$ . The adsorption of an OH-molecule influences significantly the surface electronic charge density. When considering one OH-group, a flat band at Fermi-level is introduced and there is a small band gap between this OH-band and the upper bands. The reason for the opening of the band gap is firstly due to the symmetry break of the sublattice and secondly because of the strong  $sp^3$ -hybridization. The peak in the DOS corresponds to the  $2s$  orbital from oxygen in the OH-group [64].

In the next step a closer look to the bonding geometry will be put, as well as the role of the aggregation of more OH-groups adsorbed at the same time will be discussed. The orientation of the O-H bond has also an effect on the stability and the H atom pointing to the center of the hexagon is energetically favoured. The OH-bond can rotate at room temperature. Co-adsorption of two OH-groups at the same 6-fold ring is calculated. The energetically most favorable adsorption sites are when O-H groups are found on two neighbouring atoms on the opposite side of

graphene. This gives a binding energy of  $-2.92$  eV. The binding energy of a single OH-molecule can be significantly enhanced when more groups are absorbed at the same time. For comparison, the binding energy of a single O-H molecule is of  $-0.78$  eV. In the case of one and three hydroxyl groups there is a distinguishable peak at Fermi-level in the density of states. For more hydroxyl groups the arrangement has a direct impact on the electronic structure. The band gap increases with the growing number of oxygen-containing groups on the surface [65].

There are no studies on the literature that cover in detail the bonding of OH-groups on CNTs. But what can be stated is that CNTs are more reactive than graphene. The pyramidalization angle, a measure for the chemical reactivity,  $\theta_p$  is about  $3^\circ$  in most CNTs used in this study compared to zero angle in flat graphene. The bond between the OH-molecule and the carbon atom of the CNT is expected to be stronger and more stable under electron irradiation in STEM.

After the impact on the structural and electronic properties of OH-group bonding were worked out, in the following the role of OH-molecules on the graphene surface under electron radiation in TEM is discussed.

### 2.6.3 OH-groups forming point defects in graphene in TEM

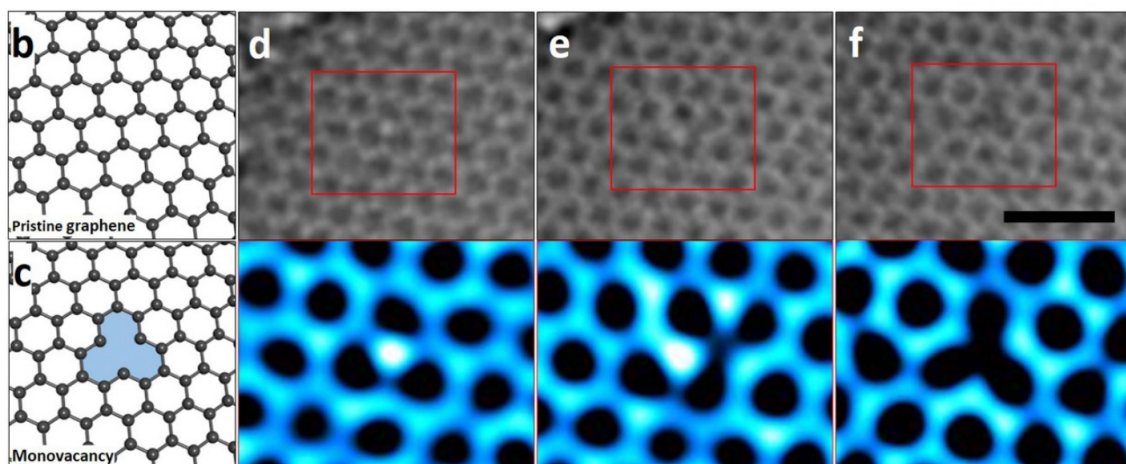


Figure 2.17: **Monovacancy in graphene.** (b), (c) schematic depiction of the pristine graphene lattice and a monovacancy. (d-f) atomic resolved ARTEM images with enlargement (red box). Adapted with permission of IOP Publishing, from [12] 2020; permission conveyed through Copyright Clearance Center, Inc.

In the TEM during electron radiation, the position of ejection of a carbon atom is generally random, although in this experiment point defects are formed at the site in the graphene lattice

where OH-molecules are bound. From previous studies it is known that OH-groups are more preferentially absorbed than oxygen. The pristine graphene lattice was imaged in atomic resolution (AR) TEM, then the sample was treated by ultraviolet ozone (UVO) [12]. In UVO treatments the sample is put into a vacuum chamber, oxygen is introduced under UV irradiation [66]. It is used mainly in semiconductor devices to control critical interfaces [67].

Under the electron beam defects were formed. From DFT calculations it is shown that the formation of monovacancies is unpreferable involving only oxygen. Not considering hydrogen, the structure is not stable enough. There are three types of point defects observed in their experiments [12]. The first one is a monovacancy. The formation is shown in consecutively taken TEM images (Fig. 2.17(d-f)). In Fig. 2.17(b)(c) the atomic structure of pristine graphene and the monovacancy can be observed, respectively.

The issue with the HRTEM images shown in Fig. 2.17(d-f) is that there is no principle way with this experimental technique to argue that it is really an OH-group. The images look very similar to HRTEM images discussing nitrogen impurities [57]. In that case the nitrogen gets pyridinic and the threshold energy of the adjacent carbon atom gets drastically lower and defects can be easily formed at 80 keV.

In Fig. 2.18(a-g) the formation route from the DFT calculation is shown. The blue numbers indicate the energy barriers in eV, whereas the gray bars are the formation energies for each step. The OH-molecule forms a bridge between two neighboring atoms. The OH-molecule forms a single bond to an adjacent carbon atom. Then the OH-group splits up into oxygen and hydrogen. In the graphene lattice that contains both the hydrogen and oxygen molecules the carbon bond is broken with an energy barrier of 5.19 eV and the detachment of the C-O atoms from the lattice needs to overcome a barrier of 6.03 eV. Eventually the C-O molecule is desorbed from the lattice [12].

These energy barriers are not exceeded at thermal activation at room temperature. Energy must be provided by the electron beam in the TEM. They do not discuss the fact that process of adatom removal by scattering is much more probable. Further it is not clear how the energy is transferred from the electrons to the sample.

The second pathway to a point defect based on the experimental observation and consequential DFT-calculations involve a Stone-Wales defect. Starting point is the bridging of the O-H molecule with two carbon atoms. The hexagon containing the O-H is transformed into a Stone-Wales

defect (55-77) with a rotational barrier of 6.78 eV. The O-H atoms are dissociated. Two carbon bonds are broken (5.73 eV) and the C-O atom is detached from the graphene lattice overcoming a barrier of 6.76 eV. The formed defect is transformed into a monovacancy by another 90° bond rotation [12].

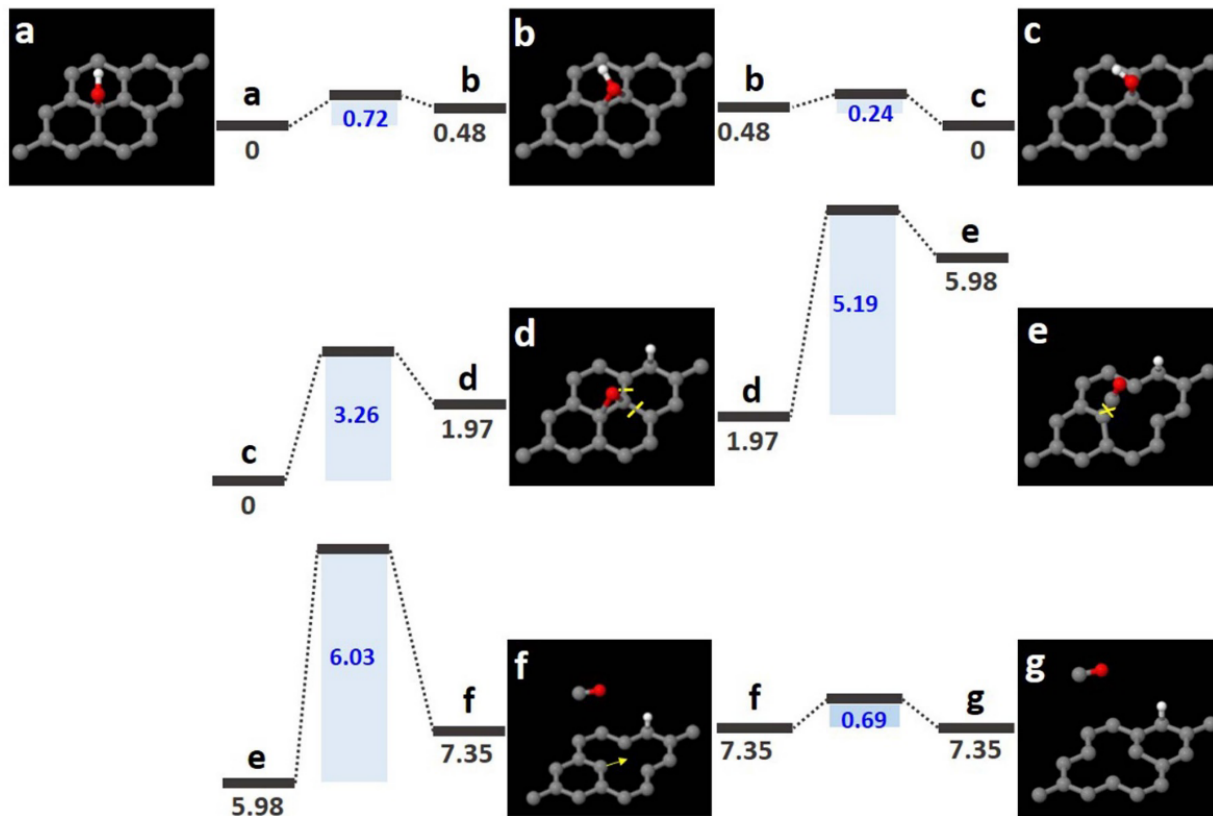


Figure 2.18: **Defect formation route.** (a) the OH-molecule bridging on two atoms. (b-g) the intermediate steps of the monovacancy formation. Used with permission of IOP Publishing, from [12] 2020; permission conveyed through Copyright Clearance Center, Inc.

The second type of defect discussed by [12] is a divacancy starting from a monovacancy and it is argued that hydrogen needs to be present. They do not give an explicit reason. This is clearly in opposition to the experimental STEM results of [1]. In that study it is shown that defects show damaging via chemical etching when pure oxygen is leaked in the microscope column. Assuming that water is split into O-H groups under the electron beam this matched the discussed case by [12]. The etching rates that are observed in STEM are about twice as high in the case of pure oxygen compared to the case of water [1]. So, it is true that O-H groups show similar damaging behavior like oxygen in EM, but the presence of hydrogen is not a condition.

The third type of defect they observe is a pair of 13-5 ring. It is stable for a few seconds. This structure if it consists only of carbon atom is not stable, as the atoms would move to the ad-

jaent site. The involvement of hydrogen makes it stable. DFT calculations suggest that in the detachment process of the C-O atoms a second hydrogen atom is involved in order to explain the observed structure [12]. Light elements like hydrogen would be removed very quickly by electron scattering.

# Chapter 3

## Experiment, Results and Discussion

In the following chapter the experimental approach will be described in detail. The results of the whole experiments leading to this thesis are given. A discussion and interpretation of the results will be done in step by step. Final conclusions will be drawn in the following chapter (ch. 4).

### 3.1 Analysis of STEM images

Before doing any measurements from the STEM images, they need to be calibrated. This is done by searching a spot with atomically clean graphene in the STEM image. Then a Gaussian blur filter is applied to the image. The distance in pixels of four consecutive hexagons of the graphene lattice is measured in zigzag direction. For that a line plot profile is done and the distance between the maxima is measured by hand. The accepted value for the interatomic distance in graphene is given by  $b = 1.42 \text{ \AA}$ , therefore the distance in zigzag direction in the hexagonal lattice gives  $\sqrt{3}b = 2.46 \text{ \AA}$ . So, the distance for four hexagons is equal to  $9.84 \text{ \AA}$ . By dividing this known distance and the distance measured in pixels, one can get the distance in  $\text{\AA}$  of one pixel. Knowing this the image can be calibrated. The calibration is done once for every microscopy session. The uncertainty of this calibration is estimated by the statistical standard deviation of 5 independent measurements. This gives an relative uncertainty of about 3%.

The analysis of the chirality pair  $(m, n)$  involves the determination of the interlayer distances and approximated Bessel fitting along the equatorial line in the diffraction pattern [43]. In Fig. 3.1(b) the fast Fourier transform (FFT) of the STEM image in Fig. 3.1(a) is shown. The hexagonal maxima of the graphene in the diffraction can be observed, as well as some contribution of the

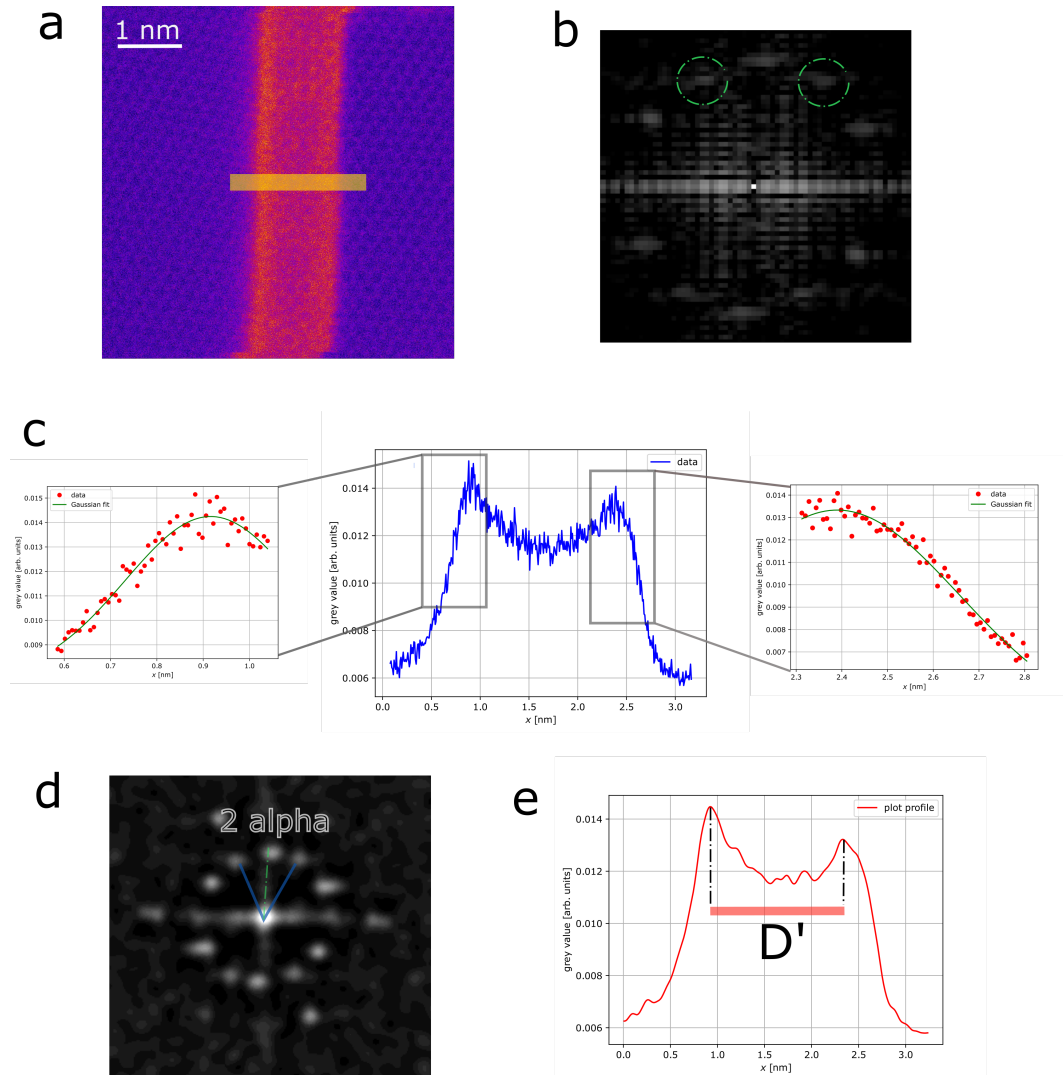


Figure 3.1: **Analysis of STEM images.** (a) shows a STEM image (FOV of 8 nm,  $1024 \times 1024$  pixels and  $16 \mu\text{s}$ ) of a CNT suspended on graphene. (b) a FFT of the image of a). (c) a plot profile along the yellow line in a) and the two zoom-ins show the results of the Gaussian fits to determine the maxima. (d) a processed FFT of the image of a). (e) the plot profile of the yellow line of a) after the application of a Gaussian blur filter,  $D'$  refers to the enlarged diameter due to VdW-flattening of the CNTs.

CNT (green circles). It is neither possible to individuate the interlayer spacing pairs, nor the approximated fitting of the plot profile gives reasonable results. This is mainly due to the limited resolution of the FFT and hence the limited amount of data points in the plot profile. Another complication is the flattening of the CNTs, as shown by [8], and its impact on the diffraction pattern is highly non-trivial. Therefore, the focus of the analysis of the STEM images will be put on the determination of the diameter and the chiral angle.

In a first attempt the diameter is determined by a plot profile perpendicular to the CNT axis (Fig. 3.1(c)). The distance between the maxima in the intensity profiles gives the CNT's diameter. The maxima are found by fitting a Gaussian to the values of the plot profile. The statistical deviation in the fits gives an uncertainty of  $0.3 \text{ \AA}$ . Results within this uncertainty can be obtained by applying a Gaussian blur filter to the STEM image and doing then the plot profile, as shown in Fig. 3.1(e). The distance of the maxima is measured by hand and by simply guessing the position of the maxima. This procedure is adapted, as it is much less time consuming. There is another complication when determining the CNT diameter. In the STEM image we only access the projection of the "flattened" diameter, denoted with  $D'$ . The only way to find out about the actual diameter is to have a part of the same CNT, both on graphene and vacuum suspended. Experimentally, that is rarely the case. To deal with that problem, to the data from [8] comparing  $D$  and  $D'$  a second order polynomial is fitted. The coefficients from the fitting yield  $a_0 = -(2.9 \pm 0.6) \times 10^{-2} \text{ nm}$ ,  $a_1 = (1.1 \pm 0.1)$  and  $a_2 = -(5.7 \pm 0.5) \times 10^{-2} \text{ nm}^{-1}$ . An expression that converts the experimental accessible diameter into the pristine diameter can be determined. This enables to simply measure the plot profile of a CNT suspended on graphene on an arbitrary position and to be able to determine the actual diameter.

For the determination of the chiral angle, the FFT of the STEM images need to be processed. The resolution of the pristine image is not good enough to allow that. The aim is to extract only the necessary information of the FFT. This is done by bilinearly scaling the image to  $2048 \times 2048$  pixels. A rectangle around the CNT is selected to minimize the graphene background. The dimension of that depends on the diameter and the relative orientation of the CNT in the image. A FFT of the rectangular selection is provided. The FFT image is duplicated and to one of those a Gaussian blur filter is applied. One image is subtracted from the other to get rid of the high frequency components. To the resulting image another Gaussian blur filter is applied and the chiral angle can be measured, as shown in Fig. 3.1(d). The uncertainty of the measurement of the chiral angle was estimated by the statistical deviation of five measurements. This gives an relative error of about 2%. The analysis of the diameter, the corresponding plot profiles, the image processing, as

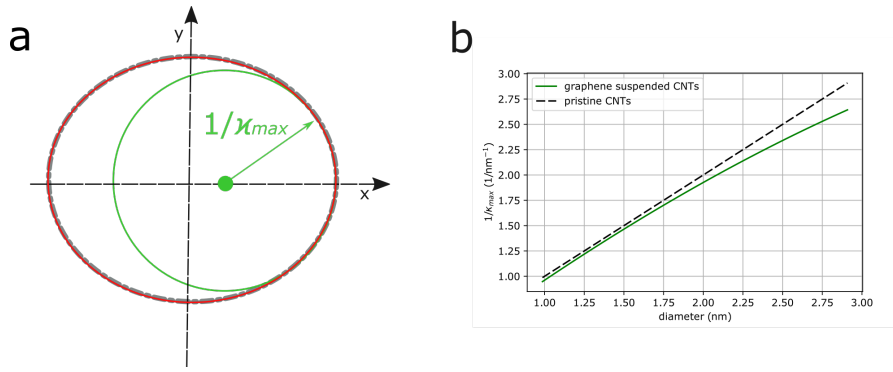


Figure 3.2: **Curvature fitting of flattened CNTs.** (a) the pristine CNT (green) fitted to the ellipse of the flattened CNT (red). (b) a plot of the maximum curvature at the sidewall from the fit against the CNT diameter.

well as the measurement of the chiral angle are performed with ImageJ software.

The interesting part for the experiment is the sidewalls of the CNT, this is where mainly the damage happens. For that purpose an ellipse is fitted to cross section of the flattened CNT, as shown in Fig. 3.2(a). This is done by knowing the semi-major axis  $a$  of the ellipse, it corresponds to  $D'/2$ , and the circumference is assumed to be constant throughout the flattening process. This is a valid assumption, as the change in bond length even in an (5, 5), diameter of 0.68 nm, doesn't exceed 0.6% [68]. Mathematically speaking one needs to analyse the curvature  $\kappa$  of a plane parametrized curve. Considering an ellipse, with the following parametrization  $\gamma(t) = (a \cos t, b \sin t)$ , this yields

$$\kappa(t) = \frac{|ab|}{(a^2 \sin^2 t + b^2 \cos^2 t)^{3/2}}. \quad (3.1)$$

In the case of the edges at the sides this corresponds to  $t = 0, \pi$  and therefore gives a curvature  $\kappa_{max} = a/b^2$ . The inverse curvature corresponds to the radius of a pristine CNT (Fig. 3.2(a) green circle). In Fig. 3.2(b) the diameter of the CNT is plotted against the fitted diameter corresponding to the maximum inverse curvature. It can be observed that with growing diameter the curvature at the sidewall increases and accordingly the fitted diameter decreases. In the case of a diameter  $D = 2.5$  nm the fitted diameter is reduced by 7%.

## 3.2 Electron dose analysis of the damage at UHV

The electron dose is not observable directly in the microscope. What can be measured is the VOA current. This is related to the electron current as follows,  $I_{e^-} = k_{VOA} \cdot I_{VOA}$ . The dose rate of the electron is given by  $D_{e^-,rate} = I_{e^-} / e$ , where  $e$  is the elementary charge. Finally, the electron dose

is calculated by  $D_e = D_{e-,rate} \cdot \Delta t$ , where  $\Delta t$  is determined by the dwell time, of every individual scattering event, times the amount of pixels. In this experiment it is sufficient to simply consider the sum of the dwell times. In reality, the beam parks before every scan row to stabilize. During this process, it is dosing the sample. As only parts in the center of the FOV are considered this has no implication on the electron dose. The electron doses of every single frame until the first apparent damage to the tube wall can be observed are summed up. In the frame, where the damage happens only the portion until the damage is taken into account. As the damage is limited to the CNTs, only the fraction of the frame that contains the CNT and  $0.5 \text{ \AA}$  added on both sides are considered. Assuming a 1.4 nm CNT in a STEM image (FOV of 12 nm,  $1024 \times 1024$  pixels and  $16 \mu\text{s}$  dwell time) this gives a dose of about  $5 \times 10^8$  electrons per frame. A statistical analysis of the electron doses is performed. For that twice the value of electron doses with respect to the maximal electron dose yielding form the electron analysis is considered. An iteration over the values of electron doses, from 0 to twice the maximal value, is done. In each iteration those cases are summed that have a bigger or equal electron dose than the considered electron dose. The aim of this analysis is to determine whether the damaging process is Poisson-distributed.

The uncertainties that play a role in this analysis are the determination of the CNT diameter and the image calibration. These are in the order of 3%. The calibration of the VOA current plays a role. Three different values depending on the date of the data recorded are considered. They vary by about 12%. Lastly the fact that in cases where the damage occurs right in the first recorded frame, the exact electron dose leading to a damage remains obscure and can only be roughly estimated. The spot where the irradiation experiment is performed is dosed when the scan is set up. This value is assumed to be constant in all cases and considering the accuracy of this measurements this has no impact.

### **3.3 Damaging of CNTs under UHV**

#### **3.3.1 Sample no.189, 190 and 195**

The first five STEM experiments were spent with samples no.189, 190 and 195, one experiment for no.189 and 190, whereas three experiments with no.195. The first two samples are Si-N grid samples and no. 195 is a Graphenea gold grid with standard CVD-grown graphene. The graphene is "Easy transfer" graphene in the case on Si-N grids, a detailed description of the transfer method

is given in sec. 2.2.2. The CNTs are deposited in a FC-CVD reactor with TP-collection, for details see sec. 2.2.6. The CNTs face the electron beam. The window in the silicon support frame of the Si-N grids is searched. In the case of the gold grids, the windows that contain the amorphous carbon film ("Quantifoil") are searched. The holes in the Si-N film or in the Quantifoil are searched in CCD-mode. The sample location is uniquely recognized by following the outmost rows of holes in the case of SiN grids. In the gold grids the central marker is searched. In this mode of the microscope possible irradiation positions are identified. The whole sample is globally scanned at large defocus of about  $-100\,000$  nm. If CNTs become visible, the defocus is decreased. The irradiation spot must contain individual CNT suspended on graphene, both atomically clean. The microscope stage can be driven to the same position again afterwards in scan mode for ADF imaging. The biggest struggle in CCD-mode is to distinguish between individual CNTs and grain boundaries. Spots with atomically clean graphene and clean CNTs are very rarely found. The microscope is operated at 60 keV acceleration voltage. The tuning is done in CCD-mode of the STEM and then in scan-mode the astigmatism is corrected manually reaching atomic resolution, as described in detail in sec. 2.3.3. These first experiments didn't give any relevant data. The biggest struggle is the CNT concentration and the contamination, both inherent to the CNT synthesis and deposition. In samples no.189 and 190 there was definitely too high CNT concentration, whereas 195 showed almost no CNTs at all. The problem with too high concentration is that the CNTs start to bundle and also an excess of contamination is brought to the sample. In this case it is not possible to find individual CNTs that are atomically clean. The deposition time and the yield of the reactor are the key ingredients. But as there are big fluctuations in the FC-CVD synthesis the low yield CNT deposition can only be partly controlled. The ideal sample is the sweet spot between low concentration and just enough CNTs to find enough possible sample spots. Only in the third experiment with sample no.195, one bundle with a lot of contamination was found. A laser cleaning procedure was applied to get rid of an excess of contamination. The first laser cleaning set-up was used, as described in sec. 2.3.5. The main issue in the used cleaning set-up is that the laser does not hit the sample at the position of the electron beam. Based on some preliminary studies with higher laser powers the offset of the alignment is known. Before using, the laser needs to be armed and can then be controlled inside a window of the microscope's software. First laser settings were 1 kHz at 50% for 10 ms. No visible changes can be observed. Then at 100%, the exposure times were increased to 50 ms by 10 ms steps. Still no visible effect can be observed. Finally with 100 ms exposure the sample got cleaner, but the amorphous carbon film got a lot thinner and at some points cracked. This procedure leads to clean graphene, but the CNTs attract a lot of hydrocarbon contamination.

### 3.3.2 Sample no.192

Sample no.192 is used for the next three experiments. It is a Si-N TEM-grid with graphene-suspended CNTs. The graphene is "Easy transfer" graphene, a detailed description of the transfer method is given in sec. 2.2.2. The CNTs are deposited in a FC-CVD reactor with TP-deposition, for details see 2.2.6. The CNTs face the electron beam. In the first experiment hundreds of holes were scanned globally at roughly  $-100\ 000$  nm defocus, but only one CNT could be found. Another attempt to laser clean was performed. The first laser cleaning set-up was used, as described in sec. 2.3.5. The laser settings were 1 kHz at 3% for 20 ms. A little improvement in terms of cleanness of the sample can be observed. But again, the CNTs seem to contaminate even more, as in the previous case. The second experiment was the first one that allowed to gather useful data sets. The sample position had the right CNT concentration and met the requests of this study. The experimental approach in terms of microscope tuning and finding sample spots for the irradiation was the same as just described at the beginning of sec. 3.3 and the microscope was operated at 60 keV. Sample spots 1 and 3 are found. These are cases where CNTs are buried under thick hydrocarbon contamination. Those positions are imaged, as there is indication in the literature that thick contamination can make CNTs softer under electron radiation [56]. An overview of these two CNTs is given in Fig. 3.3(c) (FOV 192 nm,  $1024 \times 1024$  pixels and  $4\ \mu\text{s}$  dwell time). The dwell time refers to the time that the electron beam spends on every pixel. It is notable that during the irradiation in all three cases more hydrocarbon contamination is built up, as one can observe in Fig. 3.3(a)(b). The thick contamination leading to a significant background in the FFT makes it impossible to analyze the diameter and the chiral angle. Both cases are stable under electron irradiation for 21 and 24 frames respectively, frames were taken at FOV of 12 nm  $1024 \times 1024$  pixels and  $16\ \mu\text{s}$  dwell time. Sample spots 4, 5, 6 and 8 are also imaged in this experiment. These spots show atomically clean graphene and CNT that are suspended on top. In all cases image series are recorded. All of these sample spots show appearance of mobile hydrocarbon contamination and the eventual destruction of the CNT. This can be stated as the sidewall of the CNT is disintegrated. A few images of the taken image series of sample spot 5 are given in Fig. 3.4(a-d), the numbers refer to the frame number of the series. The images were recorded at FOV of 12 nm,  $1024 \times 1024$  pixels and  $16\ \mu\text{s}$  dwell time. Fig. 3.4(e) shows a FFT of the green rectangle in (d). The sharp diffraction maxima of the graphene background in the characteristic hexagonal form can still be seen. Spots 4 and 7 show mobile contamination on the second frame (FOV of about 6 nm,  $1024 \times 1024$  pixels and  $16\ \mu\text{s}$  dwell time). Spots 5, 6 and 7 instead on the first frame at FOV of about 12 nm,  $1024 \times 1024$  pixels and  $16\ \mu\text{s}$  dwell time. With the chosen microscope settings the

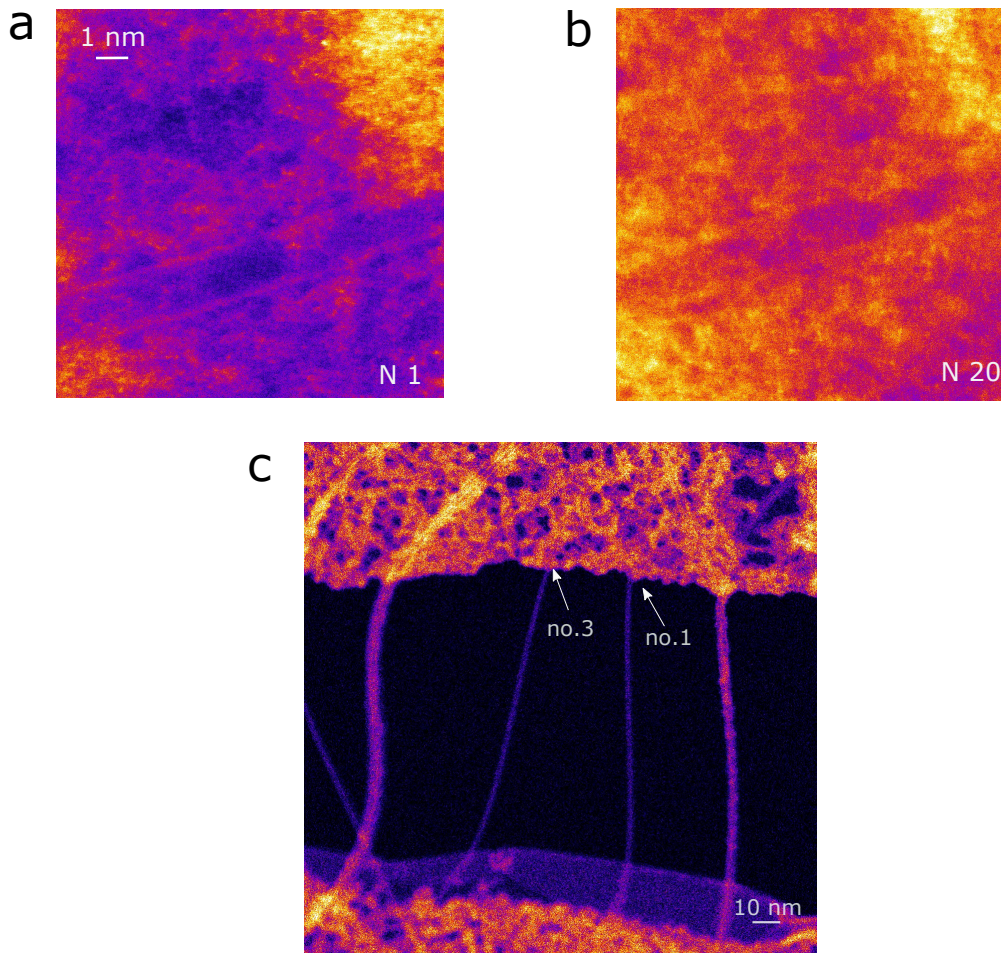


Figure 3.3: **Heavily contaminated CNTs on graphene.** (a), (b) STEM images from an irradiation series, frames 1 and 20 respectively (FOV of about 12 nm,  $1024 \times 1024$  pixels and  $16 \mu\text{s}$  dwell time). (c) a larger overview of spots 1 and 3 (FOV 192 nm,  $1024 \times 1024$  pixels and  $4 \mu\text{s}$  dwell time).

best compromise between resolution, to observe clearly what is happening in the experiment, and the time passed between frames, in order to keep track of the processes going on, is made. The scan direction is preferably chosen perpendicular to the tube axis, optimizing the resolution for further analysis. The diameter and chiral angle, if the resolution allows it, are determined as described in sec. 3.1. Detailed information on this analysis is given in Tab. 3.1. The image calibration is done in the image of spot 4, as it shows the best resolution of this experiment. The overview in Fig. 3.4(f) show the CNTs after the irradiation. Within the FOV a lot of mobile contamination is piled up. The image was taken at a FOV of about 96 nm,  $1024 \times 1024$  pixels and  $16 \mu\text{s}$  dwell time. The electron doses until the first apparent damage of the CNT were analyzed as described in sec. 3.2.

At the end of the experiments a conclusive plot containing all electron doses of the various experiments will be given.

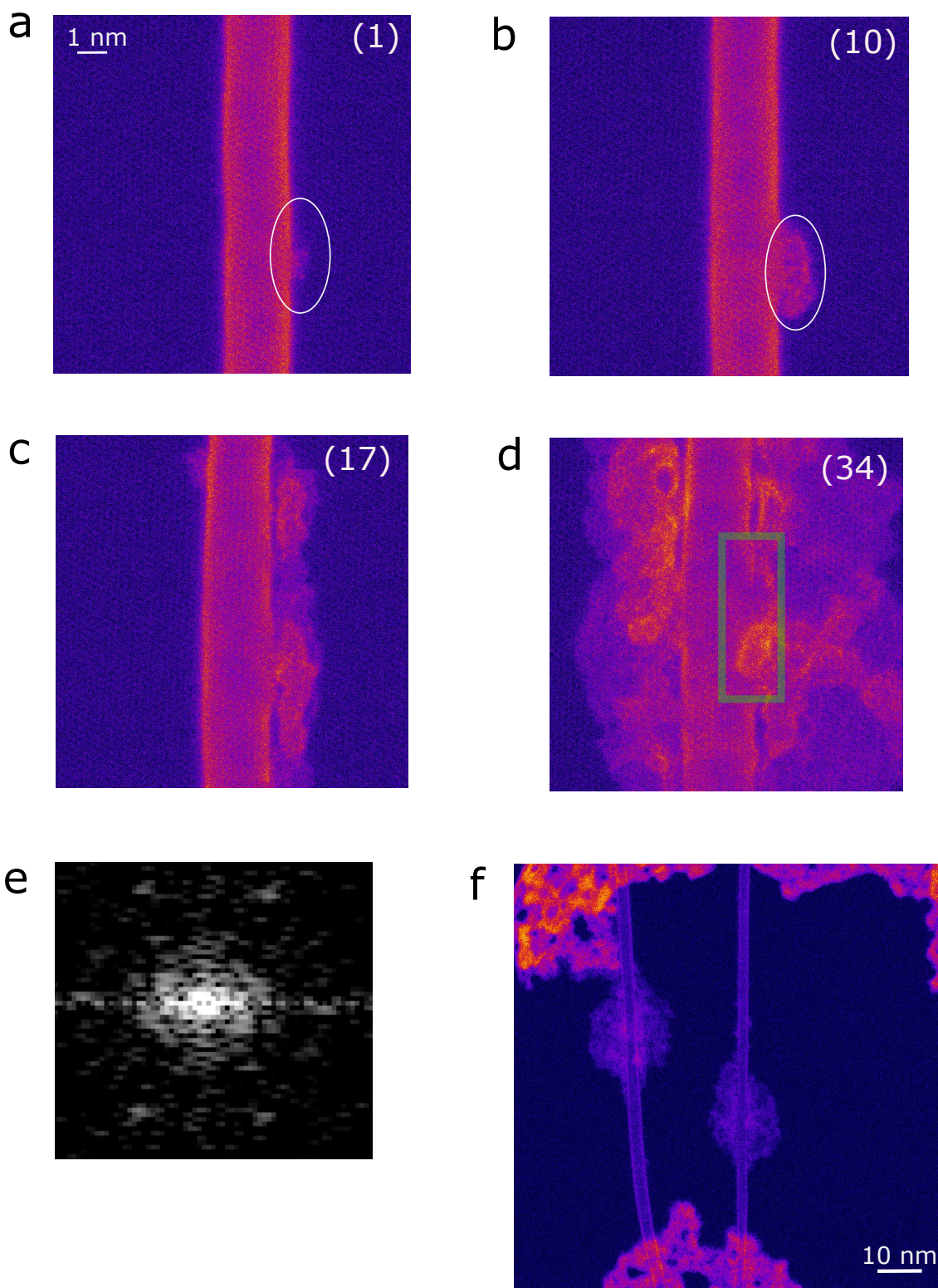


Figure 3.4: **Damaging of CNTs and accumulation of hydrocarbon contamination.** (a-d) STEM images from the irradiation series of sample spot 5 (FOV of about 12 nm,  $1024 \times 1024$  pixels and  $16 \mu\text{s}$  dwell time), mobile hydrocarbon contamination appears (white circles), frame numbers are given in white brackets, and the CNT is destroyed. (e) gives a FFT of the green area of d). (f) an overview of two CNTs after the irradiation (FOV of about 96 nm,  $1024 \times 1024$  pixels and  $16 \mu\text{s}$  dwell time).

Table 3.1: STEM data form irradiation series of sample no.192, the diameter, the chiral angle ( $D, \alpha$ ) are given,  $No_{damage}$  and  $No_{total}$  refer to the frame numbers of the series until the first clear damage appears and the total number of frames, respectively. Further the calibrated FOV is shown. All irradiation series are taken with  $1024 \times 1024$  pixels and  $16 \mu s$  dwell time.

sample spot	$D$ [nm]	$\alpha$ [°]	$No_{damage}$	$No_{total}$	FOV [nm]
1	-	-	-	21	11.78
3	-	-	-	24	11.78
4	$1.04 \pm 0.03$	$25.3 \pm 0.6$	2	39	5.89
5	$1.79 \pm 0.03$	$28.4 \pm 0.6$	1	38	11.78
6	$2.37 \pm 0.03$	$30.0 \pm 0.6$	1	22	5.89
8	$1.26 \pm 0.03$	$30.0 \pm 0.6$	1	21	11.78

In the third experiment with sample no.192 the same experimental approach in terms of tuning the microscope and sample spot fining was done. Unfortunately, no clean spots with CNTs suspended on graphene could be found. Therefore, this experiment didn't give any usable data in terms of CNT irradiation.

### 3.3.3 Sample no.239

In this experiment sample no.239 was used. It is on a Si-N grid. The graphene is grown by a standard CVD method including methane and copper substrate, a detailed description of the synthesis and the transfer method is given in sec. 2.2.2. The CNTs are deposited in a FC-CVD reactor with TP-collection, for details see 2.2.6. The CNTs face the electron beam. This sample was treated by a dry cleaning method involving active carbon, before it was loaded to the microscope's vacuum system. In this method the TEM-grids are buried into active carbon and with tweezers the active carbon is put close to the sample surface. Then the sample is put in an oven and is held at  $210^\circ C$  for 30 min. A detailed description of this method can be found in sec. 2.3.5. The experimental approach in terms of microscope tuning and finding sample spots for the irradiation was the same as just described at the beginning of sec. 3.3 and the microscope was operated at 60 keV. The active carbon treatment is effective in cleaning the graphene layer from hydrocarbon contamination, as can be observed in Fig. 3.5(d). This image is a zoom-in of an image with FOV of about 2048 nm with  $2048 \times 2048$  pixels and  $16 \mu s$  dwell time. The bright contrast of the contamination suggests that it contains a metal containing contamination, probably from the

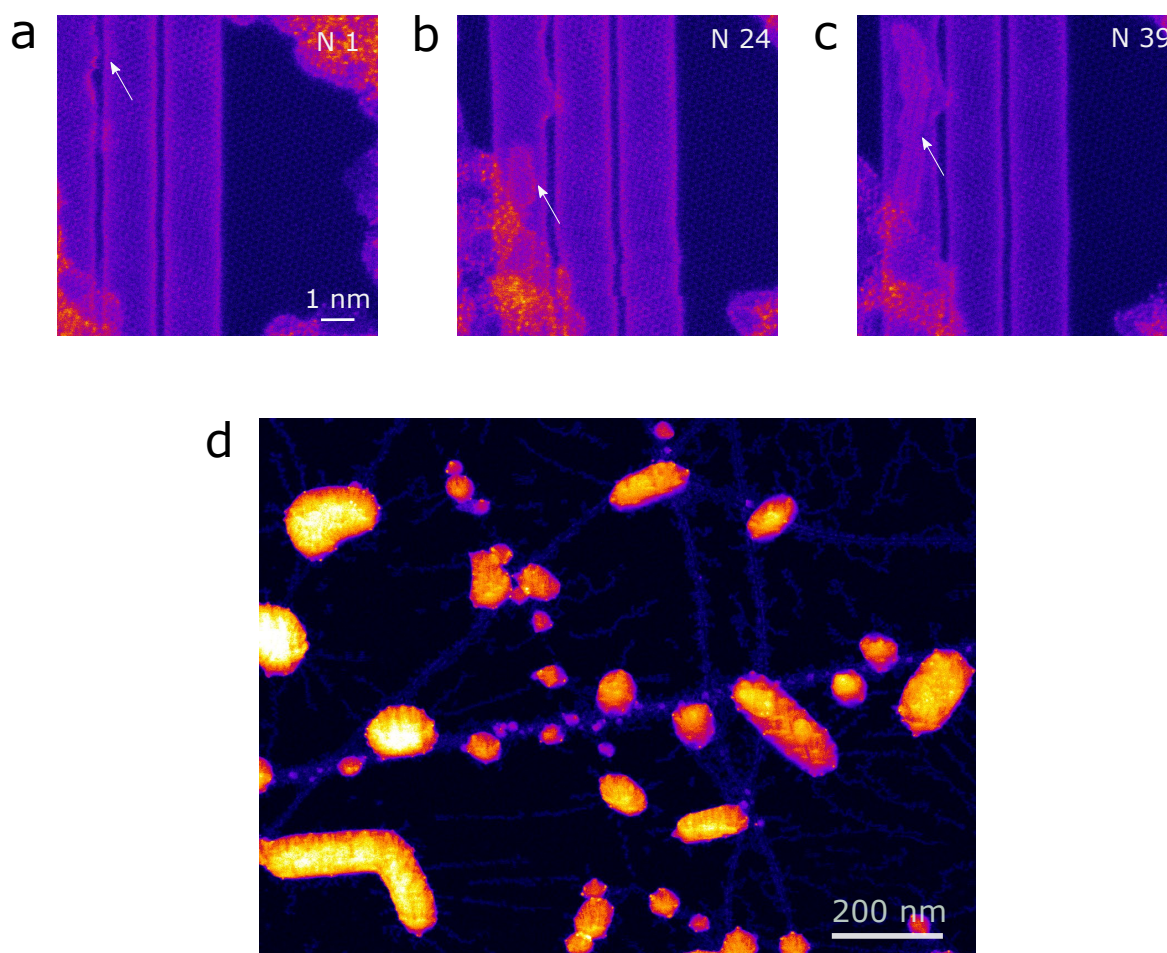


Figure 3.5: **CNT bundle and a nanobud.** (a-c) STEM images from an irradiation series, numbers refer to frame numbers (FOV of about 12 nm,  $1024 \times 1024$  pixels and  $16 \mu\text{s}$  dwell time). (d) a larger overview of sample no.239 (zoom-in of an image with FOV of about 2048 nm with  $2048 \times 2048$  pixels and  $16 \mu\text{s}$  dwell time).

copper substrate of the graphene synthesis. The issue is that this cleaning procedure does not remove the contamination from the CNTs and between the CNTs and the graphene. Therefore, it is not a useful approach for the needs of the current experiment. No clean individual CNTs on atomically clean graphene could be found in this experiment. What could be imaged though, was a bundle of three CNTs, as shown in Fig. 3.5(a-c). The images are recorded at a FOV of about 10 nm  $1024 \times 1024$  pixels and  $16 \mu\text{s}$  dwell time. A defect from the CNT synthesis can be observed in the left-most CNT. From frame 24 onward the growth of a carbon nanostructure, similar to a very defective fullerene or CNT can be observed. The structure continues with its growth until the end of the image series.

### 3.3.4 Sample no.333

In this experiment sample no.333 was imaged in the microscope. It is a Si-N sample with graphene and CNTs on top. Graphene is "Easy transfer" graphene from Graphenea (for details see sec. 2.2.2) and the CNTs were deposited by a FC-CVD method with TP-deposition (sec. 2.2.6). CNTs face the electron beam. The CNT concentration in this sample meets the requests of the experiment. There are enough CNT to find, but not an excess of bundling. The problem of this sample is the coverage with graphene. There are lots of empty holes in the Si-N film.

Sample spots 7, 9, 10, 14 and 16 were found. The CNT in spot 7 showed appearance of mobile contamination on the second frame and damage (FOV of about 6 nm,  $1024 \times 1024$  pixels and 16  $\mu$ s dwell time). CNT in spot 9 showed also damage, but only after 13 frames under the same experimental conditions and imaging parameters. One image after 39 frames is shown in Fig. 3.6(a). It is notable that there is clear damage of the CNT, since it shows a local change in diameter and chirality, but the damage looks different to all previous cases. In all cases up to this point a lot more mobile contamination was gathered next to the CNT and the process did not seem to reach an equilibrium, like in the present case. Spots 10 and 14 don't show damaging of the CNT. They were both stable for 32 frames at FOV of about 5 nm,  $1024 \times 1024$  pixels and 16  $\mu$ s dwell

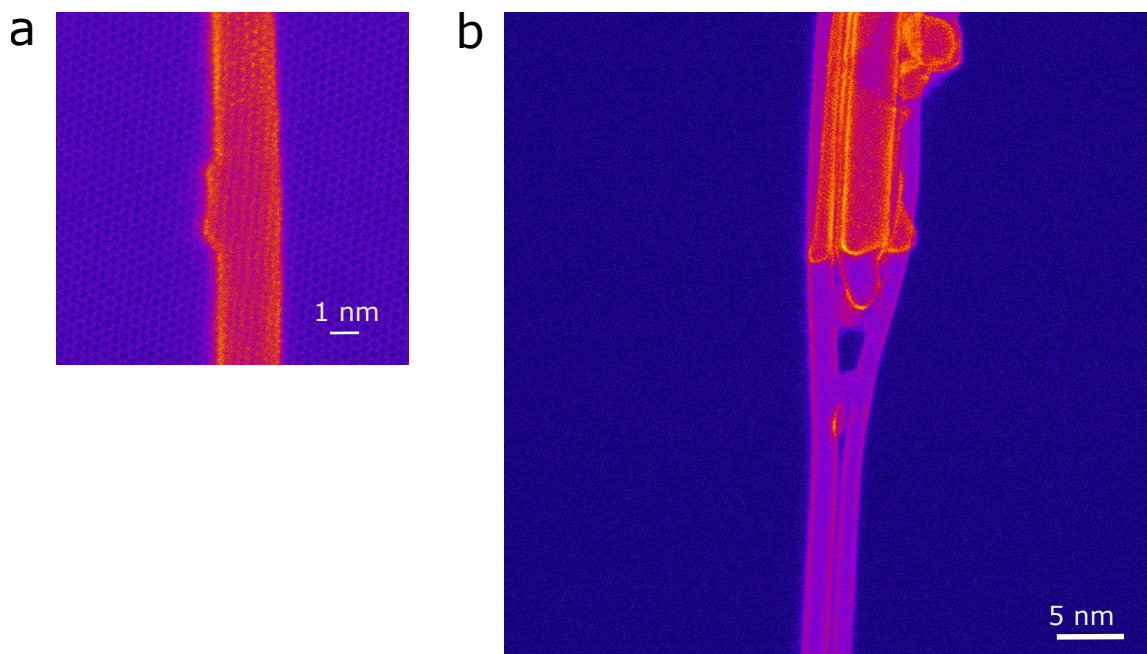


Figure 3.6: **CNT damage and multiple junction.** (a) an image after the irradiation (FOV of about 12 nm,  $1024 \times 1024$  pixels and 16  $\mu$ s dwell time). (b) an overview of the junction between several CNTs (FOV of about 48 nm,  $1024 \times 1024$  pixels and 64  $\mu$ s dwell time).

Table 3.2: STEM data form irradiation series of sample no.333, the diameter, the chiral angle ( $D, \alpha$ ) are given,  $No_{damage}$  and  $No_{total}$  refer to the frame numbers of the series until the first clear damage appears and the total number of frames, respectively. Further the calibrated FOV is shown. All irradiation series are taken with  $1024 \times 1024$  pixels and  $16 \mu s$  dwell time.

sample spot	$D$ [nm]	$\alpha$ [°]	$No_{damage}$	$No_{total}$	FOV [nm]
7	$1.00 \pm 0.03$	$22.7 \pm 0.6$	2	39	5.56
9	$1.46 \pm 0.03$	$20.8 \pm 0.6$	13	21	5.56
10	$1.62 \pm 0.03$	$27.9 \pm 0.6$	-	36	4.63
14	$1.35 \pm 0.03$	$26.8 \pm 0.6$	-	32	4.63
16	$1.17 \pm 0.03$	$27.6 \pm 0.6$	2	35	11.12

time. The CNT in spot 16 shows damaging and hydrocarbon contamination on the second frame (FOV of about 12 nm,  $1024 \times 1024$  pixels and  $16 \mu s$  dwell time). The diameter and chiral angle were measured and the image calibration was done in spot 16, as it shows the best resolution (for details see sec. 3.1). A compact version of the analyzed data are given in Tab. 3.2.

Two bundles are imaged in this experiment. The first one is a bundle of three CNT and it was stable under the electron beam for 21 frames at a FOV of 12 nm,  $1024 \times 1024$  pixels and  $32 \mu s$  dwell time. The second one is a junction between SWCNTs and MWCNTs and can be observed in Fig. 3.6(b).

### 3.3.5 Hypothesis for the damaging mechanism at UHV

The damage to CNTs at UHV does not happen to all of them. An exact ratio will be given after the end of all experiments. When damage occurs in all cases beside one, mobile contamination appears in the FOV at the nucleation site of the damage and further contamination is built up and the CNT is destroyed. In the special case (spot 13, Fig. 3.6(a)) there is certainly damage but the carbon atoms most probably originating from hydrocarbon contamination are integrated in the graphitic CNT network. The damage under stable hydrocarbon contamination, as observed by [56], was not observed in the experiments. It remains unclear what the damage depends on. One could think that the atomically clean area that is available for surface diffusion plays a role. The idea is that when the hole in the thick surrounding contamination is in the order of the FOV, the electron beam would form an amorphous carbon ring acting as diffusion barrier. Unfortunately, there is no larger FOV overviews taken of every sample spot allowing to make

conclusive analysis of that. The damage was also observed on different samples. As knock-on damage can be excluded at used experimental condition and ionization and excitation are not present in the studied system, there is a strong indication that this damaging process depends on the local atmosphere in the microscope.

There are two types of hypotheses for the damaging mechanism at UHV condition. The first one is to assume that the CNTs have small defects or lattice imperfections from the CNT synthesis that can not be seen in the STEM images due to the substantial amount of graphene background. The second type of hypotheses argues that there are no defects, but they are formed within the experiment. Firstly, one could think of the geometry of system, unlike plain graphene, allows chemical elements to bond to carbon atoms of the CNT causing a defect by a chemical process. It is though questionable, whether the adatom can be stable under electron radiation. The energy for the process must be delivered by the electron beam, as the energy barriers are not exceeded thermally. Secondly, a hydrogen assisted chemical knock-on damage is conceivable. Theoretically, those knock-on events are described by a relativistic elastic scattering, as discussed in the conventional knock-on damage by [53, 54]. Assuming the easiest model, this can be reduced to a backscattering event of the electron at the hydrogen and a central hit between the hydrogen and the carbon atom where the energy transfer is maximized and all three atoms move on one line. The hydrogen is found in the middle of the curved graphene layer and the CNT. The question how likely it is to find the hydrogen at this place is left beside for the moment. This calculation should only give an idea, if the enhancement in the transfer of energy can be high enough to exceed the threshold energy at 60 keV. The incoming electron with mass  $m_e = 9.109 \times 10^{-31}$  kg and energy of 60 keV is backscattered at the hydrogen atom, mass  $m_H = 1.674 \times 10^{-27}$  kg. Then the hydrogen hits the carbon atom, mass  $m_C = 1.994 \times 10^{-26}$  kg. The maximum transferred energy is 46 eV. This exceeds the threshold energy of carbon atoms in CNT of about 20 eV clearly. It is hence conceivable that  $H_2$  is split into atomic hydrogen by the electron beam. Then the hydrogen atoms diffuse to the sidewalls of the CNTs acting as a barrier. The electron energy is transferred through the hydrogen and a carbon atom is ejected.

In both cases the defective site acts as a nucleation site for the damaging process. The chemical elements are split under the electron beam before landing on the sample surface and diffuse. The chemical etching of graphene involving oxygen, water and air has been observed. The chemical etching results in creation of further reactive site leading to an accumulation of mobile contamination.

The test of these hypotheses is realized experimentally by electron irradiation experiments under controlled O<sub>2</sub>, H<sub>2</sub> and H<sub>2</sub>O atmospheres.

## **3.4 (Ir)radiation of CNTs under hydrogen, oxygen and water atmospheres**

### **3.4.1 Sample no.374**

The next experiment was done with sample no.374. It is on a Si-N TEM-grid. The graphene are nanoflakes. The sample was produced for a different purpose. The fact that there is no large covered areas with graphene, makes it not particularly suitable for the present experiment. The exact growth parameter and type are not known. The CNTs were deposited on top of the graphene by a FC-CVD method with TP-deposition, for details look sec. 2.2.6. The CNTs face the electron beam. The experimental approach in terms of microscope tuning and finding sample spots for the irradiation was the same as just described at the beginning of sec. 3.3 and the microscope was operated at 60 keV. The sample shows almost no CNTs at all. But the few CNTs that can be found are individual. This is the first experiment under controlled atmospheres. The experimental set-up is described in sec. 2.3.3. The pressure can be monitored by checking the objective gauge (OG) pressure of the microscope. When starting to increase cautiously, the pressures must be checked directly at the microscope's hardware and not at the computer, as there can be some time latency in the reported data. Increasing the pressure unwillingly too high can destroy the entire microscope vacuum. Therefore, these experiments can not be done alone. Prior to the actual experiment, the whole line reaching the valve at the column of the microscope is flushed with Ar and consequently pumped out again several times. The line is pumped down by opening the valve connecting the main line and the pump. The Ar and O<sub>2</sub> gas bottles are equipped with a pressure regulator. The right manometer shows the pressure in the right volume connected to the bottle and the left one the pressure in left chamber. An overpressure of about 1 bar is tuned with the central rod. Then the line can be filled with Ar by opening the valve connecting the line and the left chamber. The line can be filled with O<sub>2</sub> in the same way as just described for the case of Ar. In the case of H<sub>2</sub> only a single manometer and a valve are available. The water leakage is performed by pumping down the line and opening the valve between the main line and container with distilled water. The leakage experiments can be done to pressures

up to mid  $10^{-6}$  Torr range without destroying the microscope's vacuum system.

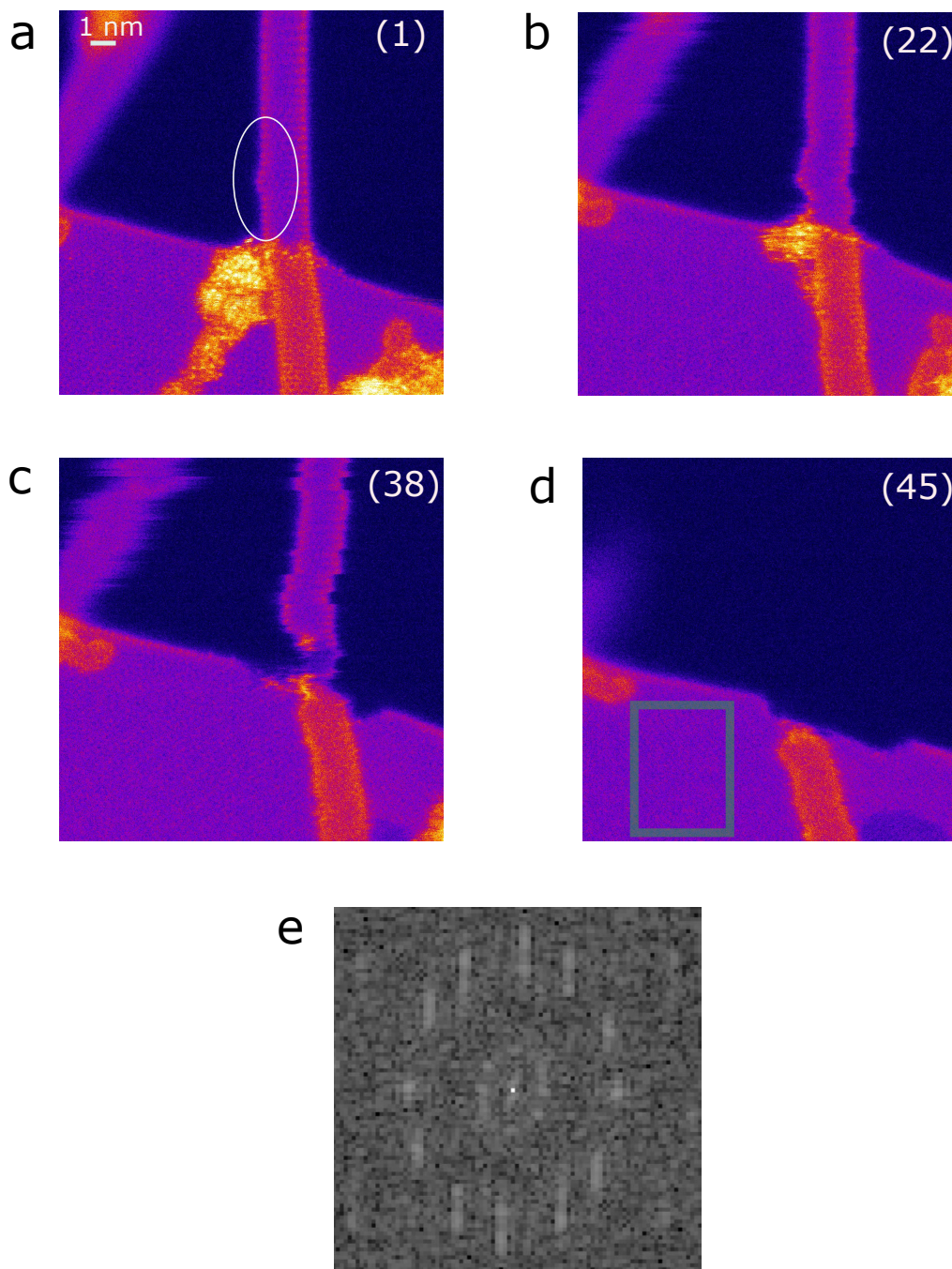


Figure 3.7: **Damage under oxygen atmosphere.** (a-d) STEM images from an irradiation series (FOV of 12 nm,  $1024 \times 1024$  pixels and  $16 \mu\text{s}$  dwell time) of spot 18 of sample no.334 under  $\text{O}_2$  leakage, the CNT has a clear defect (white circle), frame numbers are given in white brackets. (e) gives a FFT of the green area of d).

Sample spot 17 is found in this experiment. The CNT is  $(1.08 \pm 0.03)$  nm in diameter and has a chiral angle of  $(3.4 \pm 0.6)^\circ$ . The image calibration was done in the first STEM image of the irradiation series, the diameter and the chiral angle was determined as described in sec. 3.1. Some images of the irradiation series are given in Fig. 3.7(a-d).  $\text{O}_2$  is intentionally leaked into the

microscope column. The leakage was done while STEM images were recorded. The pressure was of  $(1.16 \pm 0.08 \times 10^{-6})$  Torr. The pressure was not held constant throughout the irradiation series, as the microscope's vacuum system continuously pumps out the residual gas. The uncertainty is given by the standard deviation of all pressure values measured at every frame. The CNT shows a defect yielding from the CNT synthesis (white circle), as knock-on damage can be excluded at the used 60 keV electron acceleration. The CNTs starts to etch in the area where the defect is found. The spot was imaged for 45 frames (FOV of 12 nm,  $1024 \times 1024$  pixels and 16  $\mu$ s dwell time) until the CNT was completely etched. The first visible damage could be observed after 22 frames. The CNT is suspended on a folded graphene sheet. Moiré pattern can be observed in the graphene. Moiré patterns are formed when two periodic patterns are laid one over the other by a relative twist [69]. The hexagon-shaped diffraction maxima, as can be observed in the FFT (Fig. 3.7(e)) of the STEM image, show that it is two layers. The graphene starts to etch at the fold after the CNT is cut completely.

### 3.4.2 Sample no.334

The sample is on a SiN TEM-grid. Graphene is Graphenea "Easy transfer" graphene, a detailed description of the sample preparation is given in sec. 2.2.2. The CNTs were deposited by a FC-CVD method with TP-collection (sec. 2.2.6). The CNTs face the electron beam. Three experiments were done with this sample.

**Experiment 1** The experimental approach in terms of microscope tuning and finding sample spots for the irradiation was the same as just described at the beginning of sec. 3.3 and the microscope was operated at 60 keV. Sample spots 11, 12, 13 and 18 were found in this experiment. 11, 12 and 13 are imaged under UVH condition. The CNT in spot 12 and 13 shows damage on the first frame and 11 is stable for 28 frames. In spot 18 a controlled oxygen experiment was done and then an irradiation series was recorded, like described in sec. 3.4.1. The CNT was stable under oxygen leakage. The diameter is calculated. The resolution is not high enough to allow the measurement of the chiral angle. The image calibration was done in one of the images of spot 11. For detailed information on this analysis procedure look sec. 3.1. A compact version of the data is shown in Tab. 3.3.

One CNT with a defect from CVD synthesis and another without apparent defect could be imaged. As knock-on damage is to be excluded at the used 60 keV it is assumed that it was formed

Table 3.3: STEM data form irradiation series of sample no.334, the diameter, the chiral angle ( $D, \alpha$ ) are given,  $No_{damage}$  and  $No_{total}$  refer to the frame numbers of the series until the first clear damage appears and the total number of frames, respectively. Further the calibrated FOV is shown. The average OG pressure during the experiment are given. All irradiation series are taken with  $1024 \times 1024$  pixels and  $16 \mu s$  dwell time.

sample spot	$D$ [nm]	$\alpha$ [°]	$No_{damage}$	$No_{total}$	FOV [nm]	gas	$\mu_{pOG}$ [Torr]
11	$1.44 \pm 0.03$	-	-	28	8.51	-	UHV
12	$0.92 \pm 0.03$	-	1	18	10.63	-	UHV
13	$0.71 \pm 0.03$	-	1	11	8.51	-	UHV
18	$1.96 \pm 0.03$	-	-	21	12.76	O <sub>2</sub>	$(1.12 \pm 0.06) \times 10^{-6}$

during the growth. The defective one (spot 17, Fig. 3.7) shows chemical etching behavior and the complete eventual destruction of the CNT. The second CNT from spot 18 where no apparent defects in the STEM image are visible is stable. This is in alignment with observations of graphene, as only defective sites show etching and the pristine lattice remains untouched [1]. The folded graphene edge from spot 17 also showed chemical etching, although there are no apparent defects visible. It is probable that due to the folding, the carbon bonds are strained and become much more chemically reactive, similar to what is observed in CNTs with diameters smaller than 0.7 nm. It is remarkable though, that the etching only started when the CNT was completely cut. The outcome of these two experiments support the hypothesis that defects yielding from the synthesis in the CNT act as nucleation site for chemical etching process involving oxygen and play a role in the observed damage at UHV condition. Furthermore, the fact that the part of the CNT that was freely suspended was damaged, indicates that the in-tube diffusion of molecules needs to be taken into account.

**Experiment 2** The experimental approach in terms of microscope tuning and finding sample spots for the irradiation was the same as just described at the beginning of sec. 3.3 and the microscope was operated at 60 keV. Spot 20 was found in this experiment. The scan is set up and an UHV irradiation series is done. The CNT is stable for 66 frames (FOV of 8 nm,  $1024 \times 1024$  pixels and  $16 \mu s$  dwell time). Then the oxygen experiment was performed, for details look sec. 3.4.1. The OG pressure was of  $(1.31 \pm 0.12) \times 10^{-6}$  Torr. No damage happened in this experiment and the CNT was stable for 46 frames at the same experimental condition. Then the pressure was pumped down again to  $10^{-9}$  Torr range by the microscope's vacuum system. It would take too long

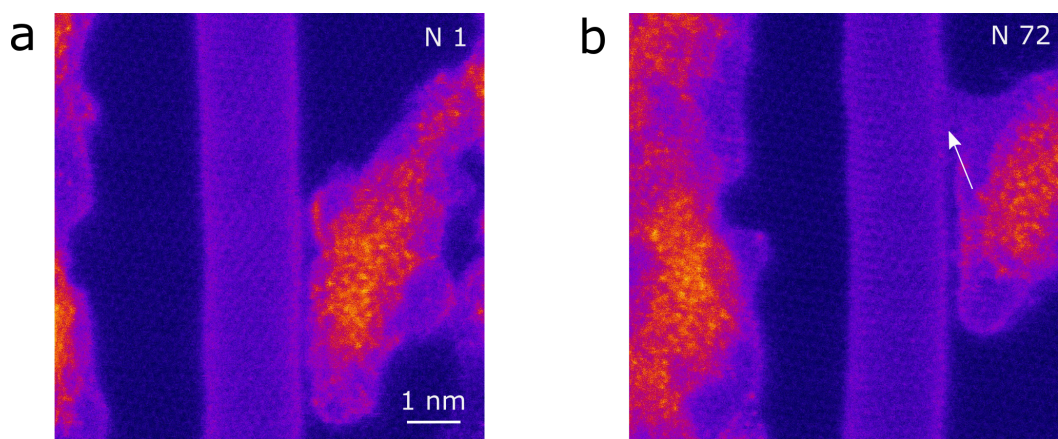


Figure 3.8: **Damage under water atmosphere.** (a), (b) STEM images from an irradiation series under H<sub>2</sub>O leakage, the CNT shows clear damage and the sidewall is broken (white arrow).

to pump down to  $10^{-10}$  Torr range. But as the oxygen leakage didn't show any difference, some residual of the gas won't compromise the upcoming experiment. Analogously, hydrogen was leaked to the microscope column at a pressure of  $(1.32 \pm 0.12) \times 10^{-6}$  Torr. No damage occurred of any kind for 68 frames at the same experimental parameters. In both leakage experiments there is no fundamental difference to the UHV case. Then with the same procedure as before, H<sub>2</sub>O is leaked into the microscope at an OG pressure of  $(1.61 \pm 0.13) \times 10^{-6}$  Torr. In Fig. 3.8(a) a STEM image of the irradiation series can be observed. The CNT shows eventual damaging with clear break of the CNTs sidewalls (Fig. 3.8(b)). The CNT is not destroyed completely and no further mobile contamination is gathered. Spot 20b is the same CNT several dozens of nm away for the original imaged spot. It was imaged under H<sub>2</sub>O leakage. This spot showed the same damaging, as the original spot, after 20 frames (FOV of 8 nm,  $1024 \times 1024$  pixels and  $16 \mu\text{s}$  dwell time). The diameter, chiral angle are analyzed and the image calibration was done in the first image of the UHV series in spot 20, as described in sec. 3.1. The analyzed data, the gas pressures of the leakages, the number of the frame in which damage occurs and the total frame numbers can be seen in Tab. 3.4.

**Experiment 3** The experimental approach in terms of microscope tuning and finding sample spots for the irradiation was the same as just described at the beginning of sec. 3.3 and the microscope was operated at 60 keV. In this experiment spot 21, 22, 22b, 22c, 22d, 23 and 24 are imaged. Of spot 21 an UHV control series is performed. The CNT is stable for 162 frames (FOV of 8 nm,  $1024 \times 1024$  pixels and  $16 \mu\text{s}$  dwell time). Then H<sub>2</sub>O is leaked in the microscope column. The CNT in 21 shows clear damage after 37 frames, under same experimental parameters, and gets

Table 3.4: STEM data form irradiation series from sample no.334, the diameter, the chiral angle ( $D, \alpha$ ) are given,  $No_{damage}$  and  $No_{total}$  refer to the frame numbers of the series until the first clear damage appears and the total number of frames, respectively. Further the calibrated FOV is shown. The leaked gas and the average OG pressure during the experiment are given. Note that spot 23 is a freely suspended CNT. All irradiation series are taken with  $1024 \times 1024$  pixels and  $16 \mu s$  dwell time.

spot	$D$ [nm]	$\alpha$ [°]	$No_{damage}$	$No_{total}$	FOV [nm]	gas	$\mu_{p_{OG}}$ [Torr]
20	$1.62 \pm 0.03$	$4.5 \pm 0.6$	-	66	8.33	-	UHV
20	$1.62 \pm 0.03$	$4.5 \pm 0.6$	-	46	8.33	O <sub>2</sub>	$(1.32 \pm 0.23) \times 10^{-7}$
20	$1.62 \pm 0.03$	$4.5 \pm 0.6$	-	68	8.33	H <sub>2</sub>	$(1.3 \pm 0.3) \times 10^{-7}$
20	$1.62 \pm 0.03$	$4.5 \pm 0.6$	69	100	8.33	H <sub>2</sub> O	$(1.6 \pm 0.4) \times 10^{-7}$
20b	$1.64 \pm 0.03$	-	20	54	8.33	H <sub>2</sub> O	$(1.23 \pm 0.24) \times 10^{-7}$
21	$1.24 \pm 0.03$	$19.1 \pm 0.6$	-	162	8.26	-	UHV
21	$1.24 \pm 0.03$	$19.1 \pm 0.6$	37	85	8.26	H <sub>2</sub> O	$(7.7 \pm 0.3) \times 10^{-7}$
22	$1.31 \pm 0.03$	-	2	40	8.26	H <sub>2</sub> O	$(7.73 \pm 0.21) \times 10^{-7}$
22b	$1.32 \pm 0.03$	-	1	17	8.26	H <sub>2</sub> O	$(7.75 \pm 0.07) \times 10^{-7}$
22c	$1.31 \pm 0.03$	-	4	73	8.26	H <sub>2</sub> O	$(1.2 \pm 0.3) \times 10^{-7}$
22d	-	-	1	45	8.26	H <sub>2</sub> O	$(1.03 \pm 0.22) \times 10^{-7}$
23	$0.87 \pm 0.03$	$4.3 \pm 0.6$	30	90	8.26	H <sub>2</sub> O	$(9.61 \pm 0.23) \times 10^{-8}$
24	$1.01 \pm 0.03$	-	1	23	8.26	H <sub>2</sub> O	$(8.98 \pm 0.04) \times 10^{-8}$

cut completely slightly outside the FOV. Spots 22, 22b, 22c and 22d are the same CNT several dozens of nm away from each other. In all spots a larger overview (FOV of 48 nm) before and after the irradiation series is taken. All CNTs in these spots show clear damaging in the first frames of the irradiation at the same experimental condition. In 22 and 22b first the hydrocarbon contamination is etched and then the entire CNT is etched away. In Fig. 3.9(a)(b) two STEM images of spot 22b are shown. A larger overview of the spot (Fig. 3.9(c)) shows that the CNT is completely etched even outside the FOV of the irradiation series. What can also be observed is that the graphene is also prone to chemical etching presumably at the grain boundaries that are covered by thick hydrocarbon contamination. In spot 22c and 22d the CNT gets cut completely slightly outside the FOV. 22d is remarkable, because it does not only show the etching but there is a bud-like feature at the bottom of the image, as can be observed in Fig. 3.10(a)(b). This structure is surprisingly not prone to any damage, only the hydrocarbon contamination is etched

away. It is stable for the whole 45 frames, same experimental condition, of this irradiation series. Sample spot 23 (Fig. 3.11(a)) is a vacuum control experiment with a freely suspended CNT without graphene. Also in this spot hydrocarbon contamination is etched away and the CNT shows clear damaging after 29 frames, same experimental condition, in two different places (white arrows in Fig. 3.11(b)).

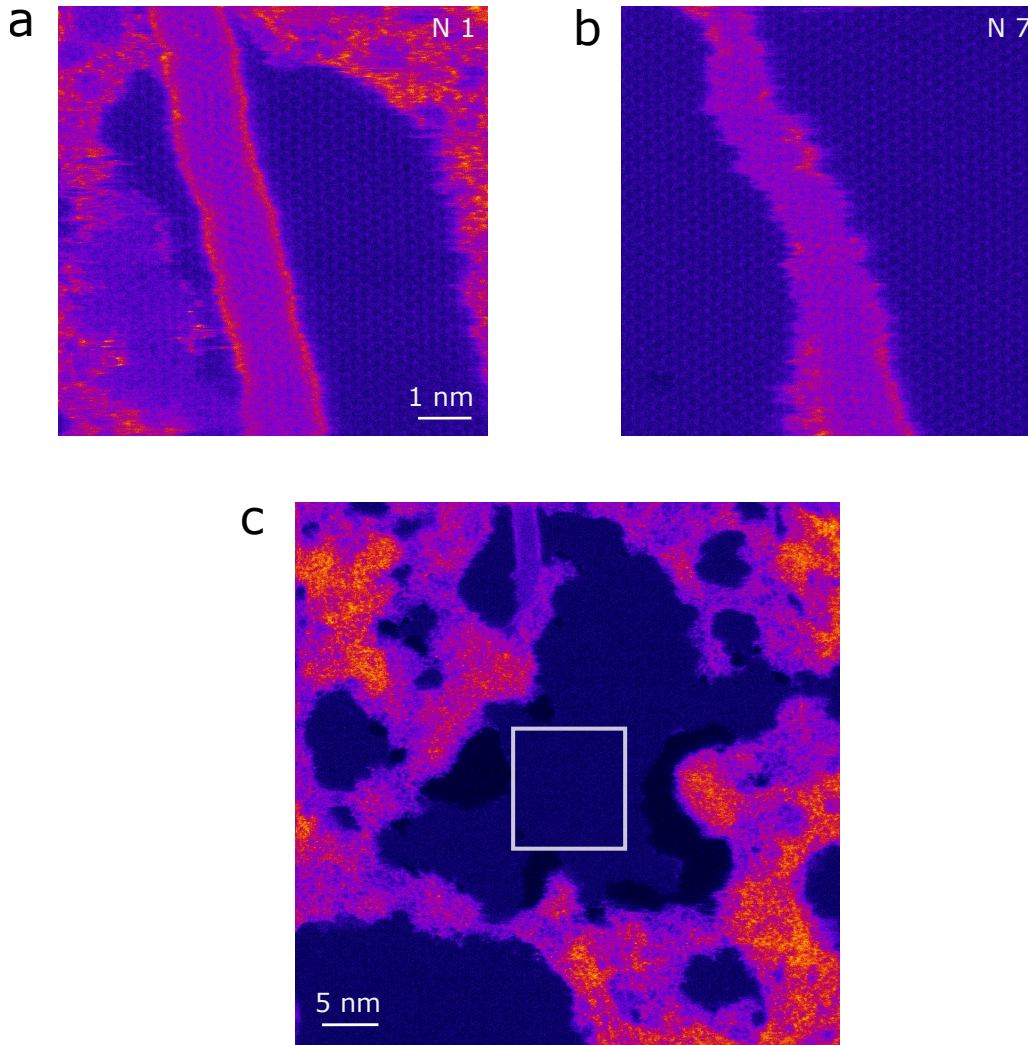


Figure 3.9: **Complete etching under water atmosphere.** (a), (b) STEM images (FOV of 8 nm,  $1024 \times 1024$  pixels and  $16 \mu\text{s}$  dwell time) from an irradiation series of spot 22b on sample no.334 under  $\text{H}_2\text{O}$  leakage, the CNT shows clear damage and is completely etched away. (c) an overview (FOV of 48 nm,  $1024 \times 1024$  pixels and  $16 \mu\text{s}$  dwell time) after the irradiation, white square shows the position of the irradiation.

In spot 24 the CNT gets damaged in the first frame and a lot of mobile hydrocarbon contamination is attracted. The process seems very similar to one observed under UHV condition, described in sec. 3.3. The diameter, chiral angles are measured and the image calibration was done in the first frame of spot 22, as described in sec. 3.1. The analyzed data, the pressures of the leakages, the

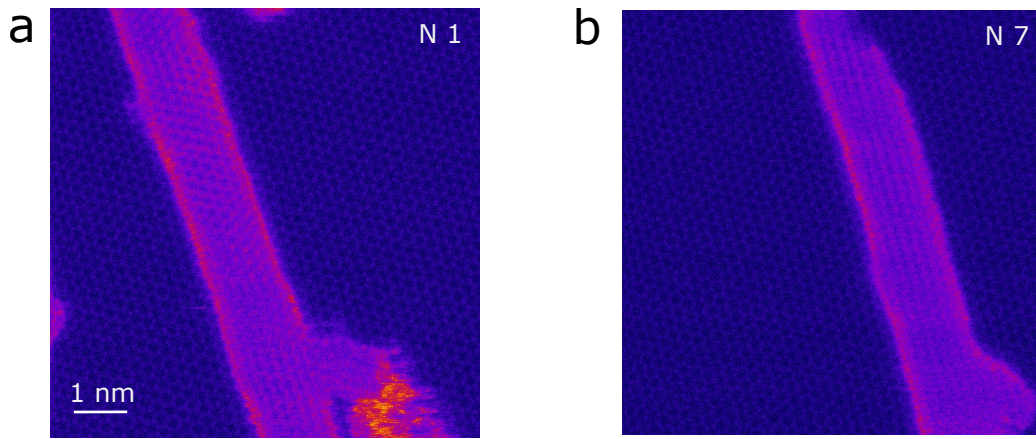


Figure 3.10: **Etching and nanobud formation under water leakage.** (a), (b) STEM images (FOV of 8 nm,  $1024 \times 1024$  pixels and  $16 \mu\text{s}$  dwell time) from an irradiation series of spot 22d under  $\text{H}_2\text{O}$  leakage, appearing of a budlike feature and clear damage at the top part.

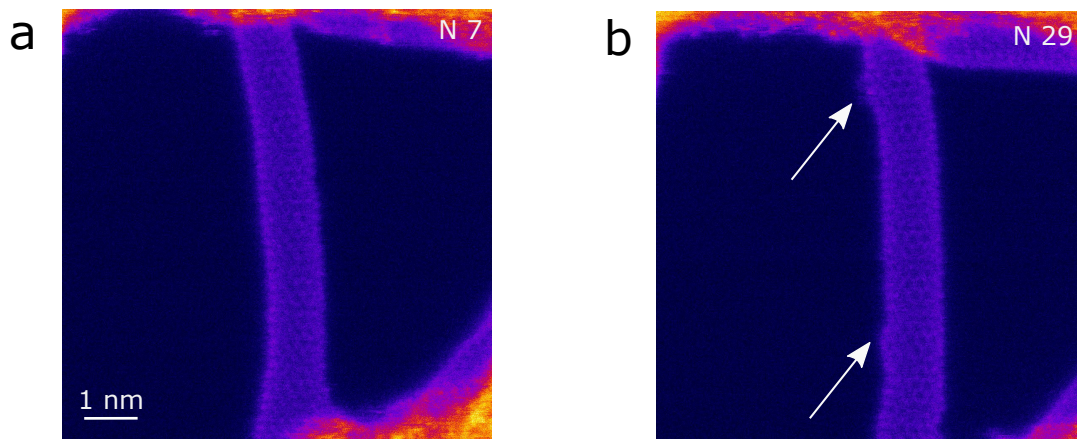


Figure 3.11: **Damage of a freely suspended CNT under water leakage.** (a),(b) STEM images of an irradiation of spot 23 (FOV of 8 nm,  $1024 \times 1024$  pixels and  $16 \mu\text{s}$  dwell time) of a freely suspended CNT from an irradiation series under  $\text{H}_2\text{O}$  leakage.

total frame numbers and the number of the frame in which damage occurs can be seen in Tab. 3.4.

In one case of the irradiation experiments (Fig. 3.12(a)) also damage to graphene could be observed. A clear monovacancy is visible (Fig. 3.12(b)). The position where the damage happened was originally covered with hydrocarbon contamination. This contamination was etched away and then the defect became visible. In the next frames further contamination appears and a hole in the graphene is formed (Fig. 3.12(c)(d)).

The CNT in spot 20 was imaged in all three controlled gas atmospheres ( $\text{H}_2$ ,  $\text{O}_2$  and  $\text{H}_2\text{O}$ ). The cases for  $\text{H}_2$  and  $\text{O}_2$  do not show any damaging of the CNT.  $\text{O}_2$  shows the chemical etching of hy-

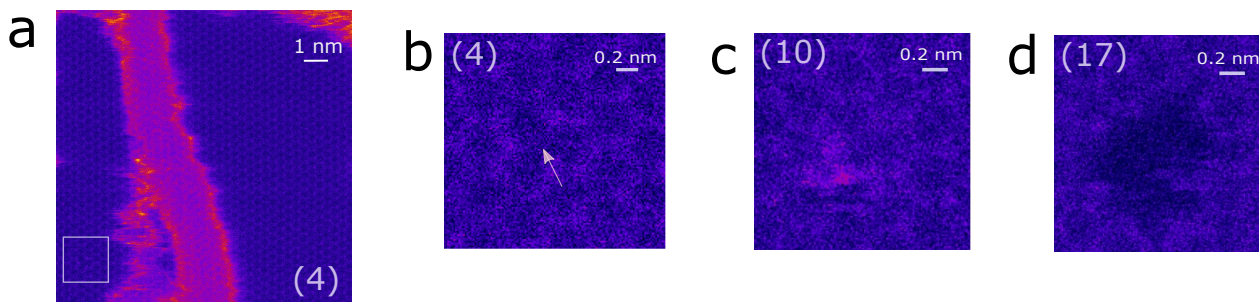


Figure 3.12: **Chemical etching of graphene.** (a) a STEM images from an irradiation series (FOV of 12 nm,  $1024 \times 1024$  pixels and  $16 \mu\text{s}$  dwell time), frame numbers are given in white brackets. (b) zoom of white box in a), graphene shows a clear monovacancy (white arrow). (c-d) further zoom-ins of the same image series.

drocarbon contamination. The  $\text{H}_2$  case cannot be distinguished from the UHV case. This matches the experimental observations dealing with graphene by [1]. The hypothesis of hydrogen assisted knock-on damage is falsified by this experiment. When  $\text{H}_2\text{O}$  is leaked into the column, the CNT gets damaged by chemical etching. This damaging behavior was observed in eight independent positions of CNTs on graphene and there are no cases where the damage does not happen under the leakage. There is also one case where a freely suspended CNT, is damaged under  $\text{H}_2\text{O}$  leakage (CNT in spot 23). It is difficult to quantify the damage of the CNTs. In 2D materials, like graphene, the etching rate can be accessed in terms of atoms per second by measuring the area of the produced hole, like done by [2]. In the case of CNTs the formation of defects causes a local change in chirality, not a hole. In the STEM image only a 2D projection of the CNT can be accessed. This cannot give a precise estimate on how many carbon atoms are etched away. Another problem is that the model proposed by [35] does not make correct predictions for the case of graphene and there is no reason that it would fit better to the present case. Hydrocarbon contamination is prone to etching and the chemical etching happens also outside the FOV implying that chemical processes are not completely localized under the electron beam. Graphene etches at the positions where there is thick hydrocarbon contamination and presumably grain boundaries or other lattice imperfections. For what concerns the hypothesis that defects from the CNT synthesis play a key role in the damage observed at UHV, remains untouched by the outcome of this experiments. But what can be stated is that, as the CNT was stable under  $\text{O}_2$  atmospheres and did damage under  $\text{H}_2\text{O}$  leakage, pre-existing defects are not a necessary condition for the process to take place and chemical etching can also occur to the carbon atoms of pristine CNTs. The chemical etching to graphene only happened once at a contamination site. It is very probable that there was a pre-existing defect from CNT synthesis that attracted contam-

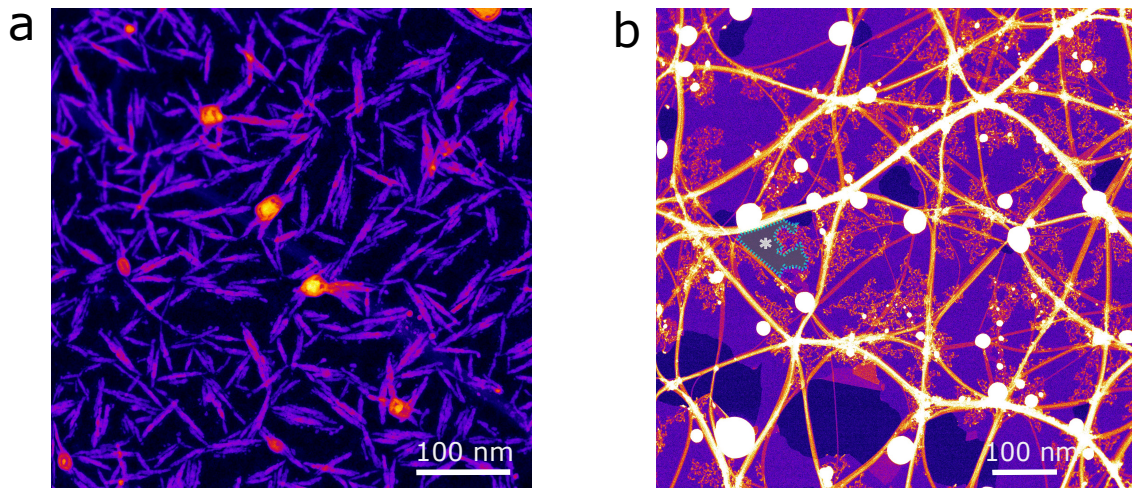


Figure 3.13: **Sample overview before and after laser cleaning.** (a) an overview (FOV of 512 nm,  $2048 \times 2048$  pixels and  $8 \mu\text{s}$  dwell time) of sample no.1095, needle-like contamination can be observed. (b) an overview (FOV of 640 nm,  $2048 \times 2048$  pixels and  $16 \mu\text{s}$  dwell time) of the same sample with CNTs on top of graphene after the laser cleaning procedure.

ination due to enhanced chemical reactivity. It is very unlikely that it reproduces the claim of an OH-group assisted point defect formation to pristine graphene by [12].

### 3.4.3 Sample no.1094 and 1095

**Experiment 1** In this experiment samples no.1094 and 1095 are used. They are Graphenea ready-to-use TEM goldgrids with standard CVD-grown graphene. The CNTs are deposited in a FC-CVD reactor with standard filter collection, for details see sec. 2.2.6. Sample no.1095 was made for a different purpose and after the CNT deposition a second graphene layer was added. The second graphene layer is grown by a standard CVD-method including methane and a copper substrate. A detailed description of the synthesis and the transfer method is given in sec. 2.2.2. The experimental approach in terms of microscope tuning and finding sample spots for the irradiation was the same as just described at the beginning of sec. 3.3 and the microscope was operated at 60 keV. The aim of these experiments is to do UHV control series for the further leakage experiments. Sample 1094 was scanned globally in CCD-mode at roughly  $-100\,000$  nm defocus. No graphene and CNTs could be found and the Quantifoil showed cracks. Sample 1095 showed a good coverage of graphene of the first layer. There is a second layer visible in some positions, but there is enough monolayer portions that meet the request of the experiment. CNTs can be found, but not in every hole. Individual CNTs on graphene can be found. The sample shows needle-like contamination, as one can observe in Fig. 3.13(a). Three experiments were done with

this sample. The sample has too much contamination in order to directly find atomically clean spots with both CNTs and graphene. For that reason a laser-cleaning procedure is applied. The recent version of the laser cleaning set-up is used from now on, as described in the second part of sec. 2.3.5. Prior to the lasering, the stage is driven to zero defocus. The laser is enabled in the menu of the microscope's software. Then the laser is pulsed at the chosen settings, this can be heard by the shutter's noise. The laser was operated at 30 mW for 2500  $\mu$ s. The whole hole in the Quantifoil becomes significantly cleaner after the procedure. The needle-like contamination is concentrated into dots of contamination, as it is shown in Fig. 3.13(b). The brightness of the contrast suggests that the contamination contains metals, presumably copper yielding from the graphene synthesis. In this imaged hole there is dozens of clean CNTs on atomically clean graphene. To quantify the laser cleaning effect, in a large overview (FOV 640 nm) image ten

Table 3.5: STEM data form irradiation series of sample no.1095, the diameter, the chiral angle ( $D, \alpha$ ) are given,  $No_{damage}$  and  $No_{total}$  refer to the frame numbers of the series until the first clear damage appears and the total number of frames, respectively. Further the calibrated FOV is shown. All irradiation series are taken with  $1024 \times 1024$  pixels and 16  $\mu$ s dwell time.

sample spot	$D$ [nm]	$\alpha$ [°]	$No_{damage}$	$No_{total}$	FOV [nm]
31b	$1.36 \pm 0.03$	-	-	80	10.04
31c	$1.39 \pm 0.03$	-	-	80	10.04
32	$1.03 \pm 0.03$	-	-	80	10.04
33	$2.53 \pm 0.03$	-	-	80	10.04
34	$0.97 \pm 0.03$	-	-	80	10.04

random atomically clean positions are selected and the area is measured. CNTs are equally to thick hydrocarbon contamination considered as diffusion barriers. The measuring procedure for one area can be seen in (\*) of Fig. 3.13(b). The mean of the area and the standard deviation give  $(2500 \pm 1300)$   $\text{nm}^2$ . There is one thing worth noting. The type of Van der Waals network of CNTs, as can be seen in Fig. 3.13(b), imply that the hole was empty during the CNT deposition. CNTs that land on a surface during deposition bundle less. This gives the opportunity to image the system in upside down configuration, so that the graphene layer faces the electron beam. The monolayer graphene that is visible yields from the adding of the second layer. Form spot 31a the end of the CNT was visible and is open. The position could not be used as the CNT was vibrating too much. Spots 31b, 31c, 32, 33 and 34 are imaged. Before the irradiation experiment is started, a high resolution image at 5 nm (FOV)  $2048 \times 2048$  pixels and 16  $\mu$ s is taken. Those are used for

further analysis. The irradiation is performed at 10 nm (FOV)  $1024 \times 1024$  pixels and  $16 \mu\text{s}$  dwell time. 80 frames are taken unless the CNT isn't destroyed before that. The image calibration was done in spot 32, as this shows the best resolution. The diameter and chiral angle if possible are determined. For details look sec. 3.1. A compact version of the analyzed data can be seen in Tab. 3.5. All five irradiated spots were stable for the entire 80 frames and no damage occurred.

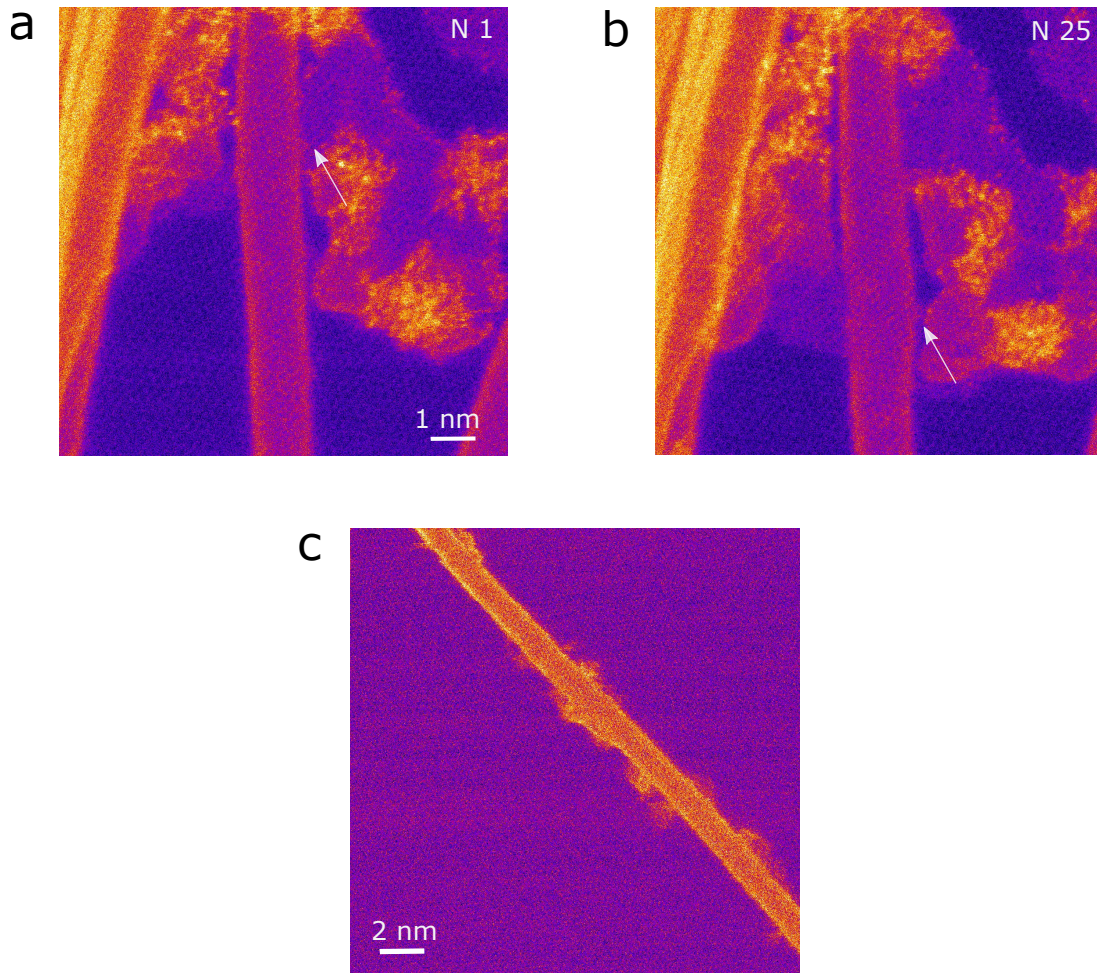


Figure 3.14: **Damaging and appearance of hydrocarbon contamination.** (a), (b) show two frames of an irradiation series of spot 37 (FOV of 10 nm,  $1024 \times 1024$  pixels and  $16 \mu\text{s}$ ) number refer to frame numbers and defects can be observed (white arrow). (c) gives an larger FOV (20 nm,  $1024 \times 1024$  pixels and  $16 \mu\text{s}$ ) of spot 34 that is contaminating and damaged under the electron beam.

**Experiment 2** This experiment is done with the same sample no.1095. The experimental approach in terms of microscope tuning and finding sample spots was the same as just described at the beginning of sec. 3.3 and the microscope was operated at 60 keV. The same hole in the carbon Quantifoil was found again in CCD-mode as in the previous experiment. The graphene layer faces the electron beam. Sample spots 35-43 are imaged. In all cases clean CNTs are found

on atomically clean graphene. An attempt was made to record one high resolution image at smaller FOV for further analysis (FOV of 5 nm,  $2048 \times 2048$  pixels and  $16 \mu\text{s}$  dwell time), like in the previous case. But both CNT in spot 35 and 36 showed clear damaging and appearance of hydrocarbon contamination already in the high resolution image. There is so much vibration in the images that they can not be used for further analysis. Several frames are recorded in both spots, but the damaging shows the same behavior as in previous cases where the damage occurs. CNT in spot 37 had definitely a defect from the CNT synthesis, as one can observe in Fig. 3.14(a). What is interesting about this spot is that although it contains a defect, the damage is not only limited to this area. It damages also several nanometers away (Fig. 3.14(b) white arrow), as there is a clear change in diameter of the CNT. The CNTs in spot 38 and 39 show damaging right from the first frame of the recorded image series (FOV of 10 nm,  $1024 \times 1024$  pixels and  $16 \mu\text{s}$  dwell time). The high resolution image for analysis was omitted in this case in order to keep track of the process. Spot 40 was stable for 2 frames and then showed the usual appearance of contamination and eventual damaging. 41 showed immediately the piling up of contamination, but only damaged after 13 frames. It is hard to tell when the actual damage starts to appear, as there is a lot of vibration in the images. 42 showed the same damaging as just described. In 43 the CNT was damaged already when setting up the scan for the irradiation series. Up to that point all imaged CNT showed piling up of mobile hydrocarbon contamination and eventual damaging. This is in complete opposition to the previous experiment with the same sample. For that reason spot 34, that was stable for 80 frames (FOV of 10 nm,  $1024 \times 1024$  pixels and  $16 \mu\text{s}$  dwell time) in the previous experiment, was imaged again. Even this CNT was contaminating immediately in various spots when imaged and it was clearly damaged, as one can observe in Fig. 3.14(c).

The diameter is analyzed as described in detail in sec. 3.1. The resolution of this experiment and the fact that CNTs damaged so fast not allowing to take an high resolution image make it impossible to measure the chiral angle in the FFT. A compact version of the data gathered in this experiment is given in Tab. 3.6. Electron dose analysis is done like described in sec. 3.2. The VOA current is reported in the metadata only for the image series. In the cases of 35, 36 and 37 the damage already occurred in the high resolution images. In these cases a quarter of the average value of the VOA current per frame from the image series is considered.

**Experiment 3** This experiment is done with the same sample no.1095. The experimental approach in terms of microscope tuning and searching for sample spots was the same as just described at the beginning of sec. 3.3 and the microscope was operated at 60 keV. The same hole in

Table 3.6: STEM data form irradiation series of sample no.1095, the diameter, the chiral angle ( $D, \alpha$ ) are given,  $No_{damage}$  and  $No_{total}$  refer to the frame numbers of the series until the first clear damage appears and the total number of frames, respectively. Further the calibrated FOV is shown. All irradiation series are taken with  $1024 \times 1024$  pixels and  $16 \mu s$  dwell time.

sample spot	$D$ [nm]	$\alpha$ [°]	$No_{damage}$	$No_{total}$	FOV [nm]
35	$0.90 \pm 0.03$	-	1	10	10.34
36	$1.65 \pm 0.03$	-	1	25	10.34
37	$1.12 \pm 0.03$	-	4	25	10.34
38	$1.15 \pm 0.03$	-	4	21	10.34
39	$0.85 \pm 0.03$	-	1	10	10.34
40	$1.28 \pm 0.03$	-	9	18	10.34
41	$1.69 \pm 0.03$	-	8	21	10.34
42	$1.00 \pm 0.03$	-	1	14	10.34
43	$1.39 \pm 0.03$	-	1	11	10.34

the carbon Quantifoil was found again in CCD-mode as in the previous experiment. There was mobile contamination piling up under the electron beam. It is growing at the boundaries of stable thick hydrocarbon contamination. One spot with an CNT was imaged (spot 46), but there was immediate appearance of mobile hydrocarbon contamination and damage, as previously observed (Fig. 3.4(a-d)). The amount of contamination and the damage of the CNT makes it impossible to measure the diameter and chiral angle. The sample is scanned at roughly  $-100\,000$  nm defocus in CCD-mode. The aim is to find monolayer graphene with CNTs on top. Another window in the gold grid is chosen that was not affected by the previous laser cleaning. Several potential positions can be found on the rest of the sample. They are too dirty and need to be cleaned by the laser. A laser-cleaning procedure is applied with the second cleaning set-up described in sec. 2.3.5. Prior to the lasering, the stage is driven to zero defocus. The laser is enabled in the menu of the microscope's software. Then the laser is pulsed at the chosen settings, this can be heard by the shutter's noise. The idea is to clean just enough to find a few clean individual CNTs on atomically clean graphene. That way large clean areas, like in the previous case, that allow surface diffusion of mobile hydrocarbon contamination are avoided. A first attempt with 25 mW for  $1500 \mu s$  was made. No visible change on the sample could be observed. The laser power was increased to 30 mW and then to 40 mW, but still no cleaning effect of any kind could be seen. The pulse time is the same, if not stated otherwise. As in the previous cases the sample was significantly cleaner

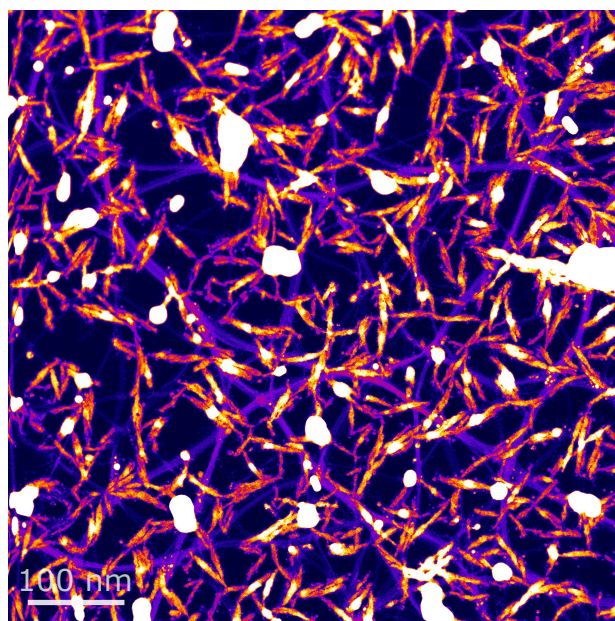


Figure 3.15: **Overview after laser cleaning.** a large overview (FOV of 640 nm, 2048×2048 pixels and 16  $\mu$ s dwell time) of sample no.1095 after the laser cleaning procedure.

at similar settings, this suggested that the alignment of the electron beam and the laser has been lost. For that reason another sample spot without CNT in another window was chosen. The laser is operated at 50 mW. Then the area around is scanned. On this sample the laser cleaning can be quite easily seen, as the needle-like contamination starts to form characteristic dots (Fig. 3.13). The position relative to the electron beam where the laser hits could be identified. The offset is  $x = -9 \mu\text{m}$  and  $y = -12 \mu\text{m}$ . Knowing that, one could move back to the position with CNTs, go to the relative off-set and start to clean the sample spot. With 25 mW and 30 mW no visible cleaning could be observed. That is surprising, as in the previous case similar settings led to significant effects. Instead with 50 mW there is difference in the image and a cleaning effect can be observed. Fig. 3.15 shows the sample spot after the laser cleaning. The sample is less clean than previously (Fig. 3.13(b)) and clean CNTs on atomically clean graphene can be found. The laser cleaning effect was quantified as previously by measuring the atomically clean area of 10 random positions in a 640 nm FOV overview. The measuring procedure for one area can be seen in (\*) of Fig. 3.13(b). The mean value and standard deviation are found to be  $(360 \pm 190) \text{ nm}^2$ . Spots 47-54 were imaged in this position. It is worth noting that unlike the previous position, in the present case the graphene was there during the CNT deposition and therefore the CNTs face the electron beam again. The CNT diameter and the chiral angle are measured. The image calibration is done in spot 47. For details look sec. 3.1. Spot 47 showed damage right on the first frame and there is a defective nanotube structure inside the CNT, similar to what was observed

Table 3.7: STEM data form irradiation series of sample no.1095, the diameter, the chiral angle ( $D, \alpha$ ) are given,  $No_{damage}$  and  $No_{total}$  refer to the frame numbers of the series until the first clear damage appears and the total number of frames, respectively. Further the calibrated FOV is shown. All irradiation series are taken with  $1024 \times 1024$  pixels and  $16 \mu s$  dwell time.

sample spot	$D$ [nm]	$\alpha$ [°]	$No_{damage}$	$No_{total}$	FOV [nm]
47	$1.29 \pm 0.03$	-	1	11	10.65
48	$1.11 \pm 0.03$	$10.1 \pm 0.6$	-	80	10.65
49	$1.35 \pm 0.03$	$27.1 \pm 0.6$	-	80	10.65
50	$1.64 \pm 0.03$	$32.2 \pm 0.6$	-	80	10.65
51	$1.20 \pm 0.03$	$20.9 \pm 0.6$	-	80	10.65
52	$1.21 \pm 0.03$	$15.5 \pm 0.6$	13	21	10.65
53	$2.00 \pm 0.03$	$29.4 \pm 0.6$	2	13	10.65
54	$1.23 \pm 0.03$	$16.6 \pm 0.6$	-	80	10.65

in Fig. 3.5(c). Spots 48 to 51 were stable for the entire 80 frames. 49 has a defect in the CNT presumably from the synthesis, but also the defect was untouched by mobile hydrocarbon contamination. 52 showed appearance of hydrocarbon contamination and damage. In 53 the usual contamination appeared, the CNT wall broke and then starting from that defective site a carbon nanobud was grown inside the CNT. Such a growth has already been observed in Fig. 3.5(a-c). The diameter, the chiral angle, the frame number where the first apparent damage appears, the total frame number of images and the calibrated FOV can be taken from Tab. 3.7. This is the last experiment leading to this thesis. The lack of controlling the mobile contamination issue made it impossible to gather further irradiation data under controlled water atmospheres.

The first two experiments with sample no.1095 were done in upside down configuration, i.e. the graphene layer faced the electron beam. In experiment 1 all CNT in 5 sample spots were beam stable, whereas in the next experiment 2 all CNTs, 9 cases, damaged with same process that has been observed previously. Therefore, one can conclude that the sample orientation has no influence on the studied damage mechanism. Spot 37 (Fig. 3.14(a)(b)) showed that the damage is not limited to positions of the CNT where a clear defect from the synthesis is visible. This supports the hypothesis that defects are not necessary for the process to happen. After the defect formation in the CNT of spot 53, a nanobud was formed inside. Carbon atoms that are trapped inside the CNT diffuse and stick to reactive site such as defects. As the end of the CNT in spot 31a was open, it is possible that molecules enter the end and start to diffuse. Much more laser power

was needed for the laser cleaning in experiment 3 with respect to experiment 1, 50 mW compared to 30 mW in order to get visible cleaning effects. In the third experiment the average clean areas after the cleaning were reduced from  $(2500 \pm 1300) \text{ nm}^2$  to  $(360 \pm 190) \text{ nm}^2$ . This indicates that size has an influence on the probability that damage and piling up on mobile contamination happens at UHV. In experiment 2 the same hole that was laser cleaned in experiment 1 was imaged again and all CNT found in the microscopy session showed immediate damage. Whereas, with less cleaning in experiment 3 only 3 out of 8 CNTs damaged. However, the size of clean area available for diffusion is not the only factor. The fact that the same CNT in spot 34 did not damage in experiment 1, but did in experiment 2 implies that it must depend on the local atmosphere of the microscope that is not constant over time. It is conceivable that the sample contaminates slightly over time and the local atmosphere in the STEM is influenced by that.

### 3.5 UHV damage, dependencies and general observations

A total of 39 independent cases where CNTs can be found on top of graphene in a 1D-2D carbon heterostructure were analyzed. In 21 cases there was damage to the CNT and apart from one case (sample spot 13) mobile hydrocarbon contamination was piled up. Looking to the damage process as a whole there are two types of cases. Cases where clear damage happens and in the other cases the CNTs are stable. The time until the first apparent defect happens is plotted as a function of the CNT diameter and chiral angle in Fig. 3.16(b)(c), respectively. There is no systematic dependence on the diameter and the chiral angle. The mean diameter of all found cases is found to be  $(1.3 \pm 0.4) \text{ nm}$ . Further, a histogram of cases with and without damage as a function of diameter was done (Fig. 3.16(d)) and the mean diameters were calculated. They are found to be with damage  $(1.3 \pm 0.5) \text{ nm}$  and without damage  $(1.35 \pm 0.26) \text{ nm}$ . Therefore there is no significant difference in diameter dependence.

Focusing on the statistical analysis of the cases with damage (Fig. 3.16(a)), the distribution as a function of electron dose until the first visible damage shows a Poisson-like behavior. The expectation value from the fit shown in Fig. 3.16(a) gives

$$\mu_{e^- \text{ dose}} = (1.29 \pm 0.4) \times 10^9. \quad (3.2)$$

Knock-on events by elastic scattering could explain the systematic dependence. One can calculate the displacement cross section for the process by eq. (2.19). The sheet density  $\rho$  is higher by a factor of  $\pi$  with respect to flat graphene, as a CNT is a rolled up graphene sheet. The value is of

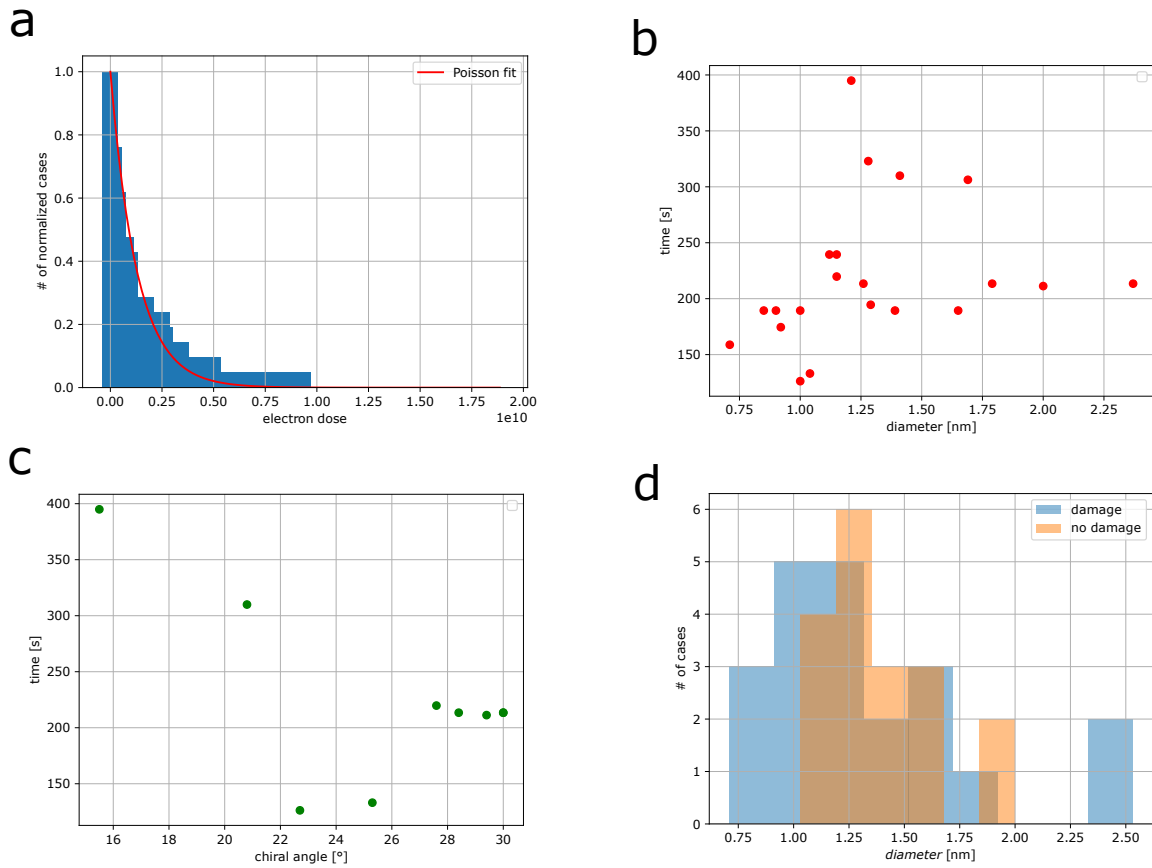


Figure 3.16: **Final analysis of damaging mechanism.** (a) the statistic analysis of the electron dose until defect formation of all observed cases with damage. (b), (c) give the dependence of the time until the first apparent defect on the diameter and chiral angle, respectively. (d) histogram of the diameters of cases with (blue) and without damage (orange).

about  $\rho = 12 \times 10^{19} \text{ m}^{-2}$ . This gives

$$\sigma = 0.065 \text{ b.} \quad (3.3)$$

This value can be compared to the elastic cross section model taking care of atomic vibrations [58]. In order to get a similar cross section at the applied 60 keV the displacement threshold energy must be in range of 13-14 eV, with a strong energy dependence.

The question remains what could lower the threshold energy enough to allow this kind of damage. Defects could play a role. There are two aspects that need to be taken into account. Firstly, it has to be checked if defects can lower the displacement threshold sufficiently. Secondly, it has to be seen if the number of occurring events can be plausibly explained in terms of defect density in the used CNTs.

The displacement threshold energies in graphene were analyzed by [70]. The minimum value was calculating for a single vacancy with a dangling bond and is of 14.7 eV. This is roughly one

1 eV too high.

The experiment were done at roughly 10 nm FOV. The mean diameter  $d$  of the CNTs was found to be about 1.3 nm. In about 20 out of 40 CNTs there needs to be at least one defect. This gives a defect density of about

$$p_{\text{defect}} = \frac{20}{40\pi \cdot 1.3 \text{ nm} \cdot 10 \text{ nm}} = 0.01 \text{ nm}^{-2}. \quad (3.4)$$

The mean distance  $L_p$  between defects is related to the intensity ratio of the Raman  $G$ -peak and the disorder  $D$ -peak the following way [71]

$$\frac{I(D)}{I(G)} = \frac{C(\lambda)}{L_p}, \quad (3.5)$$

where  $C(\lambda)$  is a wavelength-dependent constant and has a value of 4.4 nm for a wavelength of 488 nm. The CNTs synthesised by FC-CVD used in this study have a  $I(D)/I(G)$  of approximately 1/50. This gives a mean length between defect by eq. (3.5) of about 220 nm. In the easiest model this gives one defect in a cylinder segment of the mean diameter of the CNTs (1.3 nm) and length  $L_p = 220$  nm. This yields a defect density

$$p_{\text{defect}} = \frac{1}{\pi \cdot 1.3 \text{ nm} \cdot 220 \text{ nm}} = 0.001 \text{ nm}^{-2}. \quad (3.6)$$

As observed from eq. (3.4) and eq. (3.6) the two defect densities differ by on order of magnitude. In conclusion it can be stated that if the defect hypothesis was true this would lead to defect density that is significantly higher than the one based on the available Raman data.

In all experiments atomic resolution could be reached. However, not in all STEM images the resolution was high enough to reliably measure the chiral angle in the FFT. The main factors limiting the achieved resolution comprise, firstly any kind of vibrations yielding from outside, for instance if somebody is drilling in the building. In some cases the CNT shows beam-induced vibrations when imaged. A slight temperature drift between the point of the measurement of the higher order aberrations and the actual imaging in scan-mode. Coma in the probe is the most prevalent one. The sample can drift inside the puck. Moving onto different positions on the sample can have a slight impact on the tuning. Finally, also the signal to noise ratio can play a role.

# Chapter 4

## Conclusion and Outlook

In this chapter final conclusions about the outcome of the experiments will be drawn. If you are interested in the detailed discussion of individual experiments please consult the experimental chapter (ch. 3). An outlook about further potential studies based on this thesis will be given.

The research question at the basis of this thesis addresses the role and composition of the local atmosphere in the damaging of CNTs in 1D-2D VdWHs at UHV and the effect of chemical etching under controlled  $H_2$ ,  $O_2$  and  $H_2O$  atmospheres of this structure. For what concerns the experiment with controlled atmospheres it is shown that the driving force of the process is water, as  $H_2$  and  $O_2$  could be ruled out. The etching process does not rely on pre-existing defects and defects can be formed in the pristine graphitic network of the CNT. No damage of this kind has been observed to pristine graphene. The outcome of the experiments confirm the main hypothesis regarding damage under controlled water atmospheres. For the damage at UHV it can not be stated conclusively, if the damage is caused by the same mechanism as proposed for the damage observed at low-pressure water atmosphere. Instead, the Poisson-like distribution of the electron dose suggests that it could be knock-on damage caused by elastic scattering.

The main steps in the damaging mechanism are discussed.

As also freely suspended CNTs show chemical etching. It is not likely that the surface diffusion on graphene plays a predominant role in the process. This experimental outcome leads to the conclusion that molecules that cause the damage are found inside the CNTs. If one thinks about the electrons experiencing scattering by the positively charged nucleus, electrons with bigger impact parameters have a much higher cross section than smaller ones. High impact parameters cause the atoms to move perpendicular to the incident beam, whereas small ones lead to deviation

parallel to the incident beam. Thinking about flat graphene, this implies that adatoms are not stable and the same argument applies to the outside of the CNTs. It is hence most likely to have molecules bond inside the CNT.

In order to allow in-tube diffusion the molecules must enter at the ends of the CNT. It is not trivial that the CNTs are open at their ends. In at least one case the end of a CNT was imaged that was open. This makes the concept plausible. It is also conceivable that the damage process depends on the nature of the ends. This couldn't be checked experimentally, as the indication arose only after the end of the experiments and further the ends are not always observable in the microscope.

The water molecules are split into hydrogen and OH-molecules by exciting the electrons to a non-bonding orbital. This is easily fulfilled by the energy of the incident electrons.

The point defect formation by OH-group assistance under electron irradiation, as discussed by [12], could apply to the carbon atoms of CNTs. The energy barriers are too high to overcome thermally at room temperature, the energy must hence be supplied by the incoming electron beam. The outcome of the experiments leading to this thesis can not in detail answer how this works. However, it is shown that pristine CNTs experience damage under water leakage.

There are no cases where the damage does not happen under water leakage. It can not be answered conclusively how the damage depends on the pressure of the leaked water vapor. The time until the defect is expected to be dependent on the number of water molecules available and a stochastic process involving the bonding to carbon atoms.

Once a defect is formed, this acts as nucleation center for the whole process. This is supported by the fact that no CNT in the entire experiments recovered once the process has started. Defective CNTs show the same chemical etching behavior as defective graphene. It has been shown by the experiments that this process, when a defect is already present, can in principle be both water and oxygen driven.

The statistic analysis of the electron dose for the damage at UHV revealed a Poisson-like behavior. This suggests that the damaging mechanism can be a knock-on process by elastic scattering. It remains an open question what could lower the displacement threshold energy sufficiently. Defects alone can not explain the observed mechanism, as the expected defect density is about one order of magnitude too low and the threshold energy is not exceeded at 60 keV. What could play role is that the bonding of an OH-molecule to the sidewall inside a CNT would lower the

displacement threshold energy of the carbon atom sufficiently giving rise to a chemically assisted knock-on damage.

It can not be stated by the outcome of the experiment what the exact role of the mobile hydrocarbon contamination is in the damaging under UHV. By simply observing the STEM images, one tends to give a causal role to the mobile contamination, but there was one case where damage happened without building up of mobile contamination. So the most plausible picture is that contamination diffuses on the graphene surface, once a defect is formed it sticks to this reactive site and becomes visible in the STEM image. But what can be stated is that the process with pilling up of contamination is not reversible, as there is no cases where the CNT recovers after the appearance of mobile contamination. It can not be conclusively stated that the probability of damage depends on the size of atomically clean area of graphene around the sample spot.

The mobile contamination in the FOV is radicalized by the electron beam as light hydrogen atoms are scattered away. That way the chemical reactivity is enhanced and further contamination is build up.

To get a conclusive guess that the damage only depends on the local atmosphere, experiments at ideally three different pressure ranges are necessary. To rule out damage at UHV and defects playing a role, the experiment must be designed the following way. A UHV control series must be done, then oxygen is leaked and another irradiation experiment is performed, after that if the CNT is stable the oxygen is pumped out again and then the actual water leakage experiment can be done. The time until the first damage must depend on the pressure of the water leakage.

In terms of future computational work, it would be very interesting to study the impact of the OH-molecules bonding on the displacement threshold energy of the carbon atom.

As water experiments lead to damage one could think of taking advantage of that in terms of defect engineering. The big advantage of this method is that looking to the energetics involved in the process the damage is expected to be highly localized under the electron beam, as energy must be supplied by the electrons. One application might be that CNT are cut under controlled water atmospheres midst a small area scan without touching the pristine graphene below. A partial N<sub>2</sub> atmosphere could be split up under the electron beam and lead to N dopants in the CNT lattice. When partially leaking a carbon source such as CO, it is split under the electron beam and carbon atoms become available. These could be integrated into the CNT structure at the defective site leading to change in diameter and chirality locally and hence in the electronic

properties, as it was observed in several experiments.

# Bibliography

- [1] G. T. Leuthner, C. Mangler, J. C. Meyer, T. Susi, J. Kotakoski, Atomic-scale Chemical Manipulation of Materials in the Scanning Transmission Electron Microscope under Controlled Atmospheres, *Microscopy and Microanalysis* 25 (S2) (2019) 1398–1399. doi:10.1017/s1431927619007724.
- [2] G. T. Leuthner, T. Susi, C. Mangler, J. C. Meyer, J. Kotakoski, Chemistry at graphene edges in the electron microscope, *2D Materials* 8 (3) (2021) 035023. doi:10.1088/2053-1583/abf624.
- [3] T. Odom, J.-L. Huang, P. Kim, C. Lieber, Structure and Electronic Properties of Carbon Nanotubes, *Journal of Physical Chemistry B* 104 (13) (2000) 2794–2809. doi:10.1021/jp993592k.
- [4] A. Chodos, Discovery of Graphene, <https://www.aps.org/publications/apsnews/200910/physicshistory.cfm>, last date accessed: 2022-07-03.
- [5] F. Banhart, J. Kotakoski, A. V. Krasheninnikov, Structural Defects in Graphene, *ACS Nano* 5 (1) (2011) 26–41. doi:10.1021/nn102598m.
- [6] Y. V. Skrypnik, V. M. Loktev, Electronic properties of graphene with point defects (Review Article), *Low Temperature Physics* 45 (12) (2019) 1310–1342. doi:10.1063/1.0000565.
- [7] M. Tripathi, A. Mittelberger, K. Mustonen, C. Mangler, J. Kotakoski, J. C. Meyer, T. Susi, Cleaning graphene: Comparing heat treatments in air and in vacuum, *Physica Status Solidi - Rapid Research Letters* 11 (8) (2017) 1700124. doi:10.1002/pssr.201700124.
- [8] K. A. Mustonen, A. Hussain, C. Hofer, M. Reza, A. Monazam, R. Mirzayev, K. Elibol, P. Laiho, C. Mangler, H. Jiang, T. Susi, E. I. Kauppinen, J. Kotakoski, J. C. Meyer, Atomic-Scale Defor-

mations at the Interface of a Mixed-Dimensional van der Waals Heterostructure, *ACS Nano* 12 (8) (2018) 8512–8519. doi:10.1021/acsnano.8b04050.

- [9] D. Jariwala, T. J. Marks, M. C. Hersam, Mixed-dimensional van der Waals heterostructures, *Nature Materials* 16 (2) (2016) 170–181. doi:10.1038/nmat4703.
- [10] L. Britnell, R. V. Gorbachev, R. Jalil, B. D. Belle, F. Schedin, A. Mishchenko, T. Georgiou, M. I. Katsnelson, L. Eaves, S. V. Morozov, N. M. Peres, J. Leist, A. K. Geim, K. S. Novoselov, L. A. Ponomarenko, Field-effect tunneling transistor based on vertical graphene heterostructures, *Science* 335 (6071) (2012) 947–950. doi:10.1126/science.1218461.
- [11] J. C. Meyer, F. Eder, S. Kurasch, V. Skakalova, J. Kotakoski, H. J. Park, S. Roth, G. Benner, A. V. Krasheninnikov, U. Kaiser, A. Chuvilin, Accurate Measurement of Electron Beam Induced Displacement Cross Sections for Single-Layer Graphene, *Physical Review B* 108 (2012) 196102. doi:10.1103/PhysRevLett.108.196102.
- [12] G. H. Ryu, S. Lee, J. H. Kim, G. D. Lee, Z. Lee, OH molecule-involved formation of point defects in monolayer graphene, *Nanotechnology* 32 (2) (2020) 025704. doi:10.1088/1361-6528/abb9d7.
- [13] A. H. Castro Neto, F. Guinea, N. M. R. Peres, K. S. Novoselov, A. K. Geim, The electronic properties of graphene, *Reviews of Modern Physics* 81 (1) (2009) 109–162. doi:10.1103/RevModPhys.81.109.
- [14] R. Saito, M. Hofmann, G. Dresselhaus, A. Jorio, M. S. Dresselhaus, *Advances in Physics*, *Advances in Physics* 60 (3) (2011) 413–550. doi:10.1080/00018732.2011.582251.
- [15] L. E. F. Foa Torres, S. Roche, J.-C. Charlier, *Introduction to Graphene-Based Nanomaterials. From Electronic Structure to Quantum Transport*, Cambridge University Press, New York, 2014.
- [16] M. Dresselhaus, G. Dresselhaus, R. Saito, A. Jorio, Raman spectroscopy of carbon nanotubes, *Physics Reports* 409 (2) (2005) 47–99. doi:10.1016/j.physrep.2004.10.006.
- [17] M. S. Dresselhaus, P. C. Eklund, Phonons in carbon nanotubes, *Advances in Physics* 49 (6) (2000) 705–814. doi:10.1080/000187300413184.
- [18] J. Maultzsch, S. Reich, C. Thomsen, E. Dobardžić, I. Milošević, M. Damnjanović, Phonon dispersion of carbon nanotubes, *Solid State Communications* 121 (2002) 471–474. doi:10.1016/S0038-1098(02)00025-X.

- [19] R. Muñoz, C. Gómez-Aleixandre, Review of CVD Synthesis of Graphene, *Chemical Vapor Deposition* 19 (2013) 297–322. doi:10.1002/cvde.201300051.
- [20] Graphenea, "Easy Transfer" Graphene, <https://www.graphenea.com/products/easy-transfer-monolayer-graphene-on-polymer-film>, last date accessed: 2022-06-30.
- [21] Tedpella, Silicon Nitride holey TEM films, <https://www.tedpella.com/grids/html/silicon-nitride-holely.htm>, last date accessed: 2022-06-30.
- [22] A. Moisala, A. G. Nasibulin, D. P. Brown, H. Jiang, L. Khriachtchev, E. I. Kauppinen, Single-walled carbon nanotube synthesis using ferrocene and iron pentacarbonyl in a laminar flow reactor, *Chemical Engineering Science* 61 (13) (2006) 4393–4402. doi:10.1016/j.ces.2006.02.020.
- [23] Y. Liao, Carbon dioxide-assisted synthesis of single-walled carbon nanotubes and their thin film properties, Ph.D. thesis, Aalto University (2019).
- [24] P. Laiho, K. Mustonen, Y. Ohno, S. Maruyama, E. I. Kauppinen, Dry and Direct Deposition of Aerosol-Synthesized Single-Walled Carbon Nanotubes by Thermophoresis, *ACS Applied Materials and Interfaces* 9 (24) (2017) 20738–20747. doi:10.1021/acsami.7b03151.
- [25] C. Hinds, Williams, *Aerosol Technology: Properties, Behavior and Measurement of airborne Particles*, John Wiley and Sons, Boston, 1982.
- [26] A. Moisala, A. G. Nasibulin, S. D. Shandakov, H. Jiang, E. I. Kauppinen, On-line detection of single-walled carbon nanotube formation during aerosol synthesis methods, *Carbon* 43 (10) (2005) 2066–2074. doi:10.1016/j.carbon.2005.03.012.
- [27] P. Intra, N. Tippayawong, An overview of differential mobility analyzers for size classification of nanometer-sized aerosol particles, *Songklanakarin Journal of Science and Technology* 30 (2) (2008) 243–256.
- [28] Mariam, M. Joshi, P. Khandare, A. Koli, A. Khan, B. K. Sapra, Influence of sheath air humidity on measurement of particle size distribution by scanning mobility particle sizer, *Journal of Aerosol Science* 111 (2017) 18–25. doi:10.1016/j.jaerosci.2017.05.005.

- [29] A. Kaskela, P. Laiho, N. Fukaya, K. Mustonen, T. Susi, H. Jiang, N. Houbenov, Y. Ohno, E. I. Kauppinen, Highly individual SWCNTs for high performance thin film electronics, *Carbon* 103 (2016) 228–234. doi:10.1016/j.carbon.2016.02.099.
- [30] Y. Tian, H. Jiang, J. V. Pfaler, Z. Zhu, A. G. Nasibulin, T. Nikitin, B. Aitchison, L. Khriachtchev, D. P. Brown, E. I. Kauppinen, Analysis of the size distribution of single-walled carbon nanotubes using optical absorption spectroscopy, *Journal of Physical Chemistry Letters* 1 (7) (2010) 1143–1148. doi:10.1021/jz100161p.
- [31] K. Mustonen, P. Laiho, A. Kaskela, Z. Zhu, O. Reynaud, N. Houbenov, Y. Tian, T. Susi, H. Jiang, A. G. Nasibulin, E. I. Kauppinen, Gas phase synthesis of non-bundled, small diameter single-walled carbon nanotubes with near-armchair chiralities, *Applied Physics Letters* 107 (1) (2015) 013106. doi:10.1063/1.4926415.
- [32] A. Hussain, Y. Liao, Q. Zhang, E. X. Ding, P. Laiho, S. Ahmad, N. Wei, Y. Tian, H. Jiang, E. I. Kauppinen, Floating catalyst CVD synthesis of single walled carbon nanotubes from ethylene for high performance transparent electrodes, *Nanoscale* 10 (20) (2018) 9752–9759. doi:10.1039/c8nr00716k.
- [33] I. Heena, Atomic scale dynamics and modifications of stacked heteronanostructures under extreme conditions, Ph.D. thesis, University of Vienna (2021).
- [34] R. Bridson (Ed.), *Aberration-corrected analytical transmission electron microscopy*, RMS-Wiley, Chichester, West Sussex, 2011.
- [35] G. T. Leuthner, Electron irradiation effects in two-dimensional materials, Ph.D. thesis, University of Vienna (2021).
- [36] O. L. Krivanek, M. F. Chisholm, V. Nicolosi, T. J. Pennycook, G. J. Corbin, N. Dellby, M. F. Murfitt, C. S. Own, Z. S. Szilagyi, M. P. Oxley, S. T. Pantelides, S. J. Pennycook, Atom-by-atom structural and chemical analysis by annular dark-field electron microscopy, *Nature* 464 (7288) (2010) 571–574. doi:10.1038/nature08879.
- [37] M. De Graef, *Introduction to conventional transmission electron microscopy*, Cambridge University Press, Cambridge, U.K. ; New York, N.Y., 2003.
- [38] I. Alex, Sources of electrons, <https://www.thermofisher.com/blog/microscopy/electron-source-fundamentals/>, last date accessed: 2022-06-28.

- [39] L. Yougui, Practical Electron Microscopy and Database. Isoplanatic Approximation, <https://www.globalsino.com/EM/page3701.html>, last date accessed: 2022-06-30.
- [40] A. R. Krivanek, O. L., Dellby, N., Lupini, Towards sub-Angström electron beams, *Ultramicroscopy* 78 (1999) 1–11. doi:10.1016/S0304-3991(99)00013-3.
- [41] L. Yougui, Practical Electron Microscopy and Database. Axial Coma Aberration in EMs, <https://www.globalsino.com/EM/page3666.html>, last date accessed: 2022-06-27.
- [42] O. L. Krivanek, G. J. Corbin, N. Dellby, B. F. Elston, R. J. Keyse, M. F. Murfitt, C. S. Own, Z. S. Szilagy, J. W. Woodruff, An electron microscope for the aberration-corrected era, *Ultramicroscopy* 108 (2008) 179–195. doi:10.1016/j.ultramic.2007.07.010.
- [43] H. Jiang, A. G. Nasibulin, D. P. Brown, E. I. Kauppinen, Unambiguous atomic structural determination of single-walled carbon nanotubes by electron diffraction, *Carbon* 45 (2006) 662–667. doi:10.1016/j.carbon.2006.07.025.
- [44] O. Dyck, S. Kim, S. V. Kalinin, S. Jesse, Mitigating e-beam-induced hydrocarbon deposition on graphene for atomic-scale scanning transmission electron microscopy studies, *Journal of Vacuum Science and Technology B, Nanotechnology and Microelectronics: Materials, Processing, Measurement, and Phenomena* 36 (1) (2018) 011801. doi:10.1116/1.5003034.
- [45] T. C. Isabell, P. E. Fischione, C. O’Keefe, M. U. Guruz, V. P. Dravid, Plasma cleaning and its applications for electron microscopy, *Microscopy and Microanalysis* 5 (2) (1999) 126–135. doi:10.1017/S1431927699000094.
- [46] G. Algara-Siller, O. Lehtinen, A. Turchanin, U. Kaiser, Dry-cleaning of graphene, *Applied Physics Letters* 104 (15) (2014) 153115. doi:10.1063/1.4871997.
- [47] V. Atanasov, A. Saxena, Tuning the electronic properties of corrugated graphene: Confinement, curvature, and band-gap opening, *Physical Review B - Condensed Matter and Materials Physics* 81 (20) (2010) 205409. doi:10.1103/PhysRevB.81.205409.
- [48] Y. V. Shtogun, L. M. Woods, Electronic and magnetic properties of deformed and defective single wall carbon nanotubes, *Carbon* 47 (14) (2009) 3252–3262. doi:10.1016/j.carbon.2009.07.042.

- [49] T. M. G. Mohiuddin, A. Lombardo, R. R. Nair, A. Bonetti, G. Savini, R. Jalil, N. Bonini, D. M. Basko, C. Galiotis, N. Marzari, K. S. Novoselov, A. K. Geim, A. C. Ferrari, Uniaxial strain in graphene by Raman spectroscopy: G peak splitting, Grüneisen parameters, and sample orientation, *Physical Review B* 79 (20) (2009) 205433. [doi:10.1103/PhysRevB.79.205433](https://doi.org/10.1103/PhysRevB.79.205433).
- [50] J.-K. Lee, K. P. S. S. Hembam, Y. Park, S.-G. Lee, J.-G. Kim, W. Lee, D. J. Moon, Raman Radial Mode Revealed from Curved Graphene, *Physical Chemistry Letters* (8) (2017) 2597–2601. [doi:10.1021/acs.jpcclett.7b01220](https://doi.org/10.1021/acs.jpcclett.7b01220).
- [51] F. Rana, Electron-Hole Generation and Recombination Rates for Coulomb Scattering in Graphene, *Physical Review B* 76 (2007) 155431. [doi:10.1103/PhysRevB.76.155431](https://doi.org/10.1103/PhysRevB.76.155431).
- [52] T. Susi, C. Hofer, G. Argentero, G. T. Leuthner, T. J. Pennycook, C. Mangler, J. C. Meyer, J. Kotakoski, Isotope analysis in the transmission electron microscope, *Nature Communications* 7 (1) (2016) 13040. [doi:10.1038/ncomms13040](https://doi.org/10.1038/ncomms13040).
- [53] A. Zobelli, A. Gloter, C. P. Ewels, G. Seifert, C. Colliex, Electron knock-on cross section of carbon and boron nitride nanotubes, *Phys. Rev. B* 75 (24) (2007) 245402. [doi:10.1103/PhysRevB.75.245402](https://doi.org/10.1103/PhysRevB.75.245402).
- [54] A. Zobelli, A. Gloter, C. P. Ewels, C. Colliex, Shaping single walled nanotubes with an electron beam, *Phys. Rev. B* 77 (4) (2008) 045410. [doi:10.1103/PhysRevB.77.045410](https://doi.org/10.1103/PhysRevB.77.045410).
- [55] A. V. Krasheninnikov, F. Banhart, J. X. Li, A. S. Foster, R. M. Nieminen, Stability of carbon nanotubes under electron irradiation: Role of tube diameter and chirality, *Physical Review B - Condensed Matter and Materials Physics* 72 (12) (2005) 125428. [doi:10.1103/PhysRevB.72.125428](https://doi.org/10.1103/PhysRevB.72.125428).
- [56] J. H. Warner, F. Scha, G. Zhong, M. H. Ru, B. Bu, J. Robertson, G. A. D. Briggs, Investigating the Diameter-Dependent Stability of Single-Walled Carbon Nanotubes, *ACS Nano* 3 (6) (2009) 1557–1563. [doi:10.1021/nn900362a](https://doi.org/10.1021/nn900362a).
- [57] T. Susi, J. Kotakoski, R. Arenal, S. Kurasch, H. Jiang, V. Skakalova, O. Stephan, A. V. Krasheninnikov, E. I. Kauppinen, U. Kaiser, J. C. Meyer, Atomistic Description of Electron Beam Damage in Nitrogen-Doped Graphene and Single-Walled Carbon Nanotubes, *ACS Nano* 6 (10) (2012) 8837–8846. [doi:10.1021/nn303944f](https://doi.org/10.1021/nn303944f).

- [58] A. I. Chirita Mihaila, T. Susi, J. Kotakoski, Influence of temperature on the displacement threshold energy in graphene, *Scientific Reports* 9 (1) (2019) 12981. doi:10.1038/s41598-019-49565-4.
- [59] N. Al-Aqtash, I. Vasiliev, Ab initio study of carboxylated graphene, *Journal of Physical Chemistry C* 113 (30) (2009) 12970–12975. doi:10.1021/jp902280f.
- [60] N. Ghaderi, M. Peressi, First-principle study of hydroxyl functional groups on pristine, defected graphene, and graphene epoxide, *Journal of Physical Chemistry C* 114 (49) (2010) 21625–21630. doi:10.1021/jp108688m.
- [61] P. Denis, F. Iribarne, Comparative Study of Defect Reactivity in Graphene, *The Journal of Physical Chemistry C* 117 (2013) 19048–19055. doi:10.1021/jp4061945.
- [62] S. Niyogi, M. A. Hamon, H. Hu, B. Zhao, P. Bhowmik, R. Sen, M. E. Itkis, R. C. Haddon, Chemistry of Single-Walled Carbon Nanotubes, *ACC. Chem. Res.* 35 (2002) 1105–1113. doi:10.1021/ar010155r.
- [63] B. Liu, H. Jiang, A. V. Krasheninnikov, A. G. Nasibulin, W. Ren, C. Liu, E. I. Kauppinen, H. M. Cheng, Chirality-dependent reactivity of individual single-walled carbon nanotubes, *Small* 9 (8) (2013) 1379–1386. doi:10.1002/smll.201202761.
- [64] J. A. Yan, M. Y. Chou, Oxidation functional groups on graphene: Structural and electronic properties, *Physical Review B - Condensed Matter and Materials Physics* 82 (12) (2010) 125403. doi:10.1103/PhysRevB.82.125403.
- [65] T. T. Jia, B. Z. Sun, H. X. Lin, Y. Li, W. K. Chen, Bonding of hydroxyl and epoxy groups on graphene: Insights from density functional calculations, *Jiegou Huaxue* 32 (10) (2013) 1475–1484.
- [66] S. Y. Kim, J. L. Lee, K. B. Kim, Y. H. Tak, Effect of ultraviolet-ozone treatment of indium-tin-oxide on electrical properties of organic light emitting diodes, *Journal of Applied Physics* 95 (2004) 2560–2563. doi:10.1063/1.1635995.
- [67] W. Li, Y. Liang, D. Yu, L. Peng, K. P. Pernstich, T. Shen, A. R. Hight Walker, G. Cheng, C. A. Hacker, C. A. Richter, Q. Li, D. J. Gundlach, X. Liang, Ultraviolet/ozone treatment to reduce metal-graphene contact resistance, *Applied Physics Letters* 102 (2013) 183110. doi:10.1063/1.4804643.

- [68] M. F. Budyka, T. S. Zyubina, A. G. Ryabenko, S. H. Lin, A. M. Mebel, Bond lengths and diameters of armchair single wall carbon nanotubes, *Chemical Physics Letters* 407 (2005) 266–271. [doi:10.1016/j.cplett.2005.03.088](https://doi.org/10.1016/j.cplett.2005.03.088).
- [69] R. Bistritzer, A. H. Macdonald, Moiré bands in twisted double-layer graphene, *PNAS* 108 (30) (2011) 12233–12237. [doi:10.1073/pnas.1108174108](https://doi.org/10.1073/pnas.1108174108).
- [70] J. Kotakoski, D. Santos-Cottin, A. V. Krasheninnikov, Stability of graphene edges under electron beam: Equilibrium energetics versus dynamic effects, *ACS Nano* 6 (1) (2012) 671–676. [doi:10.1021/nn204148h](https://doi.org/10.1021/nn204148h).
- [71] M. M. Lucchese, F. Stavale, E. H. Ferreira, C. Vilani, M. V. Moutinho, R. B. Capaz, C. A. Achete, A. Jorio, Quantifying ion-induced defects and Raman relaxation length in graphene, *Carbon* 48 (5) (2010) 1592–1597. [doi:10.1016/j.carbon.2009.12.057](https://doi.org/10.1016/j.carbon.2009.12.057).